An Investigation into the Motility of Environmental Haloarchaeal Species

KATIE LOUISE THORNTON (M.SC., B.SC. (HONS))

Ph.D.

University of York

PHYSICS

NOVEMBER 2018

Abstract

This work uses holographic microscopy (and other optical microscopy techniques) to explore the swimming behaviours of three environmental strains of haloarchaea. Archaea extracted from two highly saline environments; The Great Salt Lake, Utah and Boulby Potash Mine, UK were sequenced to discover species identity and motility appendage structure. Optimal growth conditions were established, through the use of spectrophotometry and dark field spectroscopy. Thousands of cells were then simultaneously tracked in three-dimensions, using digital holographic microscopy (DIHM). The tracks were computationally analysed and motility features extracted. This thesis represents the first example of exploration into the three-dimensional swimming behaviours of any haloarchaeal species.

Genetic sequencing revealed samples of *Haloarcula hispanica* and *Haloferax volcanii* extracted from the Great Salt Lake and Boulby Mine respectively. Flagella genes from the samples highlighted variations in the composition of the archaellum structure of two samples of *H. hispanica* and a further variant in *Hx. volcanii*. DIHM experiments resulted in similar swimming behaviours across the three samples tested. The haloarchaeal cells swam very slowly, with average speeds of $\approx 2\,\mu$m/s. Cells typically reorientated much less frequently than bacterial counterparts ($\approx$ every 10-15 seconds on average). Furthermore, individuals displayed the previously characterised 'run-reverse' reorientation type, without the 'flick' associated with having a flagella hook. All samples were affected by high levels of Brownian rotation and an interesting, 'wobble' movement.

Overall this project aims to fully evaluate the motile behaviours of archaeal samples extracted directly from their natural habitats, in an attempt to gain further insight into microorganisms living in extreme hypersaline environments.

Contents

List of Tables

List of Figures

Acknowledgments

I would like to take this opportunity to offer thanks to the people who helped make the completion of this thesis possible. Firstly, I am especially grateful to my supervisor, Dr Laurence Wilson, for his invaluable advice, continued support and patience. Secondly, to my other TAP members; Dr Keith McKenna, Prof. Mark Leake and Dr Robert Greenall who offered guidance, useful feedback and interesting discussion.

I would like to offer further thanks to Dr Pegine Walrad, Prof. Seth Davis and Dr James Chong, who each gave up their valuable time to offer me advice and assistance in making the genetic sequencing possible. I am also grateful to Dr. Bonnie Baxter and the team at The Great Salt Lake for collecting, culturing and posting my samples. Furthermore, to all the fantastic staff at Boulby Potash Mine who invited us to the site and gave up their time to help us collect samples; your assistance and expertise made us feel incredibly welcome.

To all the kind people who offered me lab space, equipment and/or advice over the past few years. I greatly appreciate your generosity, enthusiasm and the time you managed to spare. Also, to all members of the bio-soft matter group for your interesting discussions and critical feedback.

My appreciation to Josie Burnett and Tony Barker, without team unicorn my finances would be poorer and my stories fewer.

Final thanks go to all the people who helped keep me sane. Firstly, to Nikky Farthing for sharing in all the rants, coffee and holidays, may we have many more to come. To Alex Hilley for helping me quiet my mind and focus my thoughts when I needed it most. Lastly to my family, especially my sister Sarah, for always understanding, knowing exactly what to say, and simply being there.

Author's declaration

I declare that the work in this thesis was carried out in accordance with the requirements of the University's Regulations and Code of Practice for Research Degree Programmes and that it has not been submitted for any other academic award. Except where indicated by specific reference in the text, the work is the candidate's own work. Work done in collaboration with, or with the assistance of, others, is indicated as such. Any views expressed in the thesis are those of the author.

...'Parts of the lake seen from a short distance appeared of a reddish colour, and this perhaps was owing to some infusorial animalcula...How suprising it is that any creatures should be able to exist in brine, and that they should be crawling among the crystals of sulphate of soda and lime!...Thus we have a little living world within itself, adapted to these inland lakes of brine.'

Charles Darwin - The Voyage of H.M.S Beagle

Chapter 1

Introduction

1.1 The Physics of Being Small

Life on earth spans a colossal size range of over eight orders of magnitude. The largest, a blue whale (*Balaenoptera musculus*) a staggering 30 m long, to the smallest nano bacterium currently recorded (*Nanobacterium sanguinem*), at only 200 nm in diameter [1]. With both ends of the body size spectrum inhabiting fluid environments, it is hardly surprising that the forces governing these organisms vary extensively. This thesis focuses entirely on life at the smallest end of the scale, the microscopic world.

Microorganisms are ubiquitous to every conceivable environment on earth. Yet the forces that govern the way in which they perceive the world are very different from the human experience. At small scales viscosity dominates and inertial forces are inconsequential.

This chapter introduces some of the physics governing swimming microorganisms, and details the mechanisms utilised for successful locomotion at the micro-scale.

1.1.1 Low Reynolds Number

Organisms smaller than 1 mm experience a world dominated by viscous forces, where inertial forces are negligible. The ratio of viscous to inertial forces acting on an object or organism within a liquid environment can be defined by a dimensionless scaling factor, known as the Reynolds Number [2, 3].

$$Re = \frac{F_{inertial}}{F_{viscous}} = \rho \frac{VL}{\eta} \tag{1.1}$$

whereby V is the typical flow velocity, η and ρ are the kinematic viscosity and density of the fluid, respectively and L is a characteristic length scale [3]. The characteristic length scale is somewhat subjective, but typically refers to the diameter of the object affecting the flow. For example, for a boat moving forwards through stationary water, the width of the boat would be selected, as this has a bigger impact on the surrounding fluid than its length. Other examples of characteristic lengths would be the diameter of a stationary sphere in a moving fluid, or the diameter of a pipe restricting the fluid-flow [2]. In the case of swimming microorganisms, the characteristic length L is generally the diameter of the cell body perpendicular to the direction of movement.

At low Reynolds numbers ($Re < 1$) the increased effect of viscous forces has a dampening effect on incipient eddies and irregularities in the surrounding fluid, which in inertia dominant regimes would typically lead to turbulence. In viscous environments this lack of asymmetry in the surrounding fluid leads to a reversibility of flow, making any movements time-independent. Consequently, periodic movement, such as the up and down movement of a paddle or the opening and closing of a hinged shell becomes ineffective in low Reynolds regimes producing no net movement in any direction [4]. In order to successfully progress through a viscous environment, the driving motion must be asymmetrical in some way, exploring two or more degrees of freedom.

1.1.2 Péclet Number

Another useful parameter for defining the movement of objects suspended in a fluid is the Péclet Number. The Péclet Number is a dimensionless unit for describing the transport of particles by diffusion or advection.

$$P_e \approx \frac{vL}{D} \tag{1.2}$$

Where L is the characteristic length, v is the velocity and D is the diffusion coefficient [5].

1.2 Brownian Motion

Brownian motion refers to the irregular diffusive movements of small, free particles in aqueous media. This motion arises from thermal energy, which results in random movements in any random direction (translational diffusion), and the random rotation about any axis (rotational diffusion). In 1905 Einstein showed that a particle in thermal equilibrium with a medium at temperature (T) will have kinetic energy associated with translation along any axis. This is true for particles of any size [6], freely moving, in a homogeneous solution. The magnitude of this movement in any direction can be calculated as a diffusion coefficient (D). It is convenient to separate diffusion into two aspects: translational and rotational diffusion.

1.2.1 Translational Diffusion

The diffusion coefficient D is given by Einstein's equation:

$$D = \frac{kT}{f} \tag{1.3}$$

$$k = \frac{R_g}{N_{Av}} = 1.38 \times 10^{23} m^2 kg s^{-2} K^{-1} \tag{1.4}$$

Where k is the Boltzmann constant (the ratio of the molar gas constant R_g to Avogadro's number N_{Av}), T is the absolute temperature, and f is the frictional coefficient of the particle. The frictional coefficient (f) of an object can be calculated as the force (F) divided by its velocity (v). In low Reynold's regimes inertia is negligible therefore the controlling force is the viscous drag (F_D) acting upon the object.

Stokes' law for the drag of a sphere is defined as:

$$F_D = 6\pi\eta\alpha v \tag{1.5}$$

When considering a spherical particle with radius α, in a Newtonian liquid with viscosity η the frictional coefficient becomes:

$$f = \frac{F}{v} = 6\pi\eta\alpha \tag{1.6}$$

The combined result:

$$D = \frac{kT}{6\pi\eta\alpha} \tag{1.7}$$

This is often referred to as Stokes-Einstein SE diffusion coefficient for transnational diffusion within a sphere.

1.2.2 Rotational Diffusion

The rotational diffusion coefficient D_r has a similar form as the transnational equation, but with a different frictional coefficient.

$$D_r = \frac{kT}{f_r} = \frac{kT}{8\pi\eta\alpha^3} \tag{1.8}$$

1.2.3 The Random Walk Model

A random walk is typically described as a stochastic process that has an equal probability of either +/- 1 in either direction. Brownian motion is often described as a random walk, as a diffusing particle has an equal probability of moving in any particular direction [6]. For a particle undergoing the random movements of Brownian motion, the distance travelled does not scale linearly with time and paths frequently revisit already explored areas (figure 1.1). Consequently, the root mean square of the displacement can be used to calculate the diffusivity of an organism or particle [5].

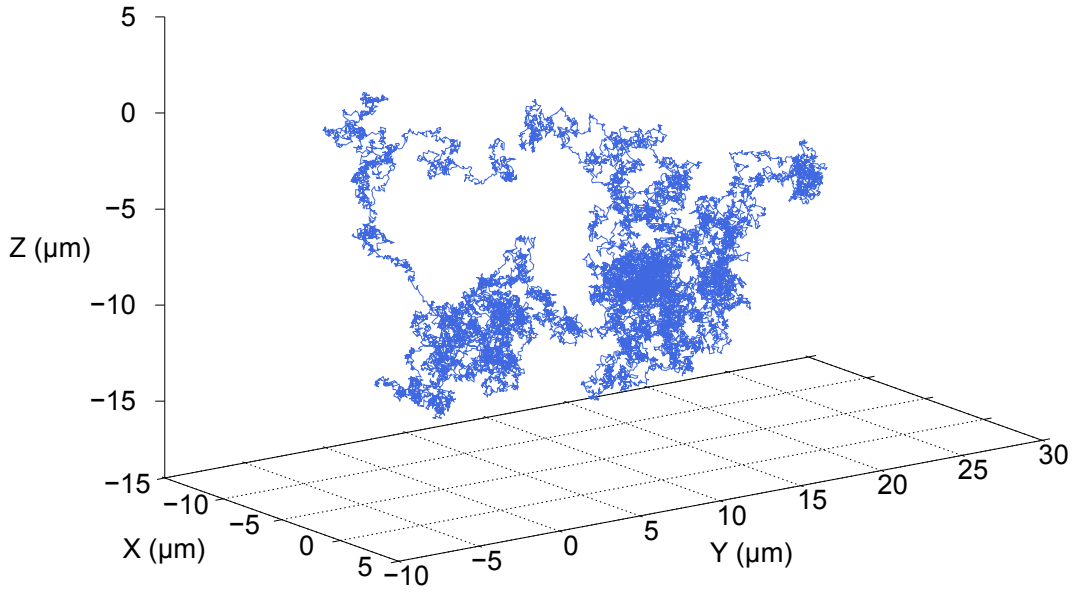

FIGURE 1.1. Example simulated diffusion trajectory. Trajectory parameters are: 10 minutes at 50 samples per second, starting at position 0, 0, 0. Particle is defined as spherical, 1 μm in diameter, in pure water and at room temperature (22°C).

If a particle is moving in just one dimension;

$$x_{rms} = < x^2 >^{1/2} = \sqrt{2\frac{R_g T}{N_{Av}}\frac{t}{f}} = \sqrt{2Dt} \tag{1.9}$$

Whereby, R_g is the molar gas constant, N_{Av} is Avogadro's number, T is the absolute temperature, and f is the frictional coefficient of the particle. As in equation 1.3, these can be simplified to create the diffusion coefficient D. t denotes time.

Therefore;

$$< x^2 >= 2Dt \tag{1.10}$$

Consequently, the distance displaced increases with the square root of time. This can be scaled to three dimensions where;

$$< r^2 >= 6Dt \tag{1.11}$$

[5, 6]

1.3 Micro-swimming

Many microorganisms have developed the ability to move in an attempt to improve their immediate surroundings. The reasons for locomotion are very diverse including, but not limited to; locating food, avoiding detrimental environmental conditions, finding a mate or host, and evading predators. Whilst synthesizing motility apparatus can be energetically expensive, the benefits gained through exploitation of nutrient patches (for example), can often far outweigh the cost [7] (figure 1.2).

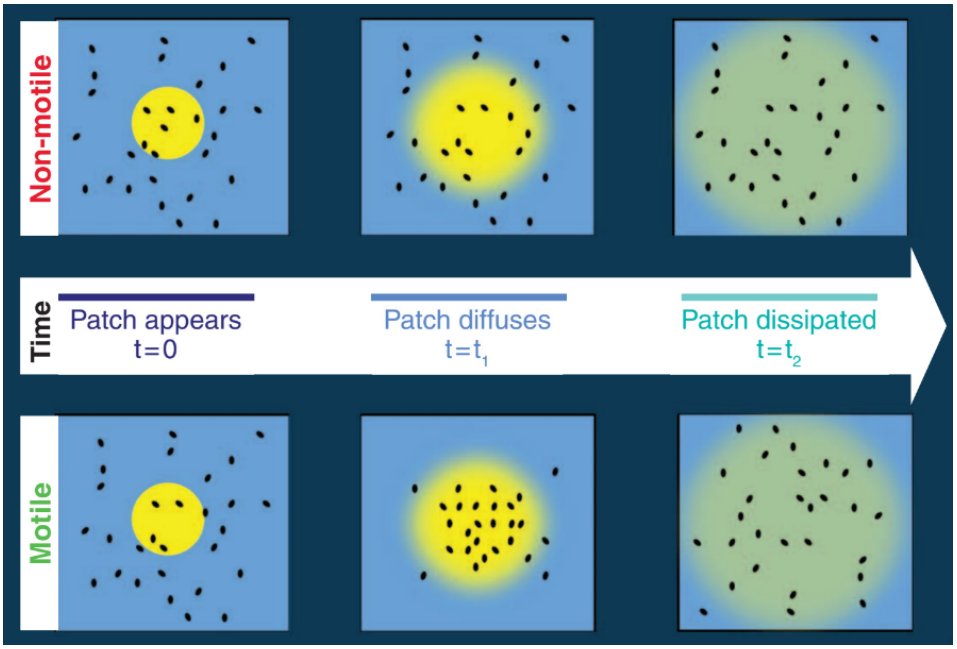

FIGURE 1.2. Cartoon highlighting the differences in nutrient patch exploitation in motile vs non-motile cells [8]. Yellow shaded region represents the diffusing nutrient over time, black dots are representative of cell positions. Note the motile cells enter the shaded region more quickly than non-motile counterparts.

1.3.1 Appendages

Microorganisms have developed the ability to move through the synthesis of thin motility appendages which either push or pull the body through the surrounding fluid or across a surface. As a result of the reversibility of fluid within this regime, the motion of these appendages is generally asymmetrical in some way, in order to generate a net movement in a particular direction. Most cells use either a single or few long, thin, rod-shaped flagella, which can either be rigid or flexible, or synthesize lots of shorter hair-like cilia.

1.4 Motivation

Swimming at micro-scales is very energetically expensive. Many microorganisms thrive without the ability to produce directed movement, simply encountering necessary nutrients through random diffusive motion. So why then have so many microorganisms evolved such a wide-range of motility appendages and swimming behaviours?

Several key laboratory bacterial species such as *Escherichia coli* and *Bacillus subtilis* have been relatively well characterised. Similarly, the swimming behaviours of some eukaryotes such as; *Chlamydomonas sp.* and *Dunaliella sp.* are reasonably well understood. Yet very little research has been undertaken to understand the swimming adaptations in archaea. Furthermore, the highly saline environments explored within this thesis represent a unique opportunity to explore micro-organisms living within low nutrient environments, where the relative cost of motility is much higher.

Recent developments in digital holography and other high-throughput techniques provide an opportunity to study organisms on a population rather than individual scale. These advancements enable the rapid, label-free imaging of thousands of cells simultaneously, in three-dimensions.

1.5 Thesis Outline

The remainder of this thesis will cover a variety of experimental, optical, and computer analysis techniques employed to understand the swimming behaviours of environmental microorganisms isolated from salt-rich habitats.

Chapter 2 - Explores the types of organism and natural habitats of all samples used within this study. Genetic analysis is applied to establish the individual species identities and genomic variations in the motility apparatus between study samples.

Chapter 3 - Provides an overview of the optical and holographic microscopy techniques used within experimentation. The optical set-up used within our lab is also outlined.

Chapter 4 - Details the computer analysis techniques necessary for reconstructing holographic images. Simulations of swimming and diffusing cells were created to test the accuracy of the bespoke software.

Chapter 5 - Discusses the preliminary experiments carried out to optimise cell culture methods prior to holographic motility experiments.

Chapter 6 - Is a key experimental chapter which explores the swimming behaviours of each of the samples, through digital holographic microscopy.

Chapter 7 - Provides a brief examination of all the material discussed, and an exploration into possible avenues for future study.

Chapter 2

Microbiology & Genetics

2.1 Introduction

Microorganisms are typically defined as single cells or cell clusters, smaller than 1 mm in diameter, that have the ability to carry out all essential life processes (growth, reproduction and metabolism) independently of other types of cell. These microscopic free-living cells are the fundamental life forms, from which all multicellular macroorganisms have since evolved [9]. Microorganisms are ubiquitous in every environmental niche known to man, constituting the majority of all biomass on earth. Consequently, they play a central role in virtually every ecosystem currently described to science, everything from; nutrient cycling, food production and preservation, disease, decomposition and photosynthesis are undertaken by unicellular organisms [9]. Without these tiny organisms, the intricate system of life on earth would be impossible.

All known life forms can be classified as belonging to one of three different domains, based upon the time at which they diverged from an unknown common ancestor which originally began life on earth. Each of these three domains; Bacteria (also known as Eubacteria), Archaea, and Eukarya, are then repeatedly divided up by genetic 'relatedness' until each unique individual can be defined as a distinct species. Eukarya are so named because they contain eukaryotic organisms, such as; animals, plants, fungi, protists e.t.c., which can be either single or multicellular organisms containing membrane-bound organelles (nucleus, mitochondria, golgi body e.t.c.). In comparison, both Bacteria and Archaea are unicellular and are termed prokaryotic, as they lack some of the organelles found in Eukarya and simply store their genetic material freely within the cytoplasm. However, Archaea and Bacteria differ significantly in the way they organise the

genes within their DNA, with Archaea encoding their genes in a more complex almost Eukaryotic manner. Archaeal genomes have often been referred to as having 'Eubacterial form and Eukaryotic content' [10]. Whilst this is not technically the case, Archaea are often considered to fall somewhere between the two domains sharing characteristics from both the Bacterial and Eukaryotic physiology [11]. It is because of these shared attributes, that Archaea are thought to have evolved from the common ancestor much earlier than their Bacterial and Eukaryotic counterparts.

2.1.1 Archaea

Archaea are widely accepted as being the most poorly understood of the three domains. Until the discovery of DNA sequencing in the 1970s [12], archaeal cells were characterised phenotypically, and as such were mistakenly categorised as members of the bacterial domain due to the physical similarities between the two groups. In 1977 Woese and Fox's formative work in genetics [13] established the third domain of Archaea creating a tripartite system, which now forms the foundation of how all life on earth is classified.

Like other microorganisms, Archaea are prevalent across the globe and can be found in almost all terrestrial and aquatic environments. Representatives have been isolated in a wide variety of ecosystems: ocean waters [14], freshwater sediments [15], soils [16], the human body [17] etc., the extent of their ubiquity is still being uncovered today. However, although archaea can be found in a diverse range of habitats, they are uniquely adapted to thrive in the most hostile environments on earth, places which are often too harsh to support any multicellular life at all. These environments range from deep-sea hydrothermal vents [18], to Antarctic sea ice [19], volcanoes [20] and salt plains [21], where they can be found in vast quantities. Archaea are often described by the conditions in which they most successfully thrive; Thermophile (temperatures > 45°C), Psychrophile (temperatures < 7°C), Acidophile (pH < 2), Alkaliphile (pH > 7), Barophile (living in high pressures) and Halophile (salinity > seawater) [22]. Archaeal species have been recorded surviving extreme temperatures ranging from -45°C to 121°C, pH levels of 0, and salt concentrations approaching saturation [23, 24]. Individual species are often found in high abundances, at levels of approximately 10^7 - 10^8 cells per ml [25]. The immense quantities of individuals present in these habitats, suggests that Archaea are major ecological components within global ecosystems. Furthermore, as a result of the high community density and low biodiversity, these extreme environments provide relatively simplistic ecosystems, enabling

the study of whole ecological networks with relative ease [26].

2.1.2 Halophiles

'Salt loving' or halophillic microorganisms are typically defined as those inhabiting environments with a salinity in excess of that of natural seawater (> 3.5 % dissolved salts). Halophiles can be roughly catagorised based on their optimum growth salinity; slight halophiles (2-5 % NaCl), moderate halophiles (5-20 % NaCl) and extreme halophiles (20-30 % NaCl) [27]. The halophillic organisms used within this thesis all lie within the extreme halophillic range.

An ecosystem with a high solute concentration can be considered extreme, as organisms must have developed specialized physiological characteristics in order to survive. Most organisms would dessicate at high salinities, consequently, halophiles have developed a number of strategies to enable efficient osmoregulation. The two most common physiological adaptations are known as; the 'organic-solutes strategy' and the 'high-salt-in strategy'. The organic-solutes strategy involves the organism actively removing salt from the cell, and producing organic solutes (which do not interfere with enzymatic activity) to match the environmental salinity gradient. This technique is highly energetically expensive, but provides the ability to withstand high fluctuations in osmolarity. In comparison, the 'high-salt-in strategy' involves the organism accumulating large quantities of KCl in the cytoplasm. This technique requires specialized intracellular machinery to cope with the increased salt, and prevent the denaturation of essential enzymes. Cells using this method of osmoregulation can typically only survive in highly saline environments [28].

Halophillic microorganisms are typically found in one of two types of salt-rich environment: salt lakes, or underground salt deposits (e.g. salt mines). However, some halophillic archaea have also been identified in food sources, such as table salt [29], green olives [30], fish sauce [31], and even isolated from the mucus within the human gastrointestinal tract [32].

Osmotic pressure often severely limits the biodiversity of salt-rich environments. Typically, the salt content of an environment is inversely correlated with the species richness [33]. Consequently, high salt environments often contain low species diversity, but the individual species are often found in high abundance within their respective habitats. However, an increase in archaeal diversity with increasing salinity (and depth) has been observed in some hypersaline environments [34]. Within these systems protozoa and other predators are typically

absent, but viruses can be common [35]. Despite the trophic simplicity of hypersaline habitats (when compared with other water-based ecosystems), very little is understood about species composition, interactions and nutrient cycling [36]. Furthermore, haloarchaeal cells have been shown to survive and remain viable in salt crystals for hundreds of years, perhaps indefinitely [35, 37]. It is generally accepted (though not fully understood) that in the absence of liquid, cells which can prevent dessication revert to a dormant metabolic state to enable long-term preservation within these halite crystals [38].

Most halophilic Archaea are aerobic chemoorganotrophs, able to utilise a range of amino acids and sugars as a growth medium. Given the low solubility of oxygen at high salinities, it is understandable that many haloarchaea are also able to survive anaerobically, for example; through denitrification [39] or fermentation in the presence of arginine [40]. Some halophilic archaeal species can also grow on a wide range of hydrocarbons (both aliphatic and aromatic) using them as the sole source of carbon and energy. This includes the ability to biodegrade crude oil, suggesting that haloarchaea could be used in the bioremediation of polluted saline environments [41].

Unlike most bacterial species, haloarchaea are typically pleiomorphic, displaying a wide array of shapes, often within an individual species; from flat disks [42], to rectangular [43], and a variety of rods and spheres [43]. Halophillic archaea can survive a wide range of temperatures (depending on the species), but they typically have a relatively high optimum growth temperature (35-50 °C) [44]. A culture temperature of 45° C was used throughout this work, as recommended by the halo-handbook [45].

2.2 Samples

Single celled organisms provide basic units for scientific study, which can often be scaled up for larger, multicellular organisms [46]. The ease of storing, growing and maintaining many microorganisms within the lab ensures straightforward, easily replicated experimental conditions.

The biological samples used within this project were extracted directly from their natural habitats, to ensure that any observed behaviours were not artefacts of generational adaptations to laboratory conditions. The archaeal cells were collected from one of two locations; The Great Salt Lake, Utah USA, or Boulby Potash Mine, Redcar, UK. In both cases, environmental samples of the liquid brine

were grown initially on 25% salt agar plates (see Appendix A) to provide mixed populations of indigenous microorganisms, then single colonies were extracted and re-cultured on new plates. A further single colony was extracted from each of these new plates before being grown in liquid media (see Appendix A) to saturation.

Given the extremely high salt concentrations within our sample environments, and previous species richness data [47, 48], it is highly probable that each of the sites has a very low biodiversity. Consequently, these archaeal species are likely to represent major components within their respective habitats.

2.2.1 Great Salt Lake

The Great Salt Lake (GSL) is one of the most-studied natural hypersaline environments in the world [49]. It is located in the Northern regions of Utah, USA (figure 2.1 left), and is the fourth largest terminal lake in the world (approximately 3900km^2). The lake has a maximum depth of approximately 10 metres during the winter/spring months, and drops to around 8 metres by late summer [50]. The GSL can be characterized as thalassohaline (pH 7-8) as its salt composition primarily stems from the natural seawater of its origin [44]. Seasonal water temperatures range from -5 °C to 45 °C [50].

FIGURE 2.1. *(Left)* Map of North America, red pointer denotes the position of the Great Salt Lake (scale bar = 2000 km) [51]. *(Right)* Satellite image of the Great Salt Lake, note the change in colour between the areas North and South of the railway. The red pointer denotes the location of the sampling site at the Spiral Jetty in the North Arm (scale bar = 20 km). Taken from Google Earth [51].

The GSL can be regarded as two very distinct ecosystems, due to the rail-road causeway constructed in 1959 which bisects the lake laterally into north and south arms (figure 2.1 (right)) [52]. After the installation of the rail-road, the northern arm has become steadily more hypersaline, whereas the southern arm more dilute (table 2.1). The north arm has very little freshwater input, and as such currently has an extremely high salinity close to saturation (up to 30% w/v). Whereas the larger southern arm has a much lower salinity (between 9-15% w/v) due to a regular freshwater supply from three rivers fed by melting snow from the Wasatch Mountain Range [53]. This southern section of the lake, although more saline than seawater, cannot be considered truly hypersaline.

TABLE 2.1. The changes in the average dissolved salt concentrations (g/l) before and after the construction of the rail-road causeway [53, 54].

	Pre Causway (1910)	North Arm (2004)	South Arm (2004)
Total Solids	$242.43\,g\,l^{-1}$	$313.68\,g\,l^{-1}$	$175.26\,g\,l^{-1}$
Chlorine	$126.35\,g\,l^{-1}$	$175\,g\,l^{-1}$	$95\,g\,l^{-1}$
Sodium	$85.1\,g\,l^{-1}$	$101\,g\,l^{-1}$	$59\,g\,l^{-1}$
Sulphate	$16\,g\,l^{-1}$	$22\,g\,l^{-1}$	$13\,g\,l^{-1}$
Potassium	$8.82\,g\,l^{-1}$	$6.9\,g\,l^{-1}$	$3.4\,g\,l^{-1}$
Magnesium	$5.18\,g\,l^{-1}$	$8.5\,g\,l^{-1}$	$4.6\,g\,l^{-1}$
Calcium	$0.98\,g\,l^{-1}$	$0.28\,g\,l^{-1}$	$0.26\,g\,l^{-1}$
Salinity	21.32 % w/v	30 % w/v	15 % w/v

The GSL plays host to a wide variety of both indigenous and migratory fauna. The southern arm typically houses large populations of brine shrimp and brine fly (*Artemia franciscana* and *Ephydra sp.*, respectively) two key species of phytoplankton (*Dunaliella viridis* and *salina*), and numerous water and migratory birds [26]. Furthermore, there is a high abundance of microscopic life, including several species of phytoplankton, rotifers, nematodes, ciliates, crustacean zooplankton, bacteria and archaeal species [26, 27]. Whereas, due to its much higher salinity, the northern arm has a much lower biodiversity. The only organisms typically found in the north arm are; a few representatives of the bacterial and archaeal domains, with a sole eukaryotic resident, the phytoplankton *Dunaliella salina* a species well known for thriving in hypersaline conditions [26]. The algal species *Dunaliella salina* produces huge quantities of glycerol for osmotic stabilisation, and so are thought to provide the main carbon source for the halophillic archaea and bacteria within this salt lake system [36].

The archaeal samples used within this study were isolated from the hypersaline North Arm of the Lake. Specifically, the waters surrounding the 'Spiral Jetty' towards the eastern bank of the north arm of the lake (figure 2.1). The archaeal species within this section of the lake are responsible for giving it the 'pinkish hue', indicative of the red rhodopsin-based pigment typical of haloarchaeal species. The north arm of the lake represents one of the most hypersaline natural environments on earth [27], and as such has relatively low nutrient availability.

2.2.2 Boulby Potash Mine

Boulby Potash Mine (BPM) is located on the north east coast of England (figure 2.2 (left)). BPM is the deepest mine in the UK (1.1 km deep), and is a working potash, polyhalite and rock-salt mine (figure 2.2 (right)). However, it is also of high scientific value to the UK, because its depth and isolation provide an opportunity for a variety of ultra low radioactivity and deep underground scientific experiments [55]. The existing research facilities and underground laboratory make it an ideal place to study halophile behaviours.

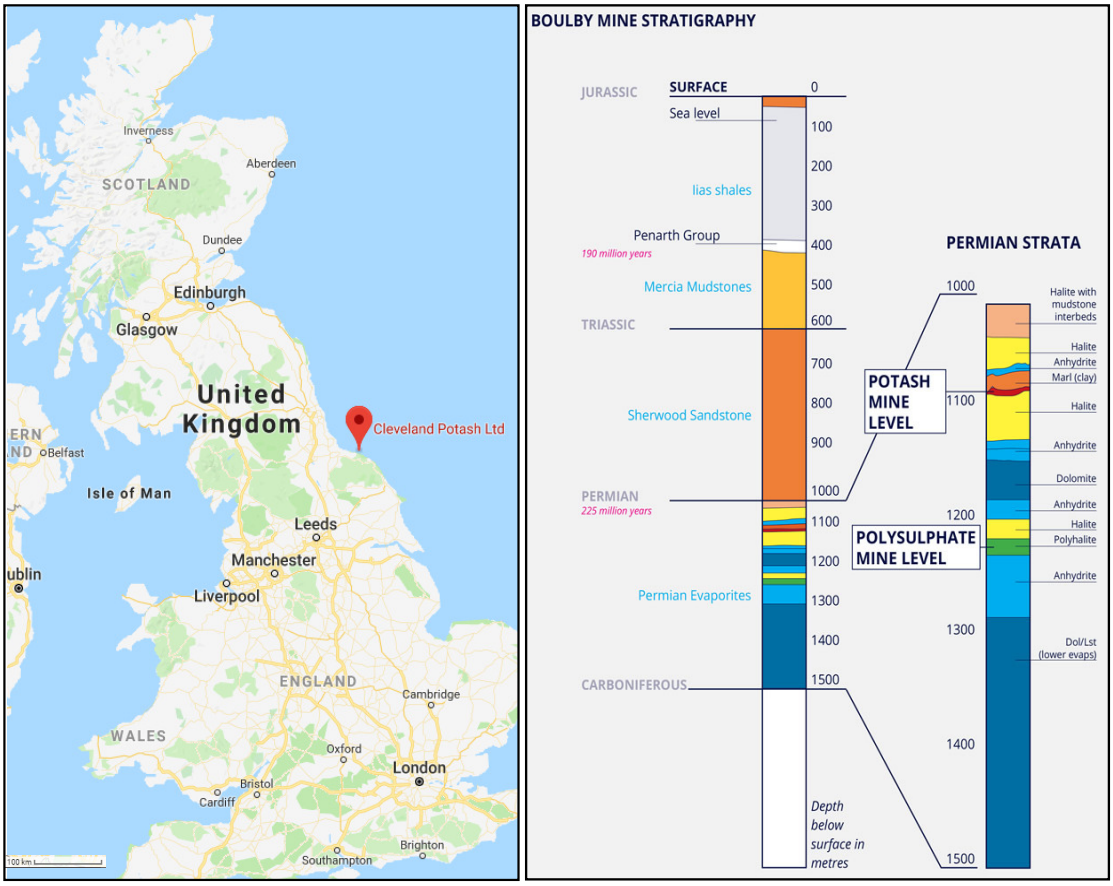

FIGURE 2.2. *(Left)* Map of the United Kingdom, red pointer denotes the position of Boulby Potash Mine (scale bar = 100 km). Taken from Google Earth [51]. *(Right)* Geological layers in Boulby Potash Mine, samples were extracted from the potash layer at 1100 m below sea level. Figure from [56].

As a result of its depth, the mine has a fairly stable temperature of between 40-42 °C [47]. The salt in BPM originated from natural seawater, created through the evaporation of the Zechstein Sea, around 230 million years ago in the Permian era [55]. The nature and distribution of organic matter within ancient salt deposits is largely varied and can be very sparse, making the available and usable carbon for microorganisms unpredictable, and significantly lower than within surface brine environments [57].

The microbial composition of the salt deposits within the vast area of the mine remain a mystery. Localised studies have revealed very low densities of unidentified archaea (2×10^2 to 5×10^6 cells per ml^{-1}) [47], but no other organisms have been isolated to date. Whilst there is the possibility that the archaea found within the mine could have been seeded there since the start of its operation in

1973, this is thought to be unlikely due to the lack of halophillic environments within the surrounding area, diversity of organisms found, and several studies failing to culture archaea from mine air [47, 57]. Consequently, the current leading hypothesis is that the archaeal cells residing within the rock salt and liquid brine seeps in Boulby salt mine originated millions of years ago (Permian era), and have been preserved within the halite crystals since before dinosaurs walked the earth.

The samples used within this thesis were collected from brine seeps within the potash layer of BPM (figure 2.2. The sampling site was located slightly off the coast of the UK, under the North Sea, in a disused/abandoned area of the mine.

2.2.3 Sample Storage and Culture

Solid agar plates of Modified Growth Media (MGM) [45] at 25 % dissolved salt (full media recipe in appendix A) were inoculated with brine samples from each of the sampling sites and incubated at 45 °C until single colonies appeared. From each plate a single colony was removed and streaked onto another 25 % MGM plate and incubated. Upon growth, a single colony was removed from this new plate and cultured to saturation in liquid MGM (appendix A). All liquid cultures throughout all experiments were incubated at 45 °C in an orbital shaker at 150 rpm until the required growth stage was achieved.

Modified Growth Medium (MGM) was initially chosen due to its high nutrient content, which provides a rich media for a wide array of halophillic archaea, and promotes rapid growth rates. When preparing the growth medium Oxoid-Peptone was selected over the more commonly used Bacto-Peptone, as the latter has been shown to contain bile salts which lyse many haloarchaeal cells [58]. Furthermore, all media stocks were adjusted to pH 7.5 prior to sterilisation (and rechecked afterwards), through the addition of Tris base or Tris HCl. Both liquid and solid media were autoclaved on a liquid cycle for 30 minutes (101 kPa above atmospheric pressure). Liquid media was then stored in airtight containers at room temperature prior to use, and discarded should salt precipitation occur. Solid medium was poured into 1 cm thick plates (under sterile conditions), wrapped with Para-film and left for 24 hours upside down at room temperature [45], before either being used or refrigerated for long-term storage.

For long term-storage, after reaching saturation in liquid media, samples were combined with a glycerol salt water stock solution (Appendix B) and stored at -80 °C to create a frozen stock. Frozen cells are thought to remain viable for

a minimum of 20 years [45]. This frozen culture stock formed the basis of all experiments, with ice scrapings being cultured in liquid MGM to saturation and refrigerated (4 °C). Cells removed from this refrigerated stock were re-cultured in liquid media for all experimentation. The 'fridge stock' was replaced regularly, though haloarchaeal cells have been shown to remain viable for 1-2 years in sealed containers at either room temperature or refrigerated [45].

2.3 Sample Identification

With millions of species of microorganisms currently recorded, and conservative (albeit somewhat controversial [59, 60]) predictions suggesting there may be upwards of one trillion unidentified species across the globe [61], accurately identifying individual samples is of vital importance. Phenotypically, many microorganisms look and behave the same, making samples extracted directly from the environment impossible to identify with any existing visual techniques. The only reliable way to accurately define microbial samples is through genetic (DNA + RNA) sequencing. In prokaryotic microorganisms this is usually achieved by comparing a specific region of the genetic code, known as the 16S ribosomal RNA (rRNA). RNA has similar properties to DNA, but is single-stranded and contains slightly different sugars and bases to DNA. The 16S rRNA is a highly conserved section of RNA found in the ribosomes of the cell, which contains information about the evolutionary history of the cell. The information contained within this region varies only slightly between individuals that are closely related, but vastly between members of unrelated organisms [9].

2.3.1 Genetic Sequencing

Deoxyribonucleic acid (DNA) sequencing is a biochemical technique that determines the order of the four base types (adenine, guanine, cytosine and thymine (uracil in RNA)) within the deoxynucleotide triphosphates (dNTPs) that make up a particular section of DNA (or RNA). The basic technique involves selecting a section of artificially synthesised complementary DNA (primer) which overlaps the region of interest within the sample of DNA under investigation. This primer, the DNA sample and free nucleotides are placed in a cycle reaction known as PCR (polymerase chain reaction) (figure 2.3). First the DNA is heated to break the hydrogen bonds, causing the two strands of the double helix to separate. The solution is then cooled to allow the primer to bind to the DNA (annealing), before being warmed to an intermediary temperature to facilitate the binding of the free

nucleotides to the end of the primer (extension). This process is repeated several times to generate a high concentration of DNA fragments containing the region of interest (figure 2.3) [9, 62].

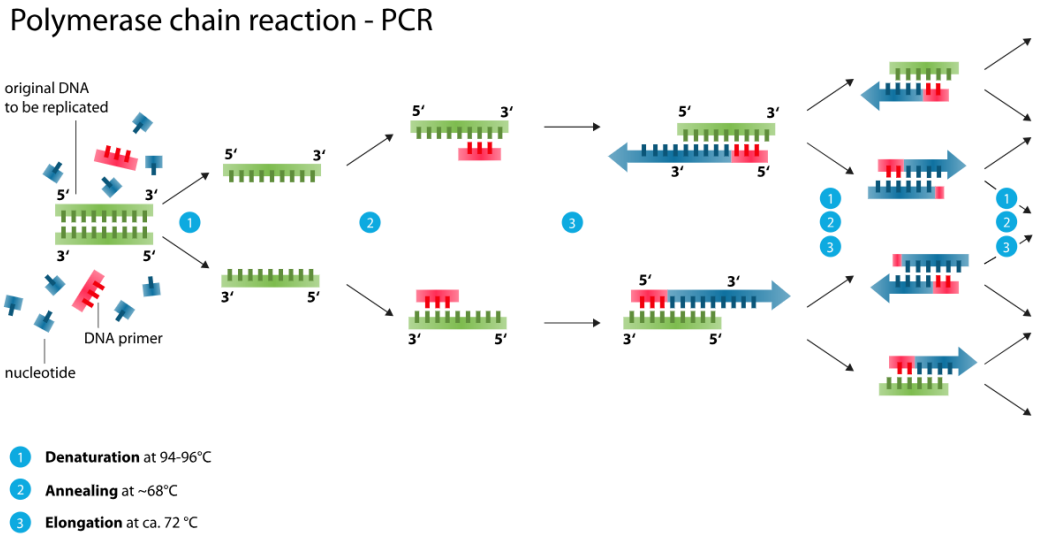

FIGURE 2.3. Schematic drawing highlighting the key steps involved in polymerase chain reaction. When using PCR for genetic sequencing, the standard nucleotides are combined with fluorescently labelled nucleotides to enable base-type identification [63]

The sequencing step requires the addition of fluorescently labelled nucleotides to the PCR solution. These labelled nucleotides compete with the unlabelled ones, to bind to the DNA. Consequently, they bind at random intervals on each DNA fragment, and prevent the addition of any nucleotides after that point, creating fragments of DNA of varying lengths. The fragments in the resulting mixture are then separated by size (electrophoresis see section 2.3.3), and the labelled nucleotides are excited using laser illumination. The base type at the terminating point of each fragment is then identified using four-colour detection of the emissions, and the original sequence can be computationally reconstructed.

In recent years, automatic, machine-based sequencing has started to become the norm. These 'Next Generation' technologies, require much less human input to produce accurate reads, and are becoming much faster and cheaper to execute. As these technologies improve, rapid, whole genome sequencing is becoming easily accessible, making comprehensive genome analysis more readily available than it was just a few years ago [62].

When sequencing the samples within this thesis, the 16S rRNA was initially extracted from the DNA and analysed. However, due to the unspecific primers used, and the short section of rRNA analysed (approx 500 base pairs), it was impossible to accurately identify the species with this method. Consequently, a further analysis was conducted to sequence the whole genome of each of the samples under investigation. The remainder of this chapter will discuss the methodology and results from this full-genome sequencing.

2.3.2 DNA Extraction

DNA was extracted from the archaeal cells using the standard technique of ethanol precipitation recommended for halophiles [53], with STE buffer used in place of phenol. The following protocol was employed for each of the environmental samples in turn.

200 μl of stationary phase liquid culture was centrifuged at 10,000 ×g for 2 minutes to concentrate the cells within a solid pellet. The supernatant containing the growth media was removed and the pellet was resuspended in 200 μl of purified (Milli Q) water. Due to the high salinity the cells, the addition of pure water served as the simplest and most effective way to lyse the cells, without damaging any genetic material. 200 μl of STE Buffer (Sodium Chloride, Tris Base, Ethylenediaminetetraacetic acid, and purified water (See Appendix C)) was added to separate the proteins from the remaining cell matter. The solution was incubated at 65 °C for 60 minutes, then centrifuged (10,000 ×g) for 5 mins. The aqueous top phase was removed and added to 400 μl of 100 % ethanol (pre-chilled), vortexed and allowed to precipitate on ice for 10 minutes. The solution was centrifuged for 10 minutes (10,000 ×g) the ethanol was then removed and the precipitate was washed with 1 ml of 70 % ethanol, and re-centrifuged (10,000 ×g, 10 mins) before the ethanol was removed. The resulting pellet was allowed to dry and re-suspended in 50 μl of DI water.

DNA was purified to remove any remaining salts and/or proteins, using a Nucleospin PCR clean-up kit [64]. The 50 μl of extracted DNA was combined with 100 μl of standard binding buffer NT1 in a PCR collection tube, and centrifuged for 30 seconds (11,000 ×g). The NT1 buffer facilitated the binding of DNA to a silica membrane matrix within the collection tube, allowing the buffer itself to pass through the membrane into the bottom of the tube. 700 μl of NT3 wash buffer was then added to the filter to remove any remaining contaminants, and re-centrifuged (11,000 ×g, 30 sec). This washing step was repeated a second time

with an additional 1 minute of centrifugation to ensure high DNA purity. After each step the flow-through was discarded. Finally, 25 μl of elution buffer NE was added to the filter to release the DNA from the silica membrane. The solution was incubated for 1 minute and centrifuged (11,000 ×g, 1 minute), producing a final sample of highly pure and concentrated DNA. 2 μl of each sample was analysed using a micro-volume spectrophotometer (NanoDrop), to check the DNA concentration and purity (table 2.2). It is common practice to measure purity as the absorbance of a sample at 260 nm wavelength, divided by the absorbance at 280 nm. This is due to the propensity of proteins and other contaminants to absorb strongly at the 280 nm wavelength, with DNA having a maximum absorption at approximately 260 nm (each different nucleotide base varies slightly) [65]. DNA and RNA samples are typically considered 'pure' (having a low level of contamination) if the ratio A260:280 falls between 1.8-2.2 [66]. Values lower than this would indicate high protein content and require further purification steps [65]. Finally, each sample was diluted with elution buffer to reach close to the maximum required levels for sequencing (10-100 ng/μl) (table 2.2).

TABLE 2.2. DNA concentration and purity levels before submission for sequencing. The NanoDrop spectrophotometer has an accuracy of around 2 % [67], however, readings may be slightly less accurate if the solutions were non-homogeneous.

	DNA Concentration (ng/μl) Before Dilution	A260:280	DNA Concentration (ng/μl) After Dilution
A	113.5	1.908	97.0
B	148.5	1.954	97.0
C	232.0	1.991	98.0
D	169.0	2.012	94.0
E	227.0	2.018	95.5
F	223.5	2.023	99.5
X	176.5	1.972	93.0
Y	157.5	1.921	97.0

2.3.3 Gel Electrophoresis

The size of the DNA fragments were checked via gel electrophoresis. Samples of DNA were combined with glycerol and TBE buffer for stabilization, and a loading dye (bromophenol blue and xylene cyanol FF) to enable visual tracking of DNA migration during electrophoresis. The samples were inserted into small wells in a submerged agarose gel. Cathodes attached at either end of the tank containing the gel generate an electrical current which was passed through the gel (from top to bottom). Nucleotides (which are negatively charged) migrated through

the gel, towards the positively charged cathode. This separated the different fragments of DNA within the sample by size. Smaller fragments of DNA travelled more quickly down the gel creating bands of genetic material of different sizes at various positions along the gel [9].

The gel used within experimentation was a standard 1 % Agarose gel (5 ml TBE buffer (×10), 0.5 g Agarose, 45 ml Milli Q water and 10 μl SYBR safe), prepared and poured into a rectangular mould. A comb placed within the mould created wells horizontally along the top of the gel. The agarose was allowed to set for approximately 45 minutes (shorter setting times can lead to smearing), and submerged a tank containing 0.5 × TBE (Tris-Borate-EDTA) buffer. 4 μl of each sample was loaded into wells and the gel was set to run at 100 V for 35 minutes (figure 2.4). In the two outside lanes of the gel, samples containing nucleotide chains of known sizes (DNA ladders) were inserted, to provide an approximate measure of sizes of the DNA fragments within the samples.

The samples of DNA were prepared as follows;

- 6.83 μl DNA sample
- 1.67 μl loading dye (purple)
- 1.0 μl 80% glycerol (filter sterilized)
- 1.0 μl TBE buffer (×10)

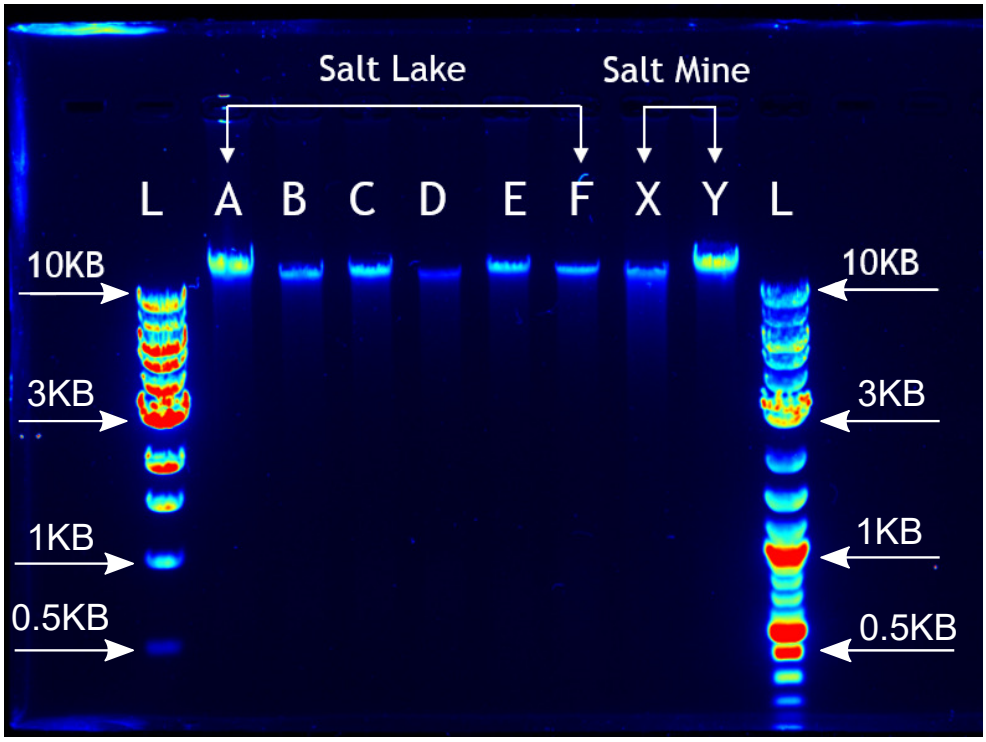

FIGURE 2.4. Archaea DNA Electrophoresis. L represents the two ladders used to measure the position of the bands. Each of A-F represent the DNA for the Great Salt Lake Samples, with X and Y representing the samples extracted from Boulby Potash Mine. The more intense the colour, the higher the concentration of DNA of that size present.

After running for 35 minutes the gel was removed and illuminated with UV light. The resulting image was photographed and artificially coloured to highlight the bands. SYBR safe was chosen over the standard ethidium bromide to stain the agarose gel as it is significantly less hazardous (i.e non-carcinogenic). The stain is designed to fluoresce under ultraviolet illumination, allowing observation of the bands.

Figure 2.4 shows clear bands near the top of the gel with only very slight smearing. This indicates that the fragments of DNA within all of the samples are very large (>10,000 base pairs). The intense levels of florescence show that the DNA is relatively well concentrated as the SYBR safe dye has bound effectively. Furthermore, the low levels of smearing/the appearance of single bands suggests there are few fragments smaller in size. The combination of these attributes suggest that the DNA is of suitable quality for sequencing.

2.3.4 DNA Sequencing

DNA sequencing was outsourced to a genetics laboratory (Microbes NG, University of Birmingham, UK) that specialises in the full-genome sequencing of prokaryotic microorganisms. Samples of the purified DNA were sent to the laboratory for analysis. The resulting data-files were then imported into Snap Gene Viewer (version 4.1.9) open source software for easy interpretation. Individual genes or whole contigs (large section of consecutive bases producing multiple consecutive genes) could then be selected via this software and compared with known sequences within the BLAST (basic local alignment search tool) database [68]. The BLAST search tool compares the nucleotide order within a section of DNA with that of those within the database. Genes are then returned alongside a value for the % likelihood of a complete match, based upon any gaps or mismatches in the alignment of the sequences, the length of the sequence under investigation and the percentage coverage of the match, to the query sequence.

2.4 Results

Whilst samples A-F (Salt Lake) and sample X (Boulby Mine) returned high-quality reads form the sequencing process, sample Y returned a huge datafile comprising of mostly short contigs, indicative of contamination with one or more other species. Consequently, sample Y was disregarded from any further analysis or experimentation at this point. Samples A-F and X each produced long contigs (complete sections of DNA) the longest of which was over 1 million base pairs for each species sequenced.

2.4.1 16S rRNA

The 16S rRNA genes were located within the data-files, for each of the samples sequenced, using Snap Gene Viewer. These genes were extracted and compared with one another, alongside known sequences for *Haloarcula hispanica* and *Sulfolobus acidocalarius* from the BLAST database. *H. hispanica* was selected as preliminary investigations suggested that it would be a close relative to the samples, whereas *S. acidocalarius* is a key laboratory species and was included as an unrelated archaeon for comparative purposes. A phylogenetic tree highlighting the relatedness of the genes was produced (figure 2.5) using the software CLC Sequence Viewer (version 7.8). This was generated using a neighbour joining algorithm based on the Jukes-Cantor model [69], with 100,000 bootstrap replicates.

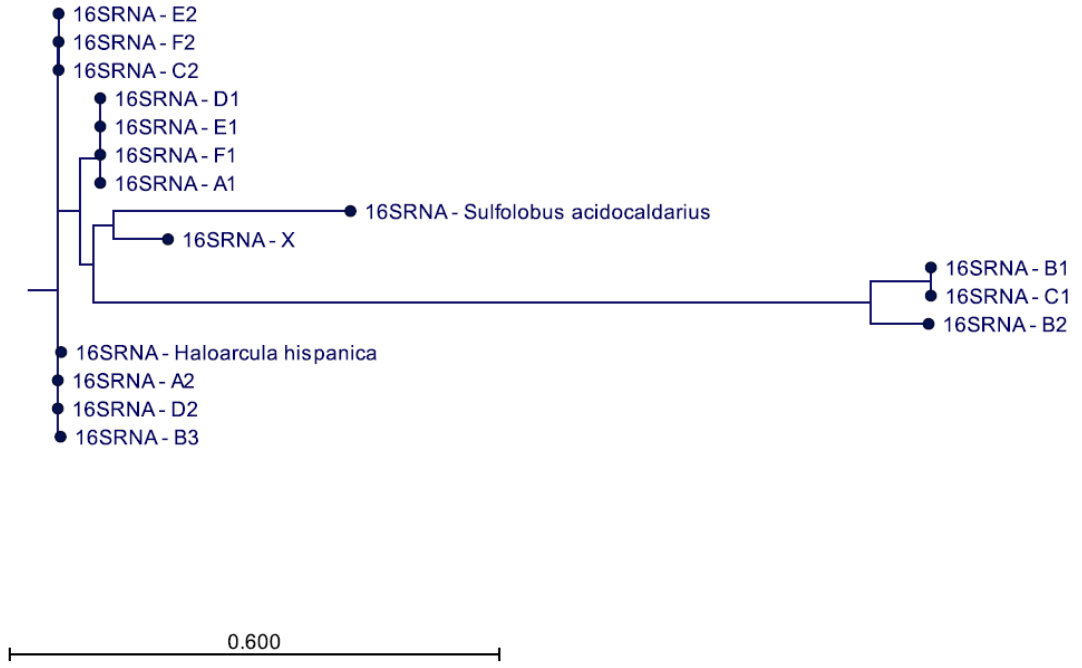

FIGURE 2.5. 16S rRNA Phylogenetic Tree of each sample sequenced, constructed using a nearest neighbour algorithm, based on the Jukes-Cantor distance measure. The scale bar represents a genetic distance of 0.6 substitution per nucleotide [69]. Multiple copies of the 16S were found within many of the samples sequenced.

Typically, organisms contain only one version of the 16S within their DNA. However, each of the samples isolated from the Great Salt Lake contained multiple copies of the 16S, each displaying high levels of genetic variation. Note that in figure 2.5 some of the 16S genes showed greater genetic variation than the 16S from *S. acidocalarius*, an unrelated species. Given that each version of the 16S was found within the same contig, it is highly unlikely that they are the result of any contamination or other experimental error.

All organisms experience a degree of genetic variation between individuals within the same species. These genetic variations form the basis of evolution, with beneficial traits becoming adopted into the genomes of future offspring. However, this intra-genomic heterogeneity is much larger within halophilic archaea, compared with bacterial and other archaeal phyla. This intra-species genetic diversification is primarily due to lateral gene transfer rather than DNA mutations [70]. The high levels of DNA exchange found in halophillic archaea have been largely attributed to homologous recombination, environmental transformation

and cell fusion [70, 71]. Homologous recombination refers to the swapping of genetic material within an individual. Whereas environmental transformation (figure 2.6 (left)) and cell fusion (figure 2.6 (right)) involve swapping of sections of DNA between individuals from the same, or even different species. Individual cells can either take up environmental DNA released from cell lysis (transformation), or bind to living organisms and exchange genetic material (cell fusion) [71].

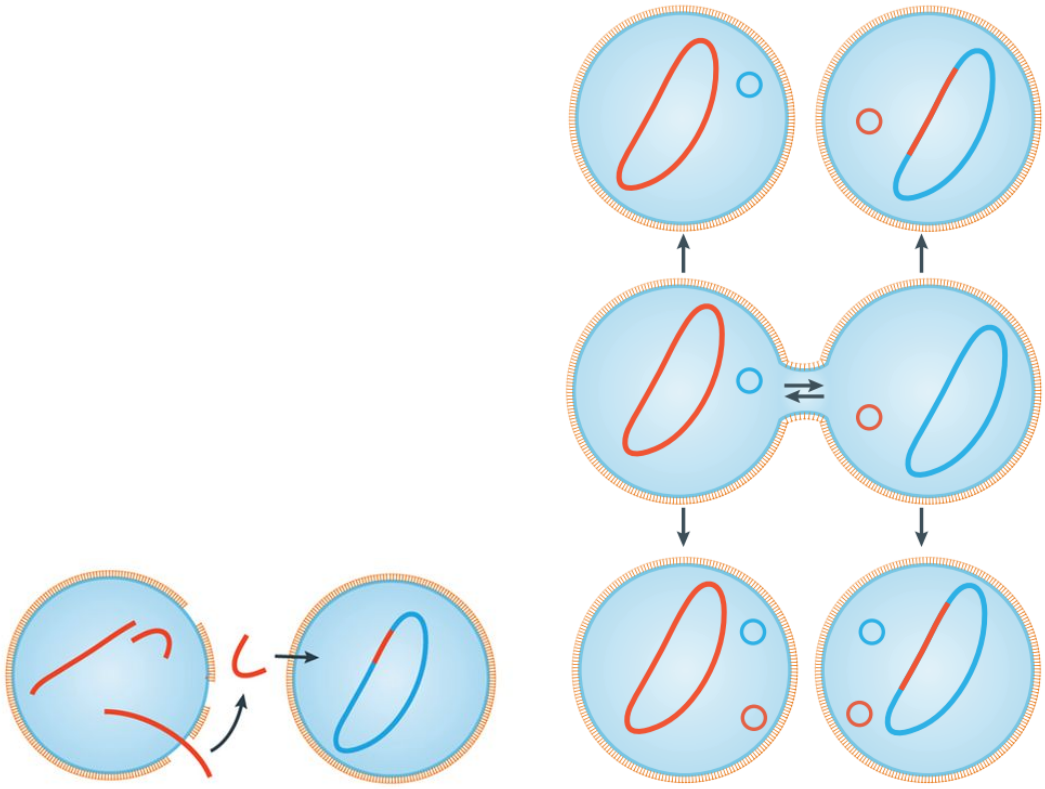

Figure 2.6: Left: DNA transfer via environmental transformation. Right: DNA transfer via cell fusion in archaea. Figure adapted from [71].

Halophiles have been found to have highly divergent 16S rRNA genes, with approximately 50 % of all strains containing two or more variants of the 16S within a single species [72]. The levels of genetic divergence within the 16S rRNA of haloarchaea far exceeds the divergence found in bacterial species, and is in line with expected values for divergence between different genera within a family [73]. Therefore, the 16S rRNA genes alone cannot be reliably used as a species indicator in studies with environmental haloarchaeal samples [74]. It has been suggested that these high levels of genetic exchange may be an evolutionary strategy within extreme environments, as particular copies of 16S rRNA have been expressed in varying temperature conditions [75].

2.4.2 Largest Contig

In order to reliably ascertain the species of each of the samples, the largest contig from each sample was compared against the BLAST database. Table 2.3 shows the size of the contig analysed (archaea DNA is approximately 3-5 million bp in total [76]) and the best match for each sample.

TABLE 2.3. Table of results from the largest contig BLAST database search.

	Largest Contig Size	Highest Species Match	Percentage Match
A	1,321,866 bp	*Haloarcula hispanica*	98 %
B	1,441,152 bp	*Haloarcula hispanica*	98 %
C	1,321,893 bp	*Haloarcula hispanica*	98 %
D	1,310,683 bp	*Haloarcula hispanica*	98 %
E	1,321,906 bp	*Haloarcula hispanica*	98 %
F	926,487 bp	*Haloarcula hispanica*	98 %
X	804,485 bp	*Haloferax volcanii*	93 %

These results suggest that all of the samples received from the Great Salt lake are of the species *Haloarcula hispanica*, and the single isolate from Boulby Potash Mine is likely to be *Haloferax volcanii*. Both species have been successfully cultured in laboratory conditions before, and have previously been isolated from similar environments.

2.4.3 *Haloarcula hispanica*

Members of the genus *Haloarcula* are typically pleiomorphic flat rod shaped cells, that are motile under normal conditions. They have the ability to utilise an array of simple sugars as carbon sources, and although are preferentially aerobic, they can respire anaerobically in anoxic conditions [43]. *Haloarcula hispanica* was originally isolated from a solar saltern in Spain [77], but has since been discovered in multiple locations [58].

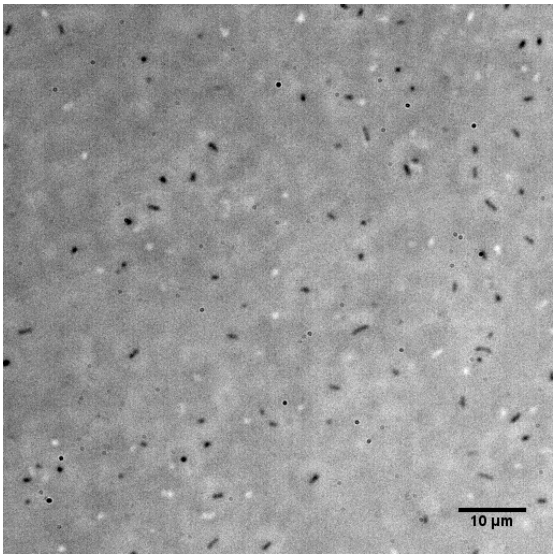

FIGURE 2.7. A phase contrast image of *Haloarcula hispanica* taken using 60 × magnification objective, with and additional 1.5 × eyepiece lens. Cells used in this figure were cultured using the standard protocol (section 2.2.3) in 25 % MGM. The scale bar represents 10 micrometers.

2.4.4 *Haloferax volcanii*

Haloferax volcanii was originally isolated from the sediments of the Dead Sea, and takes its name from the scientist who originally isolated and cultured it [78, 79]. Individuals are typically flat-disk shaped, or curved to create a cup-like shape [42]. However, like many haloarchaeal species, individuals are pleiomorphic with coccoid and other cell shapes also being reported [42]. This species is capable of growth in both aerobic and anaerobic conditions. *Hx. volcanii* grows well on a range of amino acids and sugars, and can use nitrate, Dimethyl sulfoxide (DMSO) and Trimethylamine N-oxide (TMAO) when switching to anaerobic respiration [79]. Due to it's ease of laboratory culture, and useful gene organisation, *Hx. volcanii* has become a model organisms for the study of haloarchaeal genetics [80].

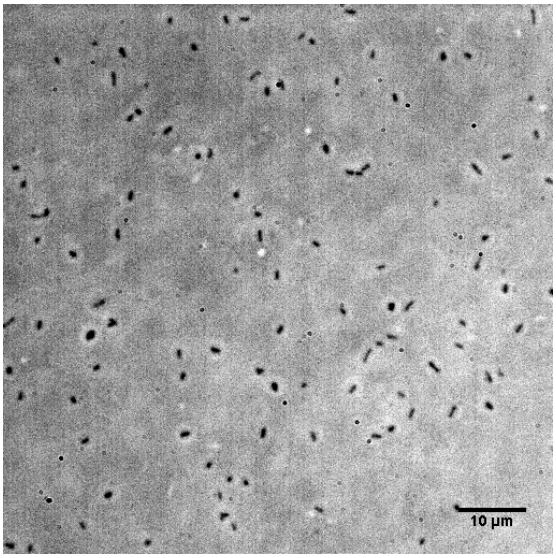

FIGURE 2.8. A phase contrast image of *Haloferax volcanii* taken using 60 × magnification objective, with and additional 1.5 × eyepiece lens. Cells used in this figure were cultured using the standard protocol (section 2.2.3) in 25 % MGM. The scale bar represents 10 micrometers.

2.5 The Archaellum

Most motile archaea propel themselves through their fluid environment using one or more helical appendages. These appendages are phenotypically similar to the bacterial flagellum, and so were originally named 'archaeal flagellum'. However, recent studies have shown that the 'archaeal flagellum' is more closely related to the type IV pillus on both an evolutionary and molecular basis [81]. Consequently, the widely accepted name was modified to 'archaellum' in an attempt to signify the uniqueness of this motility structure [82].

The archaellum is a rigid, right-handed helical filament, attached to the cell body via a rotary motor [83]. Some species of archaea have a flexible hook connecting the filament to the body (as is the case with bacterial flagella), but for many archaeal species this is absent [84]. The filament itself is slightly thinner than the bacterial flagellum, 10-14 nm compared with 18-22 nm, respectively. The rotary motor is ATP driven, and able to switch between clockwise and counter-clockwise motions [82].

2.5.1 Fla Genes

The archaellum is constructed via a number of Fla genes which synthesise the rotary motor and flagellin appendage (figure 2.9). Fla A and Fla B are responsible for producing the flagellin subunits which form the filament structure of the archaellum. Fla F, G, H, I and J are all involved in the construction of the archaella motor (figure 2.9), and Fla C-E are responsible for signal transduction between the motor and the chemotactic network [81, 85]. These individual structural genes were located within the sequencing data of each of the samples, by searching the genome for example sequences from the BLAST database.

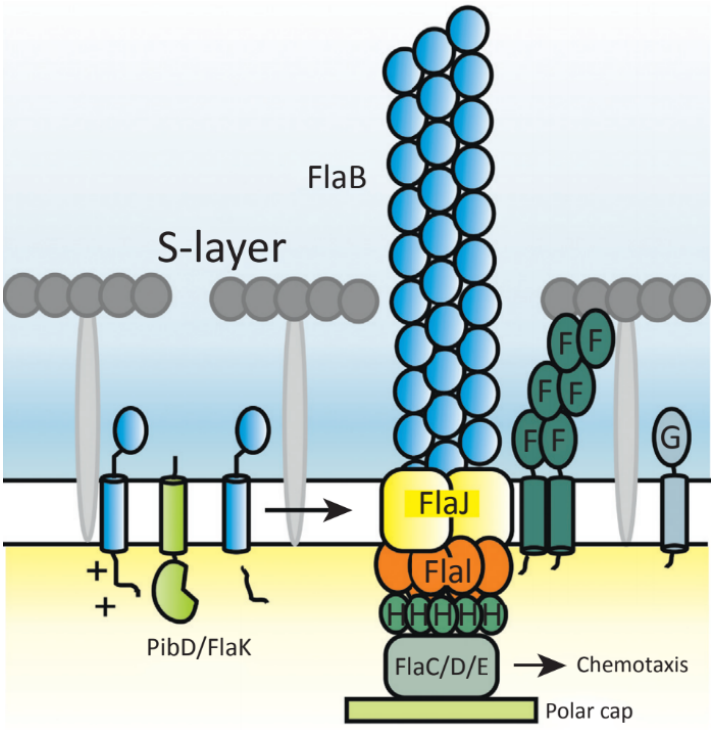

FIGURE 2.9. Archaellum structure, depicting the position of each of the known Fla genes in a Euryarchaeota archaellum. Figure taken from [85].

Figure 2.10 shows the structural Fla genes found within three of the environmental haloarchaeal samples. The general motor structures showed only slight variations in the nucleotide composition, resulting in the same Fla genes being produced. In comparison, the flagellin filament proteins were different between each of the samples. *H. hispanica* B had both Fla A and Fla B flagellin producing genes, whereas *H. hispanica* F and *Hx. volcanii* X each had only one type of flagellin, Fla B and Fla A, respectively. None of the samples sequenced had the

archaella hook producing gene Fla B3 [81]. Samples A, C, D and E produced identical genes to sample F, and so were omitted from further study.

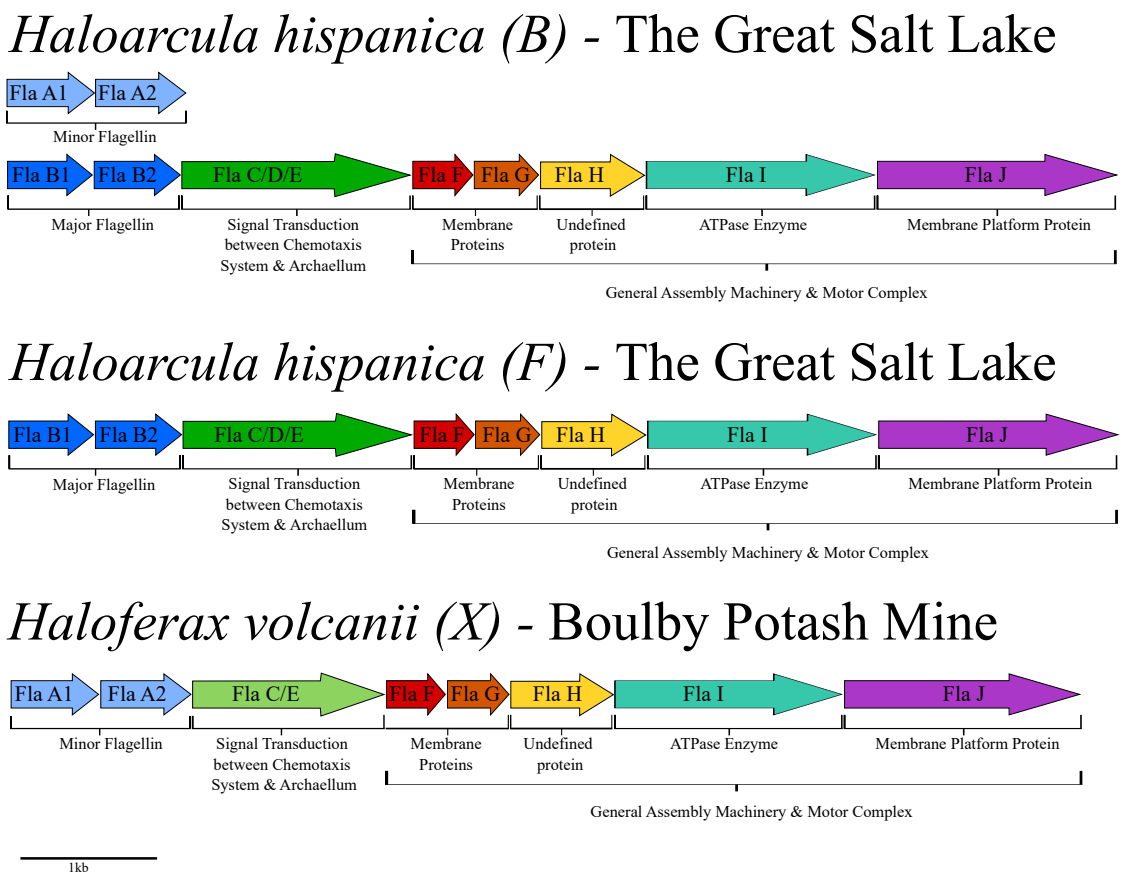

FIGURE 2.10. Archaella gene locations and sizes for *Haloarcula hispanica* samples B and F, and *Haloferax volcanii* sample X. The arrows size is representative of the number of bp within each gene (scale bar shows 1,000 bp). The different colours highlight the different genes, with shade variations of the same colour denoting homologous genes. Arrows placed above the others denote genes positioned in a different region of the genome.

H. hispanica B is of particular interest as the additional flagellin producing genes adopted within the genome are most likely a result of genetic transfer from another species, either by environmental transduction or cell fusion. Multiple flagellins within the same genome can be utilised interchangeably to create structural changes in the archaellum filament in response to differing environmental conditions [86]. Consequently, the swimming behaviours of sample B may vary as a result of these changes, when compared with sample F of the same species.

2.6 Discussion

Initial attempts to sequence the 16S rRNA of the sample organisms produced inconclusive results. This may have been in part due to the relatively small region selected. However, after completing the full-genome analysis and exploring the 16S rRNA regions of the samples, several variants of the 16S were isolated within many of the samples. This high level of heterogeneity within individual samples would have made species identification through the 16S alone challenging, if not impossible.

The full-genome sequencing yielded strong reads with long contigs, indicative of reliable data. From the largest contigs the species of each of the samples could be established. These large contigs represented approximately $\frac{1}{4}$ of the whole genome, so provided strong matches with previously recorded species (table 2.3). Unfortunately all of the samples extracted from the Great Salt Lake were the same species. Furthermore, one of the two samples collected from Boulby mine was a mixed population, and therefore unsuitable for further analysis.

The samples collected from Boulby mine represent the first full-genome sequencing of any organisms collected from that site. Furthermore, these cells are likely to have remained largely undisturbed (possibly in a dormant state) for millions of years. Furthermore, this is the first record of *Hx. volcanii* being isolated from Boulby Potash Mine.

The motility structure genetic analysis revealed that whilst the archaellum motor structure was almost identical across the samples, the filament structure varied significantly. Furthermore, sample B was shown to have adopted additional genetic information into its genome. Whilst this is thought to be very common amongst halophillic archaea, it has been suggested that the additional genes can be expressed under different physical conditions [75]. Whilst there have been no direct studies, evidence suggests that these additional flagellins could alter the structure of the filament [81] and subsequently affect the swimming behaviours of *H. hispanica* sample B, when compared with *H. hispanica* sample F.

The absence of a flagella hook is unusual. All bacterial species contain a flexible hook between the body of the cell and the flagella filament. Whilst it is widely accepted that some archaeal cells do not possess this hook, swimming studies on such individuals are incredibly limited. The absence of such a ubiquitous structural component could lead to previously undescribed swimming behaviours.

Overall, the results from this full-genome sequencing have highlighted three samples of interest for the motility studies in the remainder of this thesis. *H. hispanica* B and F, and *Hx. volcanii* have different physiological characteristics which may contribute to unique motility behaviours. *H. hispanica* and *Hx. volcanii* are members of different genus' belonging to the family *Halobacteriaceae*. Their relatively close lineage, but largely different habitats makes them an interesting pair of organisms for comparison. The variations in natural environments, coupled with genetic differences in the motility appendage structure may have interesting impacts on the motility behaviours of these organisms.

Chapter 3

Microscopy

3.1 Introduction

The human eye can only visualize objects to approximately 0.5mm in diameter. In order to accurately study single celled organisms on the micrometer scale, samples must be magnified extensively through the employment of optical microscopes. The first optical microscopes were invented by the Dutch microscopist Antonie Van Leeuwenhoek (1635-1723), who created over 500 of his own simple single lens microscopes [87]. His microscopes consisted of a single, biconvex magnifying glass which was ground, mounted between two small apertures and secured in a metal holder [88]. His wide-ranging observations with this invention were the first to detail the shape and structure of a number of biological organisms (Bacteria, fungi, insects, plants), biological components (blood, feathers, scales, spermatozoa, hair) and chemical components (minerals, metals, gunpowder) [89]. Despite his diverse scientific interest, Leeuwenhoek's largest contributions were arguably his in-depth descriptions of "Animalcules", microscopic organisms observed in water droplets from various sources. It has widely been agreed that these early descriptions constitute the first discovery of bacteria [89]. These detailed characterizations sparked a wave of interest in the microbial world which is still evident today through the rapid developments of improved microscopes attempting to visualize smaller phenomenon, in more precise detail than ever before.

3.2 Brightfield Microscopy

Brightfield microscopy is the most fundamental microscopy technique still in use today. The basic brightfield set-up has been modified extensively from Leeuwenhoek's early designs, but the concept remains largely the same. Modern 'infinity

corrected' microscopes consist of two lenses; an objective lens which generates a magnified image of the sample at an infinite distance, and a tube lens which focuses the image on to the eyepiece of the microscope (figure 3.1). These two lenses, mounted between a sample and an eyepiece, form the integral components of a basic light microscope.

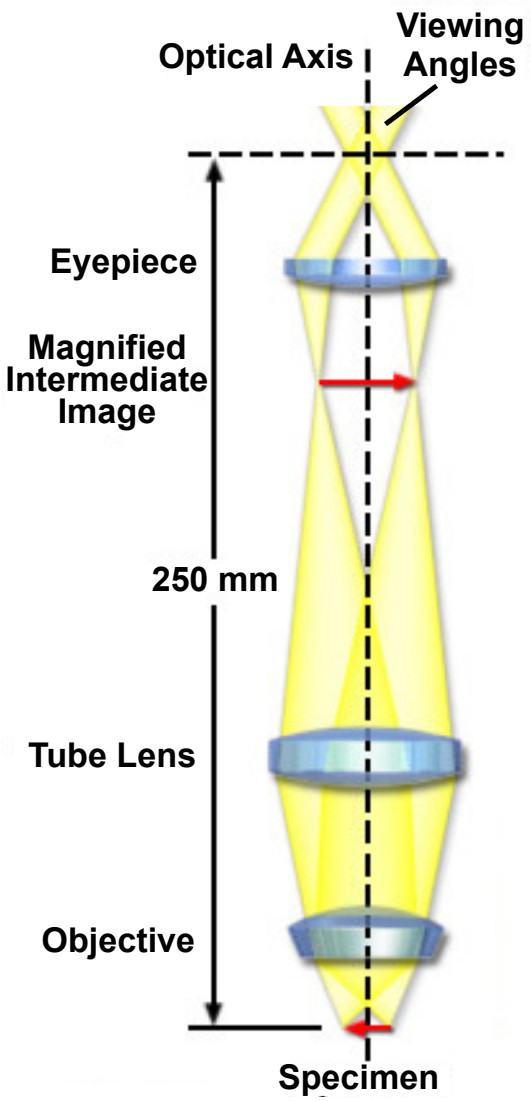

FIGURE 3.1. Schematic of the optical pathway for a basic brightfield microscope, yellow shading highlights the refraction of light through the three core lenses in a standard optical microscope [90].

Most modern microscopes have been adapted for an assortment of imaging techniques, yet still contain these essential optical components at their core. In an upright configured microscope an incandescent light source, situated below the study sample, directs white light through the sample, where it is collected and magnified by the objective lens. This lens generates a magnified image of

the sample at an infinite distance away. The tube lens then refracts the light (containing the magnified image) and focuses it at an intermediate focal plane (figure 3.1). The distance between the tube lens and the intermediate focal plane is known as the focal length (f). The optimal distance between the objective lens and the tube lens is approximately 200-250 mm to improve clarity and reduce aberrations. The image can then be viewed through the eyepiece, which often adds an additional $\times 10$ magnification to the focused image. Typically, the focused image is projected onto a beam splitter prior to the eyepiece, allowing for the use of both the eyepiece and a camera to visualise the sample.

The resolution of a microscope is generally defined as the shortest distance between two points within a specimen that can accurately be distinguished as separate entities [91]. An objective's resolution capabilities are determined by the numerical aperture of the lens and the wavelength of light used for imaging [91]. As a general rule, the higher the numerical aperture and the shorter the wavelength of light, the greater the resolving power of the microscope. The numerical aperture (NA) is a measure of a microscope's ability to resolve an image from a fixed distance.

$$NA = n * \sin(\mu) \quad \text{or} \quad n * \sin(\alpha) \tag{3.1}$$

Where n is the refractive index of the medium between the objective and the sample (usually air (n = 1, water n = 1.33 or oil n = 1.5), α or μ denote one-half of the angle of light from the lens to the sample (angular aperture), determined by the focal length.

In a standard upright microscope (as previously described) focusing of a sample is achieved through movement of the sample stage position. The stage, which houses the sample under investigation, translates both laterally (in the X, Y directions) and vertically (in the Z direction), focusing the sample occurs by altering its proximity to the objective lens in the vertical axis. In comparison, many modern microscopes are designed with the optical axis reversed (inverted microscopes). The inverted design works exactly the same as the the upright design, but rotated 180° with the illumination source housed above the specimen rather than below. Consequently, focusing is achieved by the translation of the objective lens, rather than the sample itself, allowing for the use of thicker samples which are imaged from below. The main advantage of this set-up over upright designs is the improved access to the condenser lens, where additional optical

components (discussed later in this chapter) can be added to improve contrast or modify the light source. An in-depth light microscopy review can be found at [92].

3.2.1 Köhler Illumination

Köhler illumination is the primary technique used in modern optical microscopy to ensure even sample illumination. This fundamental technique was first introduced in 1893 by August Köhler, as a method of improving the resolution of bright-field microscopy [90]. Prior to this, critical illumination was predominately used in light microscopy, with the significant disadvantage that the light source (usually a tungsten-halogen lamp) was visible in the focal plane (image of the specimen under observation).

Köhler illumination involves two sets of conjugate planes within the microscope. Conjugate planes are the inverse of one another, i.e. when one is in focus, the other is out of focus within the optical axis. These planes can be referred to as the 'field' plane, responsible for image formation and the 'aperture' plane, involved in the illumination of the sample (figure 3.2). The field plane consists of a light source transmitting light through the field stop diaphragm via the collector lens. The field stop diaphragm can restrict the diameter of the beam of light, therefore can be used to control the area of sample imaged. The diameter of the aperture in the field diaphragm equals that of the region of sample illumination [93]. From the field diaphragm, the light passes through the condenser lens where it is focused directly on the sample. The light rays containing the image of the sample pass through the objective lens, where the image is focused at the intermediate image plane, before passing through the eyepiece to be focused on the fovea of the retina in the eye. For optimum specimen clarity, the field stop diaphragm, sample and retina (or camera) must be conjugate (figure 3.2 left). When considering the aperture plane, the reverse is true. For uniform illumination of the sample, the bulb filament, back focal plane of the condenser and the rear focal plane of the objective must also be in conjugate. The illumination rays must be in focus at the front focal plane of the objective lens (the position of the condenser diaphragm), the rear focal plane of the objective lens, and the iris which acts as the diaphragm of the eye (figure 3.2 right). The condenser diaphragm aperture controls the angle of light reaching the sample. The combination of the numerical aperture of the objective lens and the position of the condenser diaphragm determine the realized numerical aperture of the microscope as a whole [90].

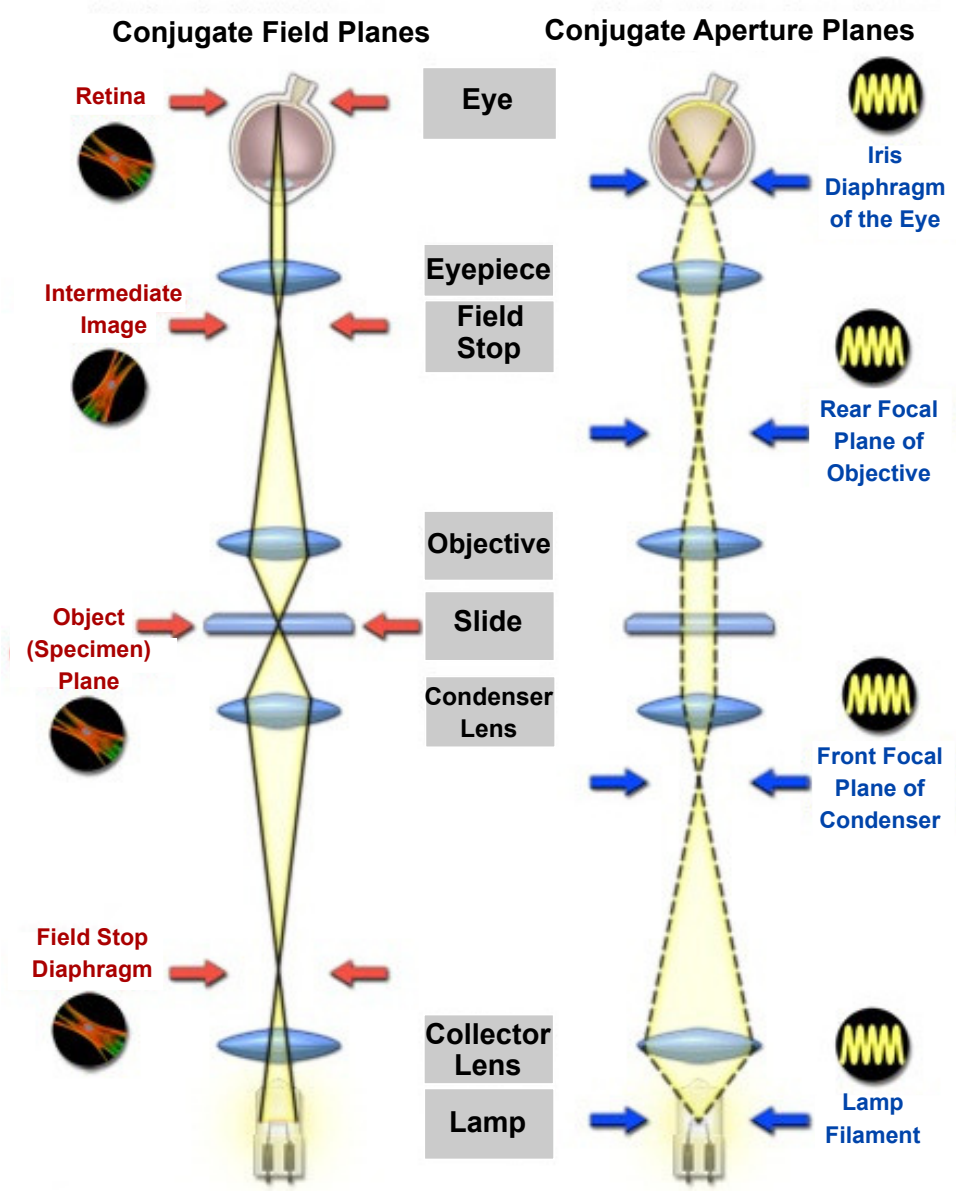

FIGURE 3.2. Schematic of the optical pathway showing the two conjugate planes required for Köhler illumination [90].

Brightfield microscopy generates contrast through changes in light absorption, colour or refractive index. However, most microscopic biological specimens are transparent or translucent/pale in colour, consequently they absorb very little light, creating very little contrast. Due to this low contrast, biological samples can often be difficult to discern, and the fine details can be indistinguishable when using brightfield alone, even with accurate Köhler configuration.

3.2.2 Improving Contrast

The human eye visualizes local intensity fluctuations in the light passing through or around any object. The difference in light intensity between a specimen and the adjacent features or general background in an image is referred to as the contrast. Inherently low contrast specimens (such as cells) produce insufficient variations in the intensity of light compared with the background, rendering the samples almost invisible using brightfield techniques alone [91]. One of the ways in which contrast can be improved is to visualise the phase information within a sample. The phase of a light wave is altered by variations in the thickness or refractive index of a sample. As light passes though a different medium to the surrounding atmosphere, the wave either speeds up or slows down, consequently altering the phase of the original waveform [90]. The unaided human eye is unable to visualise these changes in phase. Objects which create changes in phase without changes in amplitude are known as 'phase objects'. The Dutch physicist Fritz Zernike invented phase-contrast microscopy in 1934 [94] to convert variations in phase to variations in amplitude, enabling detailed observations of these phase objects.

Phase contrast microscopy consists of a beam of light divided into two components; the 'direct' and 'diffracted' waves. The 'direct' waveform passes undeviated around the sample and so has a spatial frequency of zero (zeroth order). This zeroth order wave creates uniform illumination in the eyepiece of the microscope (as in standard bright-field). In comparison, the diffracted wave passes through the sample, slowing down by approximately 1/4 wavelength (or $\pi/2$) [95]. Once diffracted by the sample, these waves also take on higher order spatial frequencies which correspond to the details within the specimen. However if the two light waves were to recombine 1/4 wavelength out of phase (as in standard brightfield) the difference in phase would be very small, and thus the resulting image would be of low contrast. Zernike's key idea was to reduce the delay in the direct light by 1/4 wavelength to gain an optimum difference in phase between the direct and deviated light of 1/2 wavelength for a 'phase object' specimen [96]. When the direct and diffracted waves recombine with a phase difference of approximately 1/2 a wavelength they interfere destructively (figure 3.3) (just as they do for an amplitude specimen), creating a dark image of the specimen on a bright background [92].

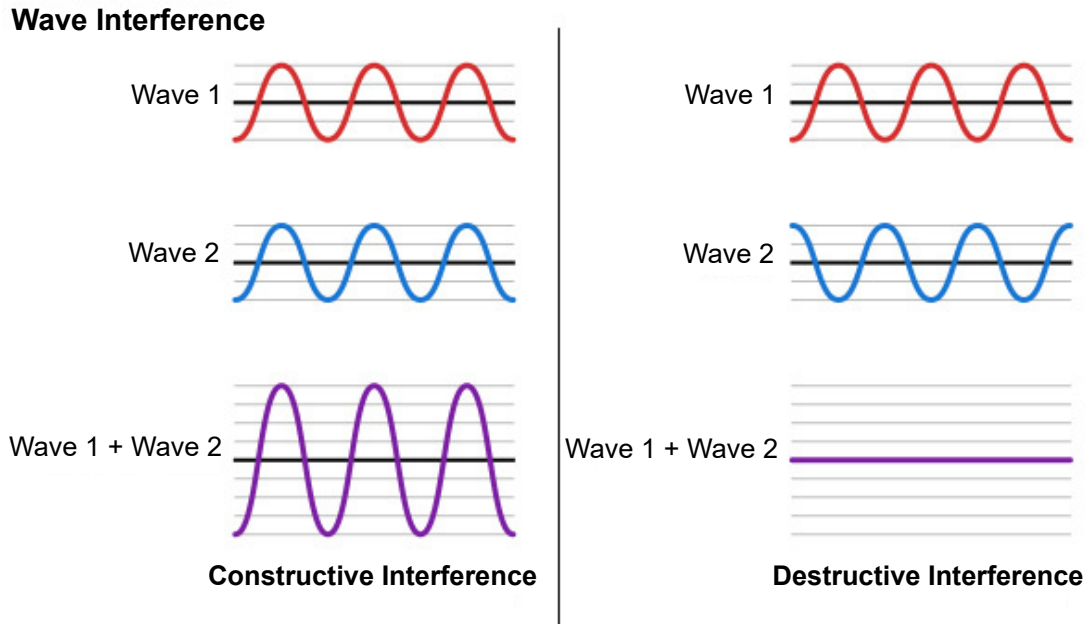

FIGURE 3.3. Simplified diagram of wave interference. *Left*: Waves 1+2 are 'in phase' and so interfere constructively producing a resultant wave of increased amplitude. *Right*: Waves 1+2 are 'out of phase', producing destructive interference and resulting in a reduction in the amplitude [97].

Initially, a spatial filter was used to induce the necessary $\pi/2$ phase shift in the direct wave. The filter created the $\pi/2$ phase advance in the zeroth order (direct) wave, but not in the diffracted wave [95]. However, this phase configuration had the significant disadvantage that when the diffracted light interfered with the direct light the resulting image was spread out in one direction, perpendicular the image, creating bright halos (an artefact caused by this technique). This was later rectified by replacing the strip filter with an annular slit which allow the halo to spread out in all directions, reducing its intensity and resultant effect on the image of the sample [94]. Zernike also realised that for thin phase objects only small changes in the phase of the diffracted light occurred, producing poor contrast final images. In order to improve this an amplitude absorbing metallic layer was added to the phase annulus to reduce the amplitude to one half of that of the direct light [94]. The reconstructed waveforms from the sample region would then be amplitude modulated allowing the image to become visible [95].

In modern phase contrast microscopes, the condenser aperture diaphragm is replaced with a phase annulus (figure 3.4 (*right*)) (the size of which can be varied depending on the numerical aperture of the microscope objective and condenser).

The annulus is placed directly below the condenser lens, conjugate to the rear focal plane of the objective [96]. This phase annulus is a solid, opaque disk with a narrow ring-shaped aperture which creates a hollow cone of light to illuminate the sample (figure 3.4 (*left*)) [90]. This bright cone of light has zeroth order and arrives at the Fourier plane of the objective lens as a bright ring, having passed, undeviated, around the sample. However, the condenser annulus also permits light around the periphery; these planar light waves are much fainter than the direct cone-shaped light waves. This direct light is diffracted by the sample, taking on a $\pi/2$ phase retardation [91]. To create the further $\pi/2$ phase shift required for optimum contrast, a phase plate is positioned at the rear focal plane of the objective. The phase plate is a disk-like structure containing a narrow ring that is optically thinner than the surrounding material (figure 3.4 (*right*)). The ring position is conjugate to the phase annulus, creating a phase advance in the direct zeroth order light, but not the diffracted light. This phase advance in the direct light combined with the phase retardation in the diffracted light creates the necessary difference in phase required for optimal imaging [96].

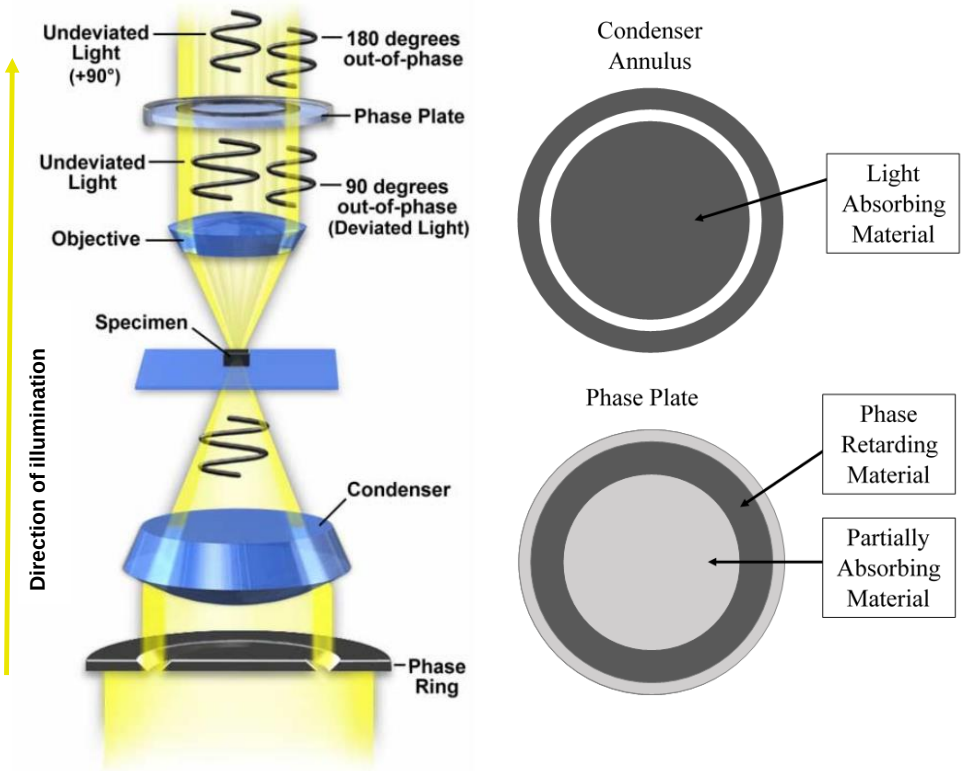

FIGURE 3.4. *Left*: Optical pathway required for phase contrast microscopy. *Right*: Representation of the phase annulus and phase plate used to equip a standard brightfield set-up for phase contrast [92].

Although phase contrast significantly enhances the visibility of transparent (phase) specimens, there are some limitations to this technique. Firstly, phase images are usually surrounded by bright halos. These halos are optical artefacts which can obscure the structural details around the edges of objects within a sample [96]. Furthermore, phase contrast only works well with relatively thin study samples, as an increased thickness can cause the phase shifts to occur above or below the plane in focus, causing blurred or distorted images. Also, the phase annuli reduce the working numerical aperture of the microscope, decreasing the maximum resolution capable by the system.

3.3 Dark Field

Dark field microscopy is another tool used for improving the contrast of 'phase objects', and works in a very similar manner to phase contrast. Light passes through a phase annulus and is divided into two components; 'direct' and 'diffracted'. The direct light passes through the condenser lens and illuminates the sample (as in phase contrast), but is removed (blocked out) before the image is formed at the rear focal plane of the objective lens (Figure 3.5). Fainter oblique rays approach the sample from all azimuths and are either reflected or refracted by the specimen under observation [96]. If no sample were present to diffract the oblique rays, they would cross and miss entering the objective lens entirely, as the numerical aperture of the condenser lens is greater than that of the objective. This would result in a completely black image in the eyepiece of the microscope [91].

Transparent specimens (phase objects) which have smooth surfaces refract or reflect the oblique light, producing small angular changes in its direction, enabling it to enter the objective and produce a light image of the specimen on the otherwise dark background. Variations in the refractive index of a sample produce variations in the angle of refracted or reflected light. Consequently, when the diffracted light interferes at the rear focal plane of the objective lens, an image of the specimen is formed exclusively from these oblique rays containing purely higher order spatial frequencies [92]. The images produced typically shine brightly on a black background.

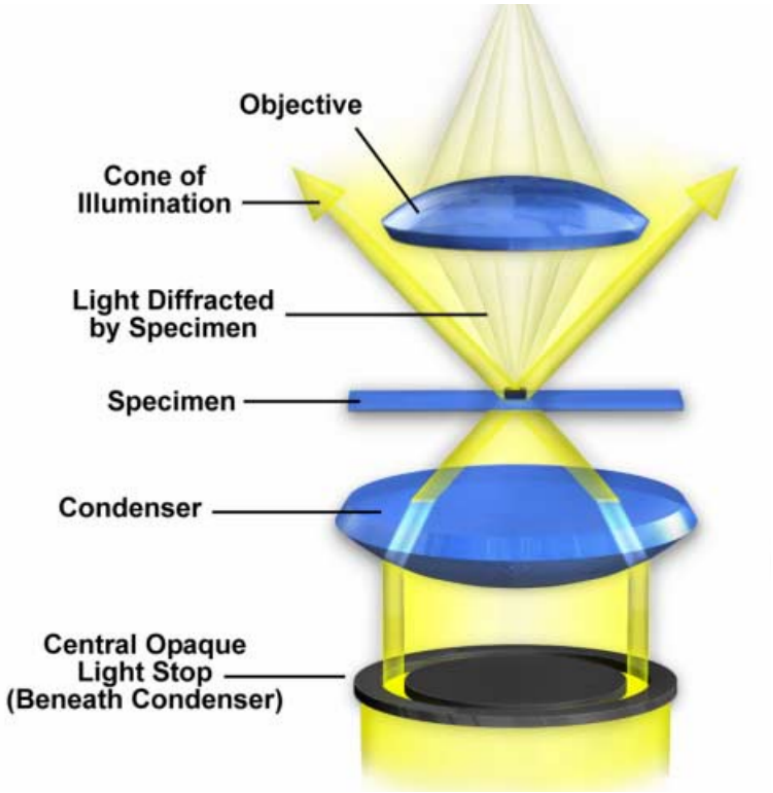

FIGURE 3.5. Schematic of the optical pathway required for dark field microscopy [92].

Dark field microscopy has the same resolution as brightfield, but the optical characteristics are considerably different, therefore the resulting image may not be an accurate geometrical reproduction of the original specimen [91]. Furthermore, if improperly prepared, dust particles and foreign objects within a sample can reflect large amounts of light which may obscure the sample under investigation. However, many specimen details/ discontinuities can often be observed which may be invisible using other brightfield techniques; particularly sample edges and boundaries where the differences in refractive index are greatest [91]. Due to the transparent nature of biological samples, dark field microscopy has been used to visualise a range of dynamic biological objects on the 100-10 nm length scales including; bacterial flagella [98–100], micro-tubules [101], and various aquatic micro-organisms [96], which are irresolvable using brightfield techniques. However, resolving features at this scale requires very high light intensities which could create irreversible damage the specimens under observation.

3.3.1 Dark Field Spectroscopy

Dark field spectroscopy is a high-throughput dark field technique which uses local, time-dependant intensity fluctuations within a sample to evaluate dynamic behaviours across the sample as a whole. Whilst variations of this technique have been employed for the visualisation of macro-organisms (using telescopes) [102], its use within the micro scale is limited [103, 104]. This approach uses a standard dark field optical microscopy set-up to generate high frame-rate video recordings of a dynamic system, which can be automatically analysed 'offline' using purpose-built software.

Dark-field spectroscopy can be used to quantify the body-rotation rates of free-swimming cells [103, 104]. Swimming microorganisms are typically ellipsoidal or asymmetrical in shape and due to their random motion within a 3D medium, their bodies rarely lie parallel with the focal plane. Consequently, as the cell body rotates its angle in relation to the focal plane varies; the further the cell body axis is from alignment with the focal plane, the brighter it appears (figure 3.6 & 3.7). This body rotation is periodic, unlike random diffusive motion, and so it is relatively easy to detect alongside other particle noise.

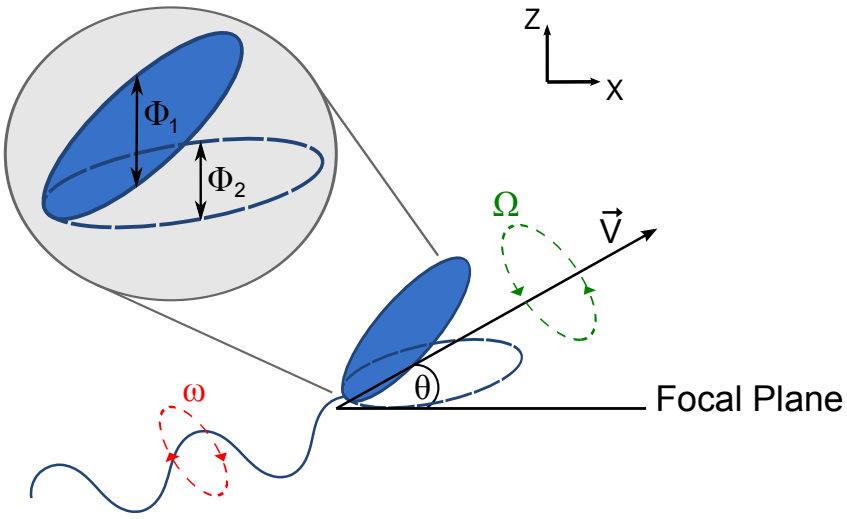

FIGURE 3.6. Simplified representation of a swimming cell (ω and Ω represent flagella and body rotations respectively). The angle θ between cell body's major axis and the focal plane changes as a result of the body Ω rotation around the swimming direction. The greater the angle θ, at any given time, the greater the perceived optical thickness ϕ and thus brighter the cell appears.

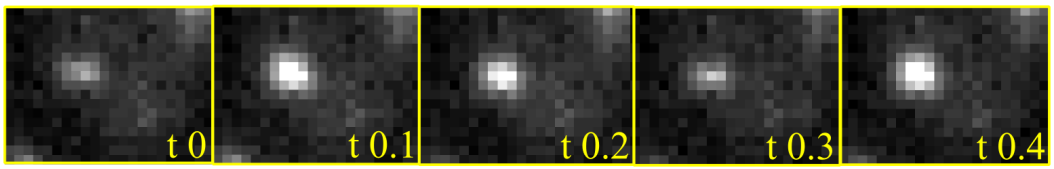

FIGURE 3.7. Dark field spectroscopy time-lapse of a single cell. Cell pixel intensity varies from dark to bright and back, as cell body rotates at a rate of approximately 2Hz (time (t) displayed in seconds).

The custom LabVIEW software [104] converts the raw image data (figure 3.8) in each frame of a low magnification, dark field video into numerical integers (8-bit grey-scale) corresponding to the intensity of each pixel (0-255). Each frame is divided into tiles of a user defined size (typically 5×5 pixels for microorganisms) to adequately capture the phenomenon of interest. The pixel intensities within each tile (i) are summed for each frame within the video. This enables the extraction of values for intensity (I) as a function of time (t) for each tile. The power spectrum (P) for each tile is then calculated using a Fourier Transform (FT) (equation 3.2), before averaging over all the tiles within the video.

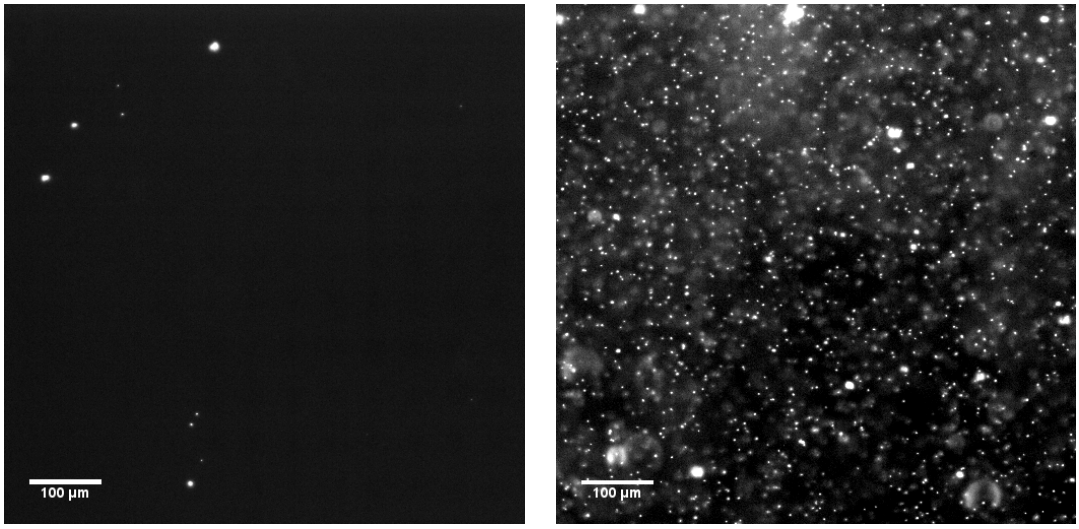

Figure 3.8: Dark field Spectroscopy single frame of raw data (512×512 pixels (1 pixel = 0.711 μm)). *Left*: Modified growth media (control) *Right*: Media containing exponential phase archaea cells. Microorganisms appear as smaller bright spots on a dark background. Dirt and foreign particles appear as large bright spots, which are automatically filtered out during the analysis, as they typically remain static, failing to generate any intensity fluctuations.

$$PSD = \sum_i P_i(f) = \sum |\, FT[I_i(t)]\,|^2 \tag{3.2}$$

The advantage of creating a power spectrum (P), is the removal of the phase component of the data. The intensity oscillations created by different cells within the sample will each produce unique frequency and/or phase profiles. Producing a signal independent of phase allows averaging over the hundreds or thousands of tiles within the sample, without destructive interference. This increases the signal to noise ratio producing more distinct peaks within the final (averaged) power spectrum (PSD) (figure 3.9 (red line)).

Unfortunately, this technique is subject to both Brownian and camera noise. The mean squared displacement for a particle undergoing Brownian motion is known to scale linearly with time [105] (section 1.2.3), therefore the power spectrum for a particle undergoing Brownian motion scales as f^{-2} (figure 3.9 (green line)). Consequently, the Brownian noise component can be easily removed by multiplying the power spectrum by the frequency squared f^2. Additional noise generated by the camera (figure 3.9 (blue line)) is typically low intensity and frequency independent (white noise), therefore does not affect the power spectral density peaks expressed by the cells.

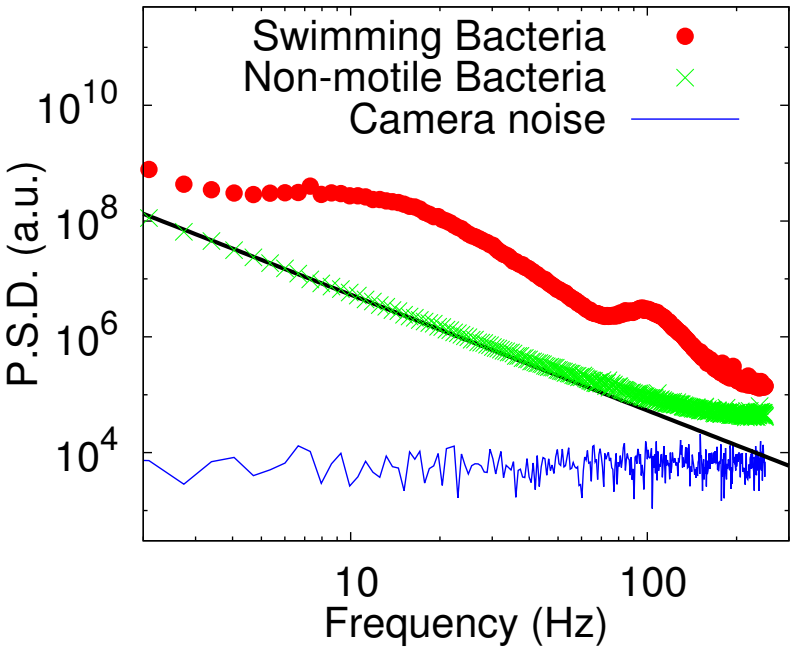

FIGURE 3.9. Dark field spectroscopy signal contributions from; swimming bacteria, Brownian motion and camera noise. Figure taken from [104]

Whilst it is impossible to identify the exact swimming speed of a cell purely from the body rotation, it can be used as a measure of motility, as faster rotation rates would indicate faster velocities when compared with conspecifics. Furthermore, although it is possible to detect flagella filaments using dark field microscopy [98–100], due to their small structure and subsequent weak scattering the ability to detect a signal of the rotation rate using dark field spectroscopy is largely subjective.

Overall, dark field spectroscopy is a convenient, non-invasive technique for recording the body rotation rates of large numbers of cells simultaneously. This method requires much less human input than other approaches for studying dynamic systems (e.g. quantum dot labelling and fluorescence), which tend to be limited to single cell observations at a time.

3.4 3D Tracking Microscopy

All of the previously discussed optical techniques are restricted to imaging in two dimensions, directly at the focal plane. Swimming microorganisms are rarely confined to two-dimensional movement. Countless motility experiments have been performed by restricting motion within the z-direction or simply omitting any out-of-plane motions (for example, [106–110]). However, this often fails to provide an unbiased, complete picture of the cell motion.

Whilst confocal and other scanning microscopes are often used to image the three-dimensional structures of biological samples, the scanning process is generally too slow to capture real-time events within dynamic systems. Consequently, a range of optical techniques have been employed to both image in three-dimensions and capture real-time events, some of which have been specifically designed for the purpose of capturing the movement of swimming microorganisms.

In the 1970s Howard Berg created a 3D tracking microscope specifically designed to 'lock onto' and follow a single bacterium in three dimensions [7]. These tracking microscopes enabled a three-dimensional analysis of the swimming behaviours of *E. coli* [111]. However, this technique has the significant disadvantage that it is only capable of tracking a single organism at any given time. Therefore, the microscope is very low throughput, which is time consuming, and can be difficult to draw viable conclusions on the behaviour of the population as a whole.

A variety of population-scale 3D techniques have been developed to overcome this. One example is defocused particle tracking (DPT) which uses the size of halos surrounding out-of-focus fluorescently labelled cells, as a measure of the axial (z) position of a cell [112]. Whilst this is relatively easy to employ on a standard fluorescence microscope, DPT is limited to $< 100\,\mu m$ depth in z with a resolution of approximately $0.5\,\mu m$, and also relies on fluorescently labelling the cells [113], which may alter motility appendages or behaviours, and are subjected to photo-bleaching. This method has also been employed to study near surface swimming using standard dark field microscopy [114]. Whilst DPT can be employed without fluorescence, using both dark-field and phase contrast, this places further limitations on the z-resolution, reducing the resolvable axial distance [115]. The resolvable z-range of this technique can be improved by imaging both above and below the focal plane, and comparing the out-of-focus images to a series of reference images at known axial positions. This adaptation relies more on the patterns of the diffraction rings, rather than just size, offering a z-range more than double that which can be achieved through standard DPT [115].

Furthermore, most modern, high throughput 3D techniques are typically more computationally expensive, as they often take a series of 2D images and reconstruct the 3D environment. Stereoscopic cameras can be used for imaging organisms $> 10\,\mu m$ [116], but for smaller microorganims digital holographic microscopy is increasing in popularity. For an in-depth review of modern tracking techniques see [117].

3.5 Holography

Digital holographic microscopy (DHM) is an optical technique which can be used for high throughput sampling in three dimensions. Three dimensional imaging is achieved through the capability of DHM to record not only the amplitude of the light waves passing through a sample, but also capture the phase information of the wave. By recording the 'whole' waveform (amplitude and phase), the optical field can be reconstructed at any plane in the direction of light propagation, not just at the focal plane, as is the case with standard brightfield microscopy. The essential additional components required for a digital holographic microscope (DHM) consist of; a coherent illumination source, a digitizing camera and a computer with the relevant reconstruction software (see chapter 4). These features can be easily added to most standard inverted laboratory microscopes [118].

Similarly to the phase methods previously discussed, holograms are created through the interference of two waveforms: light scattered by the sample (typically referred to as the object wave) and unscattered light (or the reference wave). When the object and reference waves combine, the interference patterns produced appear as light and dark fringes corresponding to constructive and destructive interference, respectively [95] (figure 3.10). These diffraction rings can be numerically reconstructed to extract a range of useful features from the sample [119]. A single holographic image contains all the information about the 3D structure of the sample under investigation.

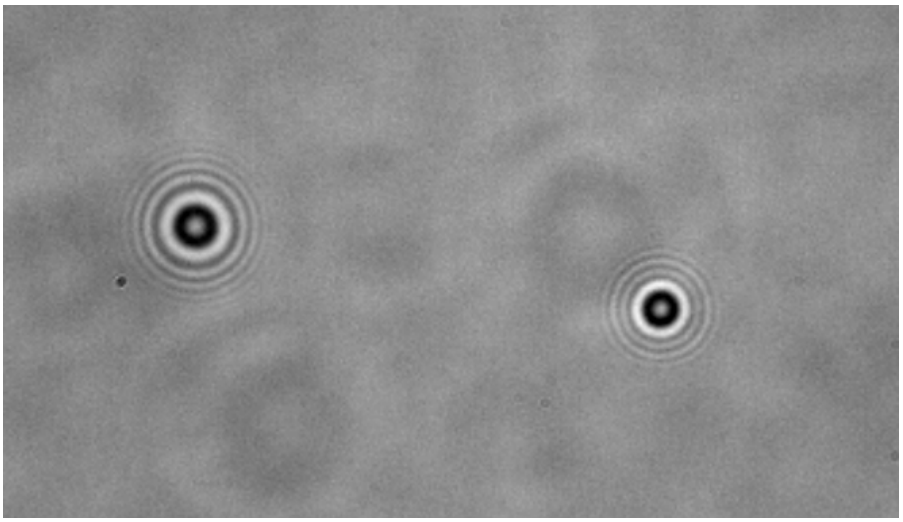

FIGURE 3.10. Holography diffraction rings 1μm colloidal particles, imaged using standard DIHM experimental set-up (discussed in section 3.6.2).

3.5.1 Theory

Holography was first developed in 1948 [120], as a technique to improve the resolution of electron microscopy. However, whilst its potential as a light microscopy technique has been understood for decades, it became much more accessible with the introduction of charge coupled devices (CCDs) and improved computer processing in the late 1990s, gaining the term 'digital' holography [121]. There are various optical set-ups which can be used to generate holographic images. Typically these are either 'off axis' through the superimposition of a reference wave onto the object wave, or 'in-line', where the object wave is in general alignment with the reference wave. Off-axis techniques typically require two distinctly separated beam paths and additional numerical refocusing steps [118]. For the purpose of this thesis, we will only consider the simpler 'in-line' configuration.

Digital in-line holographic microscopy (DIHM) uses a coherent light source, directed at the sample, creating interference patterns which are recorded at high frame rates and reconstructed offline using custom designed code. One of the simplest ways of creating a coherent initial waveform is by passing laser illumination through a pin-hole, before it reaches the object of interest. The emanating light would then be spatially coherent [122] (figure 3.11). This set-up is difficult to integrate on a standard laboratory microscope. Consequently, we achieve coherence through the use of a laser diode coupled to single mode fibre, which effectively acts as a pin hole filtering out higher order waves. By placing the illumination source further from the sample (2-5 cm), we ensure the incident light is 'flat' at the point of interference, so can be considered planar. This set-up enables a maximum imaging depth of approximately 10 mm at low magnification [123], with a maximum resolution of the order of the laser wavelength [122]. However, even LEDs can have a coherence length of around 10μm, so can also be employed for limited imaging depths ($100 - 200\,\mu m$) [123].

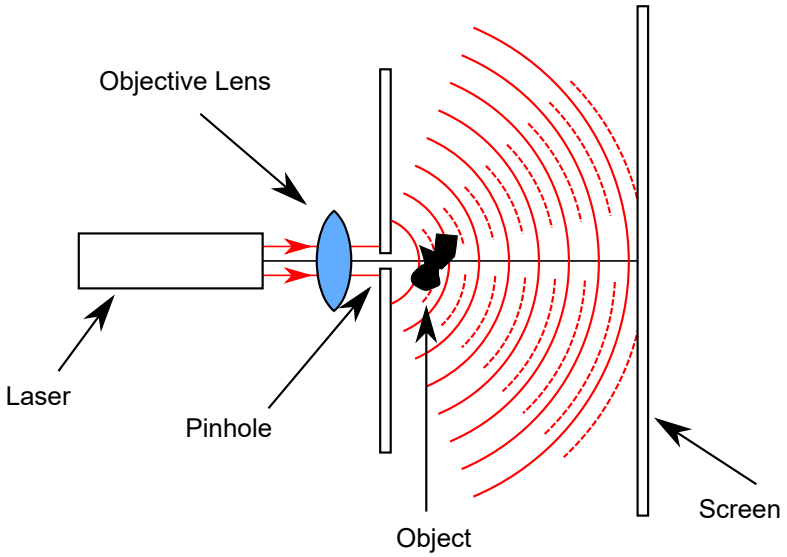

FIGURE 3.11. Pin-hole holography set-up (adapted from [124]). Solid red lines represent the reference wave, dashed red lines represent the object scattered wave.

In holography the incident illumination can be described as a plane wave propagating along the optical (z) axis. This coherent illumination can be approximated to having an equal amplitude across the transverse plane (x, y directions). The coherence intensity I_{coh} profile created through interference with the sample, can be calculated by combining the absolute value of the electric field of the object

E_{obj} and reference E_{ref} waves squared.

$$I_{coh} = | E_{obj} + E_{ref} |^2 \tag{3.3}$$

After scattering by the object, the resulting amplitude is a complex number, but we are only interested in the real (Re) part of the electron profile.

$$I_{coh} = | E_{obj} |^2 + | E_{ref} |^2 + \mathrm{Re} E_{obj} E_{ref} \tag{3.4}$$

The electric field of the scattered wave is much smaller than the reference wave, because we are only considering weakly scattering objects. Consequently the contributions from the object wave can be omitted.

$$I_{coh} = I_{obj} + I_{ref} + \mathrm{Re} E_{obj} E_{ref} \qquad | E_{obj} | << | E_{ref} | \tag{3.5}$$

$$I_{coh} \approx I_{ref} + \mathrm{Re} E_{obj} E_{ref} \tag{3.6}$$

Normalizing the hologram by the intensity distribution of the reference wave gives us:

$$\frac{I_{coh}}{I_{ref}} \approx \mathrm{Re} \frac{E_{obj}}{E_{ref}} + 1 \tag{3.7}$$

When the light scattered by the sample (object wave) and the unscattered light (reference wave) recombine, they create a series of concentric circles (diffraction rings) (figure 3.10). The light and dark rings produced are representative of the different phases of the combined waves. When both waves are in phase, the combined light-wave will have higher amplitude and thus a brighter ring, whereas out of phase waves will produce darker rings (for an in-depth review see [118]). These diffraction rings can be numerically refocused via one of several computer processing operations. Typically refocusing involves fitting the images to known solutions for Maxwell's equations, the most commonly used being the Mie scattering solutions for scattering spheres [125], with similar methods for cylindrical objects also being adopted [126]. These methods can accurately track objects with nm scale precision, but require prior knowledge of the light scattering properties of the objects being imaged and are usually very computationally expensive [127]. We use the model-free Rayleigh-Sommerfeld back-propagation

method of reconstruction [128], which is suitable for a wide range of weakly-scattering objects and less computationally expensive than other methods [127]. The reconstruction process is discussed further in chapter 4.

3.5.2 Applications

Digital holographic microscopy can be used to accurately reconstruct the shape, and/or the position of particles or organisms on the micro scale. Shape characteristics are often defined using quantitative phase holography, whereby the interference patterns are used to determine the optical thickness profile of a transparent object or organism [129]. This can be used for the extraction of a number of morphological (e.g. area, perimeter, axis lengths, eccentricity etc.) and texture-based (e.g. intensity, contrast, smoothness, uniformity etc.) features from a wide range of biological samples [130, 131]. Digital holography in either form has been employed across the single celled spectrum, including; algae [131, 132], spermatozoa [133, 134], protozoa [135], bacteria [132, 136, 137] and dinoflagellates [138]. However, until now, this technique has not been used to explore the motility of archaeal cells.

Portable holographic microscopes which allow for in-situ recordings within difficult to sample regions, have also been developed [124, 139]. These provide the opportunity to explore microorganism behaviours in extreme and remote places such as; glacial pools, underground mines, and potentially, extraterrestrial environments [124, 139].

3.6 Experimental Set-up

A standard experimental set-up was used for all imaging within all experiments for this thesis [140].

3.6.1 Optical Microscope

All imaging was performed on a standard inverted laboratory microscope (Nikon eclipse Ti). Still images and video files were captured using a Mikrotron MC-1362 monochrome CMOS camera. The system was positioned on an optical table (Thorlabs Nexus) to reduce noise contributions from the surrounding environment.

Dark-field recordings were captured using a Nikon dark-field condenser lens (dry, NA 0.95-0.8) or a mismatched phase annulus. A × 10 objective lens (dry, NA

0.30) was used for all dark-field video capture, to maximise the number of cells captured within the imaging area.

3.6.2 Holographic Microscope

The DIHM configuration used within experimentation was installed on an inverted Nikon eclipse Ti microscope (figure 3.12). The microscope was modified for holography by replacing the standard condenser lens with a bespoke 'cage mount' (figure 3.13) optical component, designed to secure the laser fibre used for illumination. The illumination was produced by a fibre-coupled laser diode (λ = 642 nm (red)). This laser fibre was positioned approximately 5 cm directly above the sample, creating a uniform illumination intensity across the imaging plane.

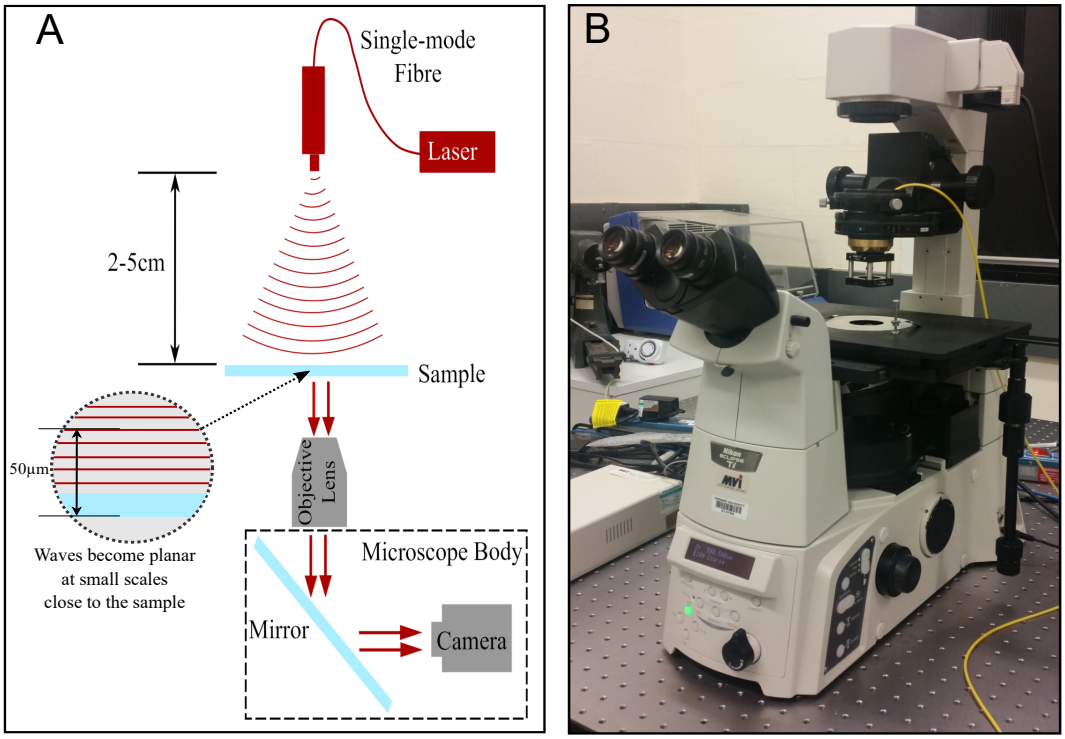

FIGURE 3.12. Image A: schematic drawing depicting the optical set-up used in all holographic experiments (adapted from [140]). Laser illumination becomes planar at micrometer scales within the imaged region of the sample. Image B: photograph of the actual microscope configuration used within experimentation.

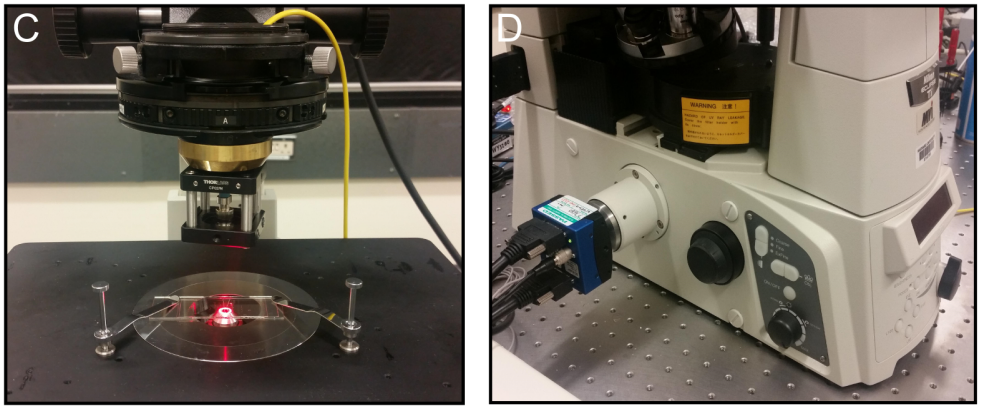

FIGURE 3.13. Image C: is a close-up photograph of the laser position above sample, including the cage mount used to secure the laser fibre. Image D: features a side-view of the microscope, highlighting the side-mounted Mikrotron CMOS camera used for video capture.

The objective lens used for holographic tracking was a 20× (air, NA 0.5). This magnification enabled a large field of view (x, y) whilst maintaining a large enough pixel size to accurately detect the contributions from the weakly-scattering microorganisms. This produced a final pixel size of 1.42 pixels$/\mu m$. For maximum axial (z) imaging, the microscope's focal plane was manually positioned approximately 50 μm below the bottom surface of the sample.

The video footage was captured using a Mikrotron MC-1362 monochrome CMOS camera (figure 3.13). Images were set to a size of 512 × 512 pixels (a subset of the full 1280 × 1024 pixels available on the sensor). A 'global shutter' ensured that all regions of the sensor were exposed simultaneously. The camera was connected to a frame grabber card with 4GB of system RAM reserved for image acquisition. This enabled rapid recording of uncompressed video footage which could be saved and processed 'offline' at a later stage.

Chapter 4

Computational Analysis

4.1 Introduction

Raw videos taken during experimentation were processed 'offline', using LabVIEW software developed in-house. This method was selected as the holography reconstruction is computationally expensive and performing analyses at the rate of capture would require extensive computational power and would reduce the speed at which we we able to perform the imaging.

The videos consisted of a series of 8-bit grey-scale images featuring a collection of diffraction rings (concentric circles varying in intensity) which move around the field of view (figure 4.1). Each of these rings represents a single cell moving within the chamber slide. Once recorded, videos were assessed individually to check for abnormalities (such as extensive drift or camera noise) and a single-frame analysis was undertaken to extract the necessary parameters for whole-video analysis. Once the required parameters were established, video analysis could then be performed in batch, requiring less human input and saving time.

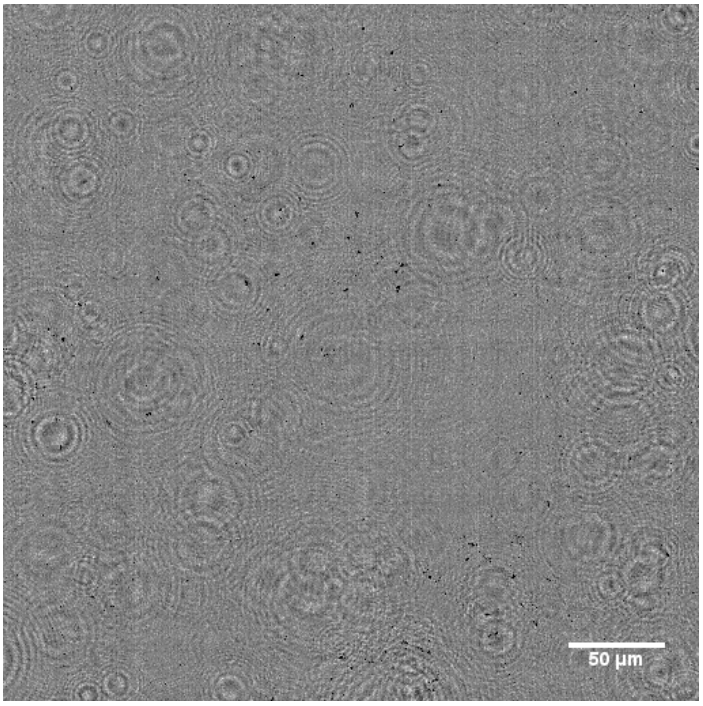

FIGURE 4.1. A single frame of raw holography data. Cells used in this figure are *H. hispanica* (F), using the standard experimental holography set-up. The scale bar represents 50 micrometers.

The video analysis step was used to extract the positional co-ordinates of each cell within each frame of video. Once the co-ordinates had been generated, they were 'stitched' together to form tracks of individual cells. These tracks were then spline-smoothed to increase the signal to noise ratio, and any non-motile cells were removed from the data set. The remaining tracks could then be used to calculate various motility parameters such as; the swimming speed, duration or directionality. To locate any reorientation events a peak-fitting algorithm was applied to the tracks. The reorientation events could then be analysed separately to the straight swimming behaviours.

Simulations of diffusing particles and swimming cells were created to test the reliability of the code, using known parameters. This enabled the rapid generation of synthetic data which could be easily modified for future experiments.

4.2 Holography Analysis Methods

The first step of analysis was to convert every pixel within each video to a single precision number based upon its intensity. This effectively created a large array of numbers for each frame within each video.

Mean and median images were then created from the videos by summing the pixel intensity at each point across every frame and dividing by the number of pixels or extracting the middle pixel value respectively. This was repeated for every pixel within the frame, and the new values were compiled to create a single average image of the video (figure 4.5). The pixel values of each frame within the video were then divided by those of the average image, to amplify changes in pixel intensity between frames by removing the fixed background. Whilst either form of average image would be suitable for this, the median was selected within these experiments, as this would ignore any extreme values (created by dead pixels or noise) which would be included in the calculation of the mean image.

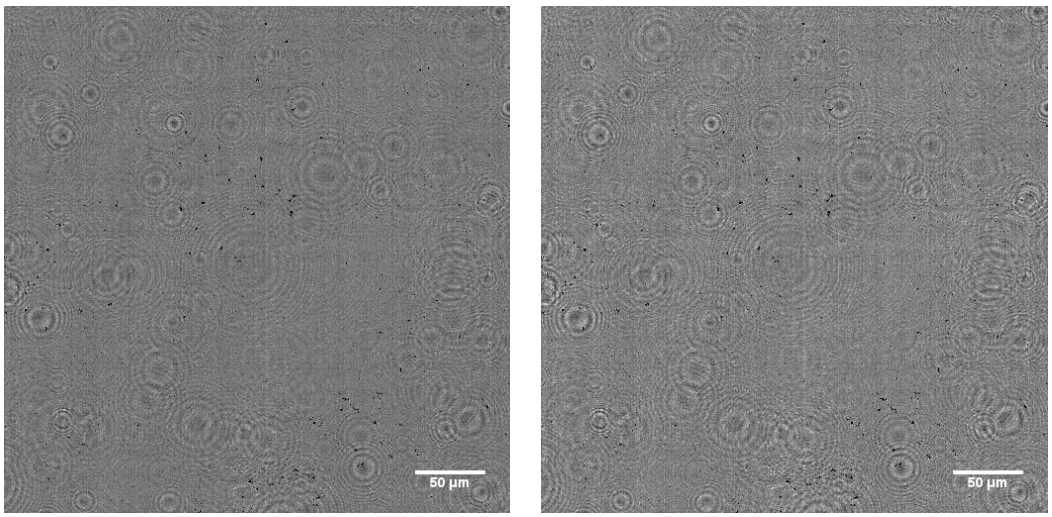

Figure 4.2: *Left*: Mean image $I_{mean}(x, y)$ created from raw holography video. *Right*: Median image $I_{med}(x, y)$ created from raw holography video. Note the high degree of similarity between the two images. Both images were created using the same video as in figure 4.5. Scale bar represents 50 micrometers.

The next step of the analysis is to replace any pixel values of zero within the video with the mean pixel value for that video, to remove any dead pixels or other aberrations which may have previously been included. At this stage, the frame size is also checked. Whilst all videos within these experiments were square (512 × 512 pixels), the software is capable of dealing with asymmetrical images by reflecting the image to make it square for ease of processing.

4.2.1 Locate Cells in 3D Space

The analysis method chosen used the Rayleigh-Sommerfeld back-propagation method of reconstruction (as detailed in [141]). Firstly, a single frame $I(x, y)$ is extracted from the video. To reconstruct images in the z direction, from this frame,

the total number of z images ('slices') required needs to be specified. Next, the space between the 'slices' needs to be defined. Given the 1.422 pixels per μm resolution in the x, y directions of the raw video footage, a step size of 2 μm from the focal plane was chosen for 150 'steps' within the reconstructed image stack.

The Fourier Transform FT of the single frame is then calculated in two dimensions;

$$FT_{2d}[I(x,y)] = \tilde{I}(u,v) \tag{4.1}$$

Conceptually, every pixel within the image is then treated as the source of spherical waves, the superposition of which is calculated at defined z-displacements. This is achieved by a convolution in real space, or (equivalently) a multiplication in Fourier space. This is repeated for every possible z position (as defined by the user). The propagator (spherical wave) h is multiplied by the image in Fourier Space.

$$\tilde{I}(u,v,z) = \tilde{I}(u,v,z) \cdot h(u,v,z) \tag{4.2}$$

The denotion $\cdot$ refers to an element-wise multiplication, whereby every pixel value within the 2d image array is individually multiplied with the corresponding value in the propagator array. At this point a spatial bandpass filter was applied in Fourier space, allowing objects between 1 and 30 pixels to pass through. The bandpass filter is shifted to the edges to accommodate the Fourier transform [128]. The inverse Fourier Transform then converts the pixel array back into real space.

$$FT_{2d}^{-1}\tilde{I}(u,v,z) = I(x,y,z) \tag{4.3}$$

This process produces an image stack of the interference patterns at each z position (figure 4.3). In standard light microscopy, when an object is slightly above the focal plane, it appears dark in colour. If it drops below the focal plane, it becomes light in colour. These transitions from dark to light also apply in holographic images. The z position at which the centre of a diffraction ring changes from dark to light in the refocused stack indicates when it is in focus and thus the actual z position of the cell (figure 4.4). This is applicable for imaging on either side of the focal plane as is shown in figure 4.4.

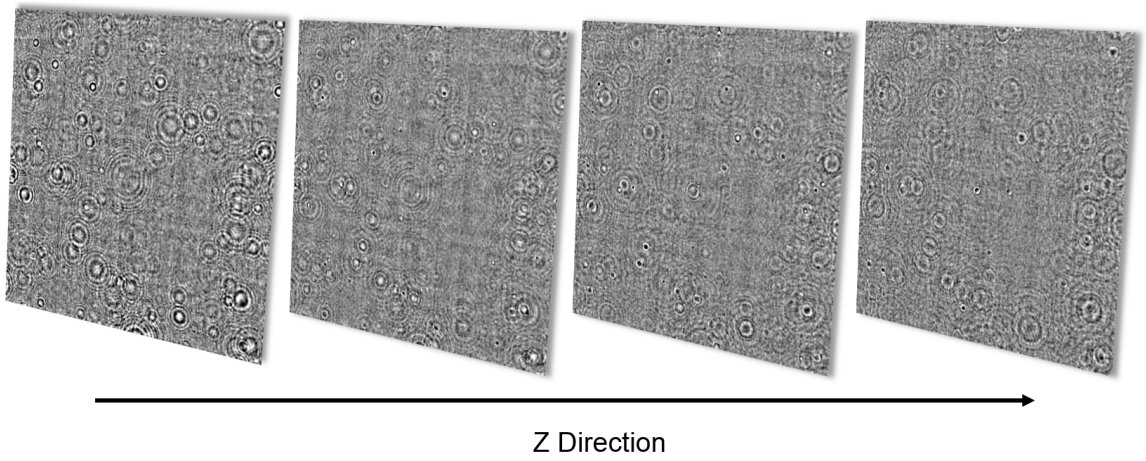

FIGURE 4.3. Slices from a reconstructed image stack ($I_{im}(x,y,z)$). Note the changes in contrast of diffraction rings with changing z position. The z direction refers to the axial position within the sample. The four images displayed are representative slices of a stack of 250 images with a changing z position, with the left image being taken at the focal plane and subsequent images moving further away.

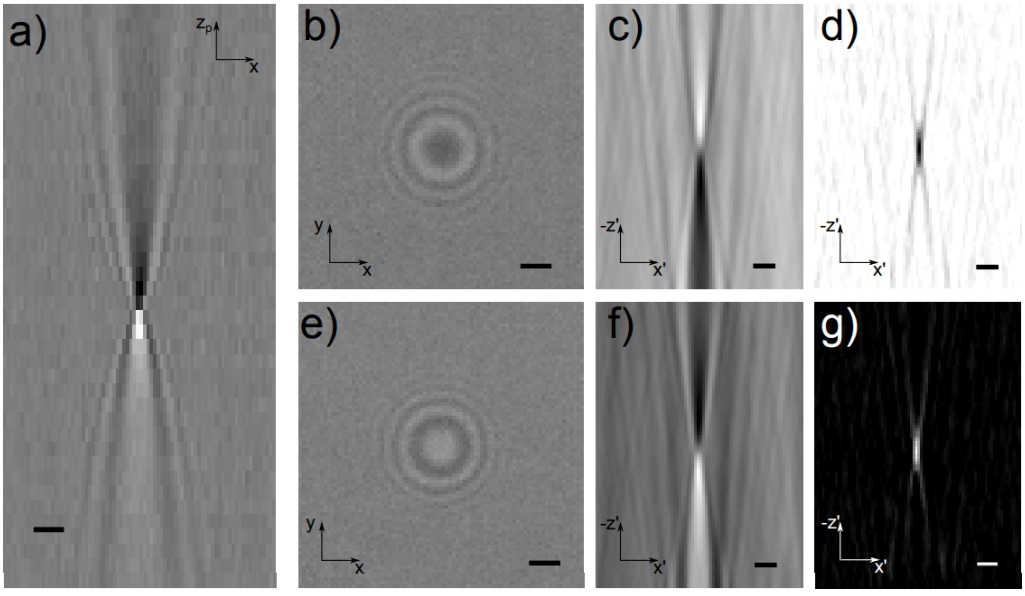

FIGURE 4.4. (a) Vertical slice through the sample, note the contrast inversion from dark to light above and below the focal plane respectively. (b) Diffraction rings produced by a single particle $\approx 9\,\mu$m above the focal plane. (c) A vertical slice through the reconstructed image stack for the particle in (b). (e) and (f) are the the same as (c) and (b), but taken from $\approx 9\,\mu$m below the focal plane. (d) and (g) are the gradient stacks for (b) and (e) respectively. Scale bars represent $2\,\mu$m in all images. Figure taken from [141]

4.2.2 Sobel filter

To produce the intensity gradient stack, the image stack is convolved with a Sobel filter (equation 4.4) [119]. The Sobel filter picks out intensity gradients in the direction of the optical axis (z). Areas with high gradients (in our case, areas with cells) appear as bright on a dark background.

$$I_{grad}(x,y,z;t) = I_{im}(x,y,z;t) \otimes S_z(x,y,z), \tag{4.4}$$

where the Sobel-type gradient operator $S_z(x,y,z)$ is the 3×3×3 array [119] given by:

$$S_z(x,y,0) = \begin{pmatrix} -1 & -2 & -1 \\ -2 & -4 & -2 \\ -1 & -2 & -1 \end{pmatrix}$$
$$S_z(x,y,1) = \begin{pmatrix} 0 & 0 & 0 \\ 0 & 0 & 0 \\ 0 & 0 & 0 \end{pmatrix}$$
$$S_z(x,y,2) = \begin{pmatrix} 1 & 2 & 1 \\ 2 & 4 & 2 \\ 1 & 2 & 1 \end{pmatrix}.$$

This process is computationally less expensive to perform in Fourier space, therefore:

$$I_{grad}(x,y,z;t) = FT_{3d}^{-1}[FT_{3d}[I_{im}(x,y,z)] \cdot FT_{3d}[S_z(x,y,z)]] \tag{4.5}$$

4.2.3 Blobs to Single Pixels

Applying the Sobel filter results in a gradient image stack containing a series of white 'blobs' at the cell locations, on a dark background. These need to be consolidated to a single pixel, to provide a single x, y, and z co-ordinate for each cell within the frame.

Firstly, to accurately determine the x and y positions, the image stack is flattened into a single image (max intensity projection) (figure 4.5 (*left*)). Next, a LabVIEW built in feature ('count objects') locates all the bright objects within

an image. At this point a user defined threshold can be applied to select for the brightest pixels. Any values below the threshold are set to zero, reducing the size of the 'blobs' located (figure 4.5 (*right*)). Once an appropriate threshold has been selected the 'count objects' feature will extract the centre pixel co-ordinate for each object (in many cases the thresholding process will have restricted the object to one pixel anyway).

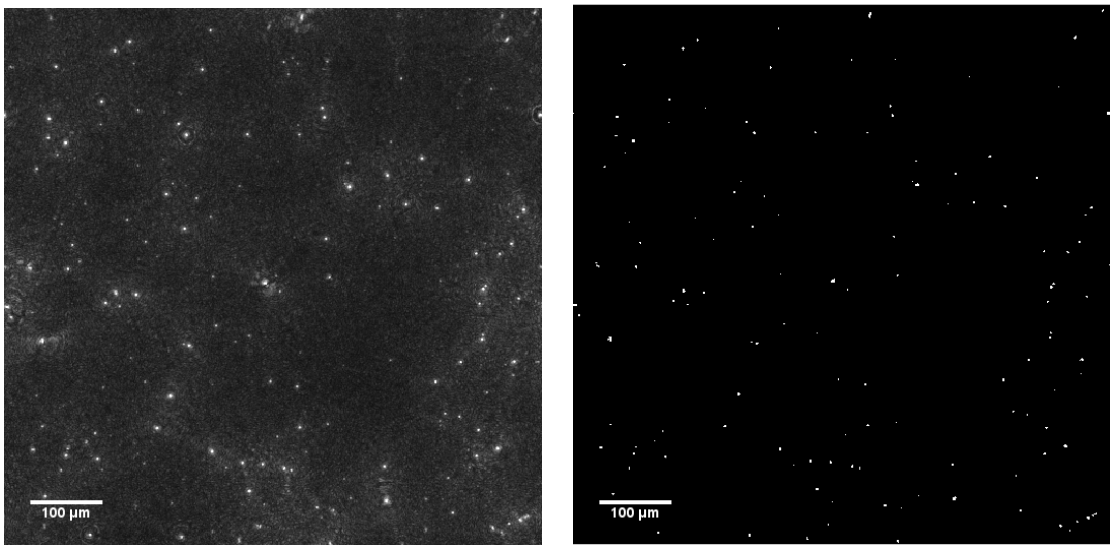

Figure 4.5: *Left*: The maximum intensity projection of the intensity gradient stacks $I_{grad}(x,y,z;t)$; this data can be used either for image registration or for object localization. *Right*: Data after threshold process used to localize objects.

To locate the z co-ordinate a column of pixels is extracted, centred around the previously defined x,y co-ordinate. The column size is user defined, although the default size is a $3\times3\times z_{max}$ sized column. The intensity values for each pixel are summed for each z 'slice', giving a $1 \times 1 \times z_{max}$ array of pixel intensities. A peak search algorithm at the x,y locations, applies local quadratic fits in the z data, to the areas where there is an increase in pixel intensity. The location of the top of the fitted peak is considered the centre of intensity and is therefore used as the z co-ordinate of the cell. This whole process is repeated for every cell within every frame of each video, to give a list of cell co-ordinates within each frame.

4.3 Tracking

This section will cover the process used to build tracks from the single-frame cell location data. Smoothing will be undertaken to remove noise, and cells will be

sorted into 'swimming' and 'diffusing' groups. The process for isolating reorientation events within trajectories will also be detailed.

4.3.1 Stitching Co-ordinates Together To Make Tracks

The main obstacle with any tracking software is linking the position of one object in a particular frame, with the same object in subsequent video frames. From the previous processing steps, we have the 3-dimensional positional co-ordinates for multiple objects identified within each frame of holographic video. To track these objects' over time, each object needs to be 'linked' to a corresponding object within the next frame. To enable this, a search is carried out in the subsequent frame to find objects which fall within a user-defined distance of the original object position. Unlike similar tracking algorithms [142], this software does not simply pick the closest point within the search sphere to become the next in the trajectory. The algorithm looks at the previous video frames (for a user-defined number of frames) and the subsequent cell position selected is linked to the previous points within the trajectory. Therefore, if two points are equally close to an individual cell, the chances of tracking the correct cell swimming direction are much higher. Furthermore, if the cell disappears, or isn't detected for a frame, then the data is interpolated to prevent a break in the track. This is repeated for each cell until there are no points that fall within the 'search sphere' in subsequent frames, and the track is terminated.

Whilst all holographic imaging is undertaken at dilute concentrations, there is always the possibility of colliding or interacting cells. Cells which collide or cross paths are notoriously difficult to accurately track. Furthermore, these interactions can impact the swimming behaviours of the organisms involved. Consequently, when two cells cross at close distances (within a pixel) of one another, the associated tracks are stopped before the interaction, and a new track is initiated immediately after. Whilst this may create a slight bias for shorter tracks, this is preferable to incorrectly tracking the wrong cell after a collision.

At this point in the analysis, very short tracks are separated from the main data-set. This is because it would be difficult to extract any useful data about swimming behaviours from tracks a few pixels in length. Therefore, if the total length of the trajectory is shorter than a user-defined length, the track is disregarded. This length will vary dependant upon the speed of the cells, frame rate of the video recording and the behaviours being investigated.

Overall the holography code has an accuracy of approximately 1 pixel in both the x and y directions, which in the case of this thesis equates to 0.71 μm. Higher levels of accuracy could be achieved using higher magnifications. In the z direction objects can be accurately resolved to a sub-micron level. The limit of resolution can be easily calculated as the wavelength of illumination divided by the numerical aperture squared ($\lambda/2(NA)^2$). The set-up used within this thesis had an accuracy of approximately 360 nm in the z direction. Using shorter wavelengths of light would improve the resolution in the axial direction, with UV lasers potentially offering the greatest accuracy.

The exact values used for the computational analysis settings within experimentation can be found in chapter 6.

4.3.2 Spline Smoothing

In order to remove any remaining noise (camera, pixel or diffusive) the tracks were smoothed using a spline smoothing algorithm created in LabVIEW. The cubic spline smooth is an in-built LabVIEW function which fits a piecewise cubic line to the data and uses a balance parameter (between 0 & 1) to control the smoothness of the fit. A balance parameter of 0 would produce a linear fit, whereas a value of 1 would pass directly through each of the data points. In general terms, the closer p is to 0, the smoother the fitted curve, conversely, the closer p is to 1, the closer the fitted curve is to the actual data points. The cubic spline fit ($x_s(t)$) is found using the function:

$$x_s(t) = p\sum_{i=0}^{n-1} w_i(x_i - f(t_i))^2 + (1-p)\int_{t_0}^{t_{n-1}} \lambda(t)(f''(t))^2 dt \tag{4.6}$$

Whereby p is the balance parameter and x_i are the individual elements of the position x at various time points t_i respectively. w is the weight assigned to each element; which in this case this can be ignored as all of the points are equally weighted. $f''(t)$ is the second-order derivative of the cubic spline function; $f(t)$, and $\lambda(t)$ is the piecewise constant function (equation 4.7). The piecewise function controls the smoothness for each interval between two contiguous data points, therefore:

$$\lambda(t) = \lambda_i \leq t < t_{i+1} \qquad \text{for} \quad i = 0, 1, 2....n_{-1} \tag{4.7}$$

Figure 4.6 shows a spline fit to the raw data of a single track in each of the x, y and z directions. The raw data points show considerable levels of random noise at the small-scale, created by Brownian motion and a cell 'wobble' generated by the off-axis positioning of the archaellum. Consequently, the balance parameter is set relatively low (0.3) to create a smooth curve, highlighting only the major features of the data. The fit is applied separately to each of the x, y and z directions.

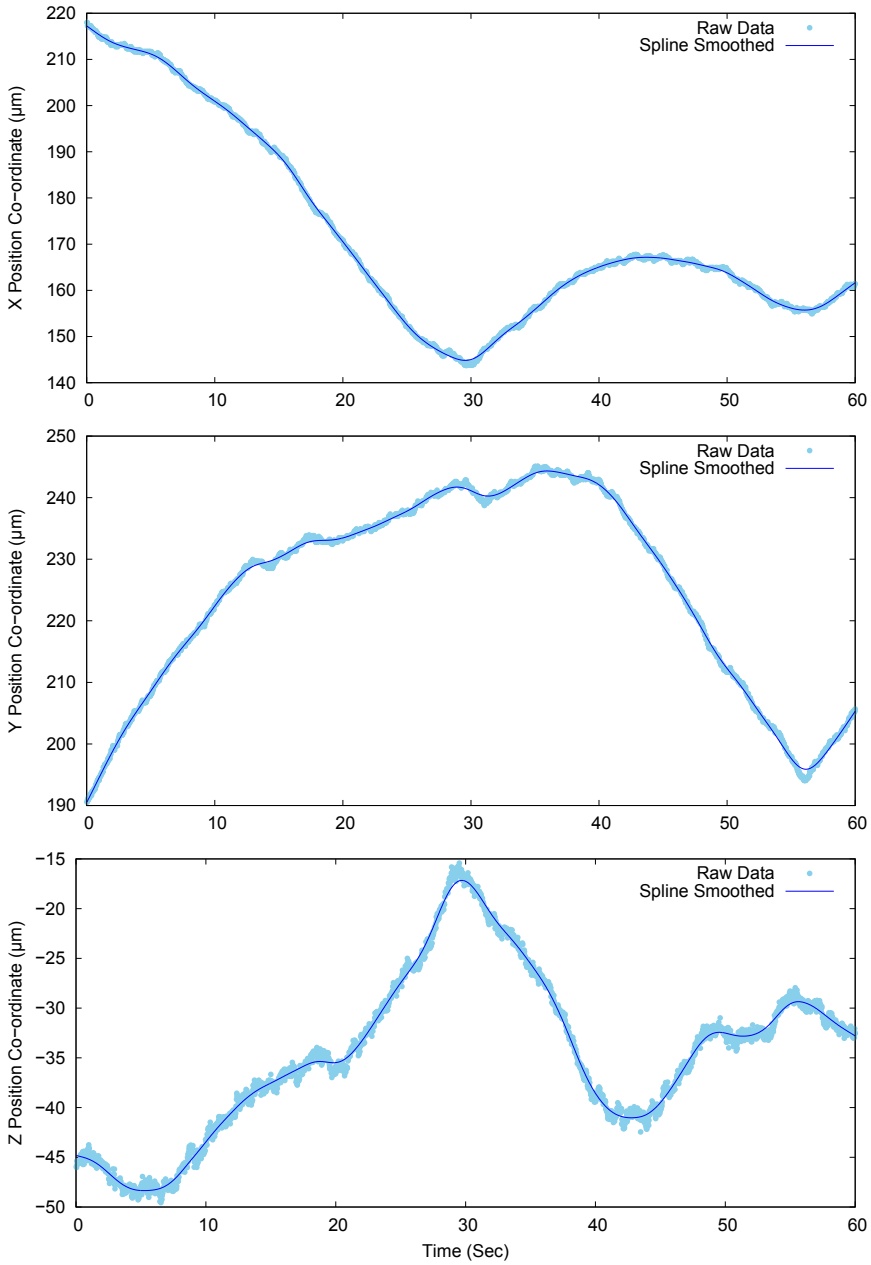

FIGURE 4.6. Example trajectory showing the raw data points and spline smoothed cubic fit in each of the x, y and z directions. The balance parameter (p) used was 0.3 to create a smooth curve. Weighting and smoothness values were both set to the default value (1).

4.3.3 Separating Swimmers and Diffusers

To separate the swimming cells from the non-motile cells undergoing purely Brownian diffusion, the mean squared displacement of each trajectory was calculated (equation 4.8) (also see section 1.2.3). The displacement was extracted for every size of time interval (τ) in each of the x, y and z directions independently and plotted on a log scale graph (figure 4.7).

$$MSD_{1D} = [(\Delta x - \Delta\tau)^2] = \frac{1}{n}[(x_{t1}(\tau)) + (x_{t2}(\tau)) + (x_{t3}(\tau)).....] = \frac{1}{n}\sum_{t=1}^{n} x_t^2(\Delta\tau) \qquad (4.8)$$

On a log scaled graph, the ideal gradient for a purely swimming cell is $log\,(2)$ whereas for a purely diffusive cell it is $log\,(1)$. A gradient threshold value of $log\,(1.4)$ was selected for experiments, as swimming microorganisms are subjected to the effects of Brownian motion, thus display swimming trajectories which contain a diffusive component. Swimming cells must have a steeper slope than the threshold, in all three directions (x, y, z).

A horizontal threshold was also set, whereby the last value of the MSD in each direction x, y and z must fall above the threshold to be considered a swimmer. Any track below the value is considered a diffuser, (figure 4.7). The thresholds values selected are slightly smaller than expected, as both threshold criterion must be met for a cell to be considered a swimmer.

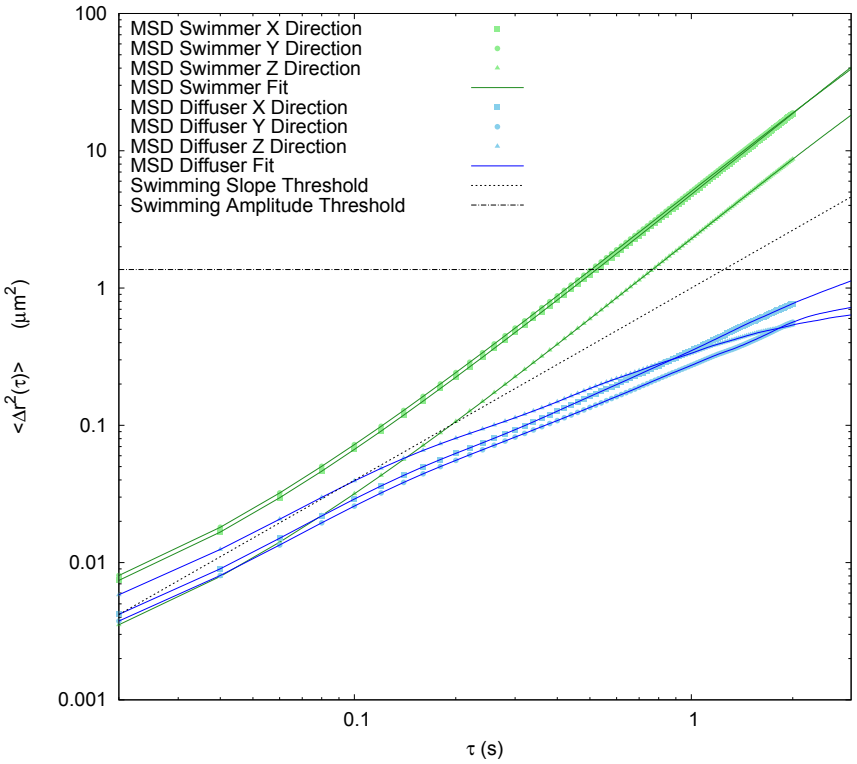

FIGURE 4.7. Mean squared displacement (MSD) thresholds for sorting swimmers and diffusers. Coloured points and line denote the MSD displacement and fit of a swimming cell (green) and a diffusing cell (blue). Horizontal dashed line represents the amplitude threshold, the diagonal dashed line is the gradient threshold.

Swimming and diffusive cells were separated using bespoke LabVIEW software. For the purposes of this thesis, only swimming cells were considered in further analysis steps.

4.3.4 Isolating Reorientations

Reorientations were isolated from the spline-smoothed, swimming trajectories. Purpose-built LabVIEW code calculated the instantaneous velocity and angle change between each data-point, before applying a peak-fitting algorithm to each track (figure 4.8). User-defined thresholds for the minimum height and width of the peaks could be set to ensure accurate detection of re-orientation events. For noisy tracks, the data could be manually re-splined at this point, to assist in the capture of major track features.

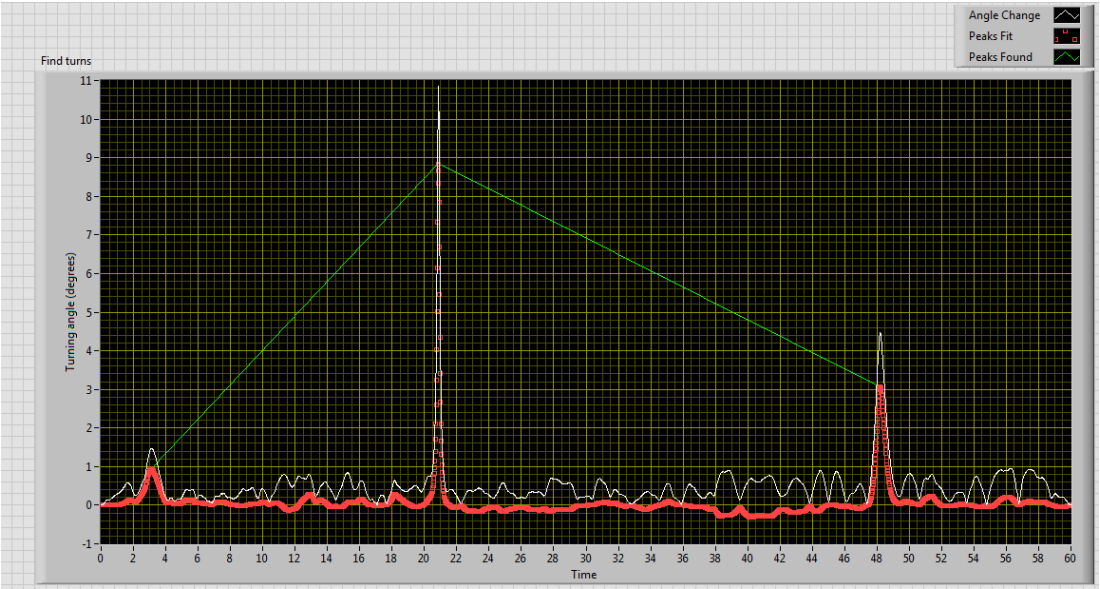

FIGURE 4.8. An example trajectory with the peak-fitting algorithm applied. White line denotes the raw turning angle data, red points represent the fitted peak, and the green line highlights the three reorientation events isolated from this trajectory.

When the turning events have been isolated, each track can be divided into 'runs'. These 'runs' are defined as periods of straight swimming flanked by reorientation events. Only those runs flanked by turning events are included in the 'run' analyses, to ensure accurate values for run durations are captured. Similarly, all reorientation events must be flanked by periods of straight swimming, or are discounted from turning angle analyses.

Chapter 5

Preliminary Motility Experiments

5.1 Introduction

Microorganisms typically experience four key stages of growth (figure 5.1). After initial inoculation into a new medium, there is a short lag phase where cells are adapting to the new medium and cell division is slow. This is followed by the exponential phase, where growth is not limited and the number of new cells is proportional to the existing number of cells. It is during the late section of the exponential phase that cells are typically removed for optical experiments. However, this is primarily due to the population of cells reaching an optimal concentration for optical imaging. The exponential growth phase is followed by a stationary growth phase, this usually occurs due to the depletion of a particular nutrient, limiting the rate of growth of the population. Finally, the cell culture enters a declining phase usually because of the over-exploitation of available nutrients, leading to cell death.

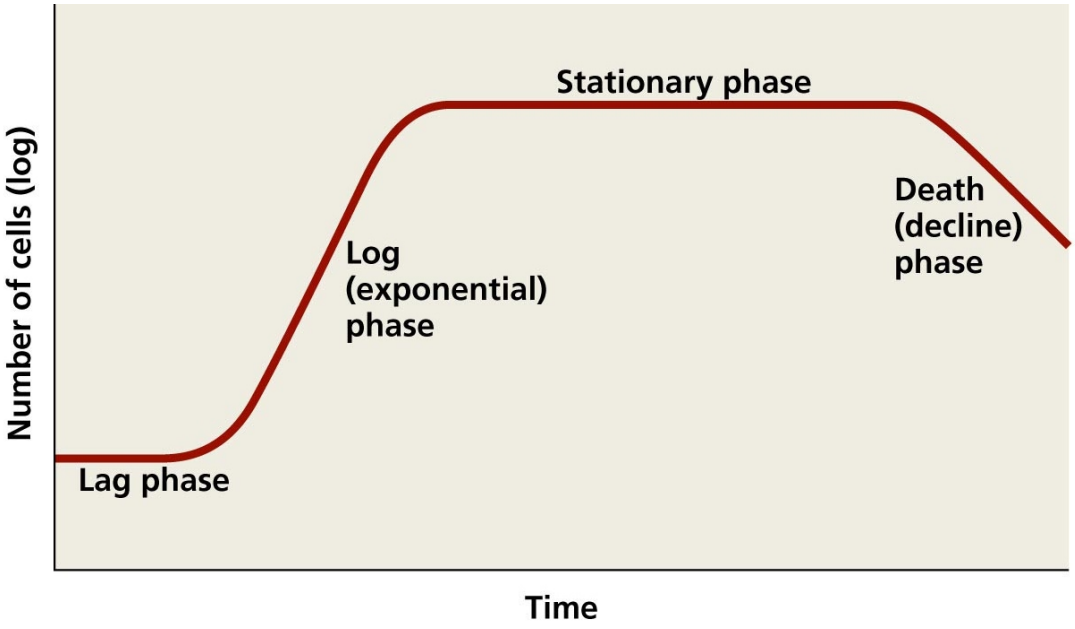

FIGURE 5.1. The four main microbial growth stages [143]. The actual time spent within each stage varies considerably between species and growth conditions.

Optimising the growth conditions for the study samples is vital for ensuring rapid growth rates and high concentrations of cells, without which, unnatural behaviours may be observed.

5.2 Methods

Unlike many key laboratory strains of bacteria (*E. coli, B. subtilis* etc.), which have clearly defined laboratory growth conditions, the environmental organisms used within this thesis are much less well defined. Whilst several growth protocols have been outlined in the halo-handbook [45], these are generally restricted to laboratory strains of individual species, and optimised for other purposes than to increase motility.

Microbial growth rates are typically quantified through spectrophotometry, as there is a clear linear relationship between the concentration of a sample, and the amount of light it absorbs (Beer-Lambert Law). It is standard practice when assessing bacterial cell densities to measure the light absorbence at 600 nm wavelength, using a spectrophotometer. Repeated readings over time can be used to produce growth curves to reliably predict the growth stage of a cell population

at any given time. Given the inherent red pigment in haloarchaeal cells, full-wavelength scans were performed to check for any atypical absorption around the 600 nm regions (V-3000PC Spectrophotometer) (figure 5.2). Both media and saturated cell samples showed no fluctuations at the 600 nm region, therefore 600 nm wavelength of light was used for all future readings.

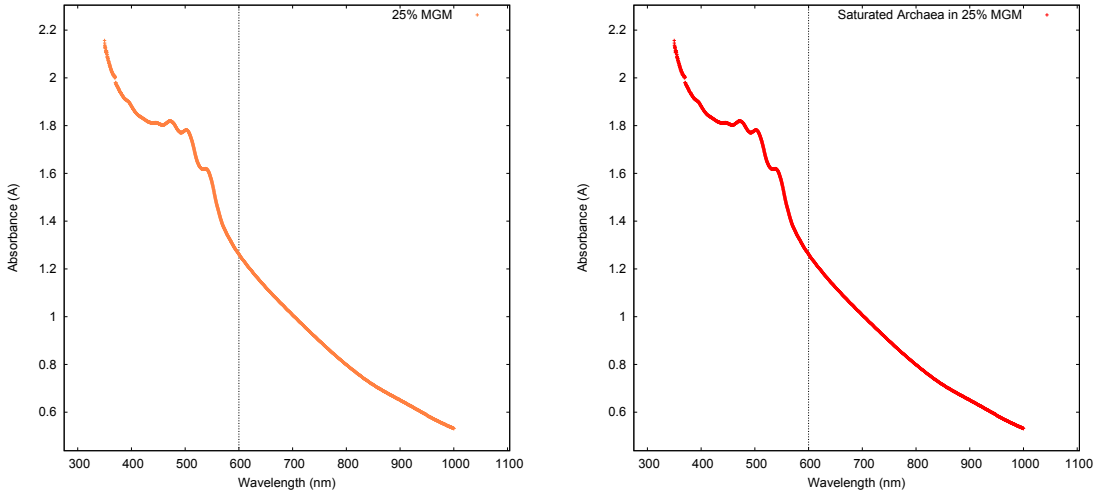

Figure 5.2: *Left*: spectrophotometer full wavelength scan of 25 % salt modified growth media (MGM). *Right*: spectrophotometer full wavelength scan of saturated archaea culture in 25 % salt modified growth media (MGM).

5.2.1 Optimising the Growth Media

Cells were originally cultured in a nutrient-rich, high-salt medium (modified growth medium). The recipe for which can be found in Appendix A01. To optimize the salt concentration within the growth medium, cells were cultured (45 °C at 150 rpm) from frozen in MGM at varying salt concentrations (12 %, 18 %, 23 % and 25 %). Spectrophotometer readings were taken at intervals over a 3-day period, to generate a growth curve (figure 5.3).

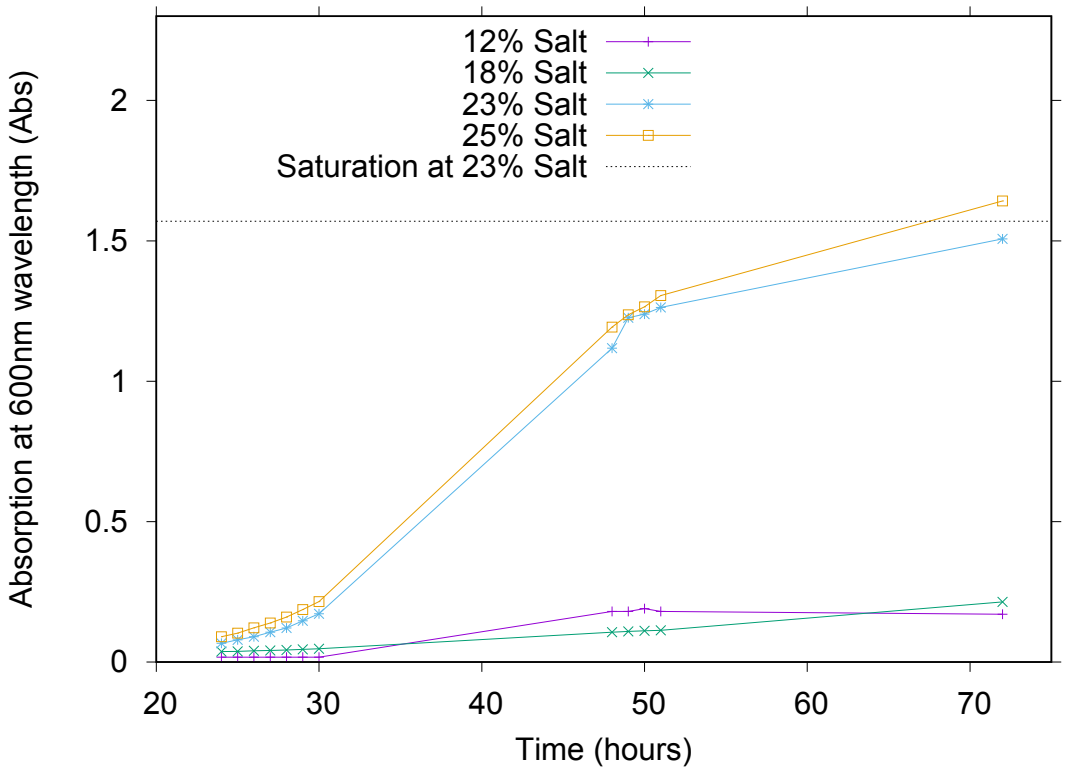

FIGURE 5.3. Growth curve of *H. hispanica* cultured from frozen stock in varying salt concentrations of modified growth media (MGM). Dashed line denotes the cell saturation level, when cultured at 23 % MGM.

The graph clearly shows that individuals grow preferentially within the higher salt concentrations (23 % and 25 %), with 25 % salt producing the overall highest yield. Higher concentrations of salt than those tested were impractical due to the increased likelihood of reaching saturation levels. Consequently, 25 % salt was chosen for the growth of cells in MGM.

Although the archaeal cells were successfully cultured in MGM, studies suggested that chemically defined medium was preferential for some species of haloarchaea [144]. Chemically defined medium is a minimal medium (full recipe in Appendix D) with fewer nutrients, but a wider variety of chemical compounds. Samples were cultured (45 °C at 150 rpm) from frozen stock in both media types and growth rates were analysed via spectrophotometry (figure 5.4).

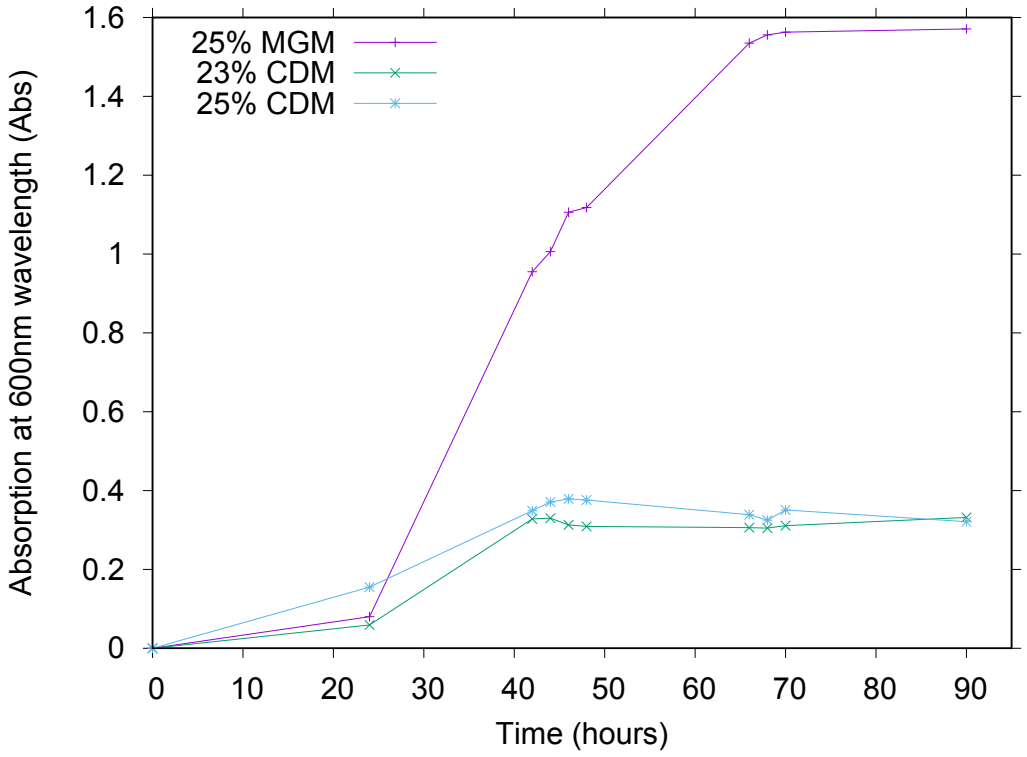

FIGURE 5.4. Growth curve of *H. hispanica* cultured from frozen stock in modified growth medium and chemically defined medium.

Figure 5.4 shows the rapid growth and cell density in MGM compared with CDM. Given the stark difference in growth rates, MGM was selected for use in all further experiments.

A growth rate curve was produced for all three samples, in 25 % MGM. Cells were grown to saturation in MGM 25 % media, stored for 24 hours at 4 °C, then re-inoculated in fresh media. Spectrophotometry readings were taken at regular intervals and plotted (figure 5.5). These readings were combined with dark-field spectrophotometry videos recorded at the same time-points, to establish an optimum incubation period for the motility experiments.

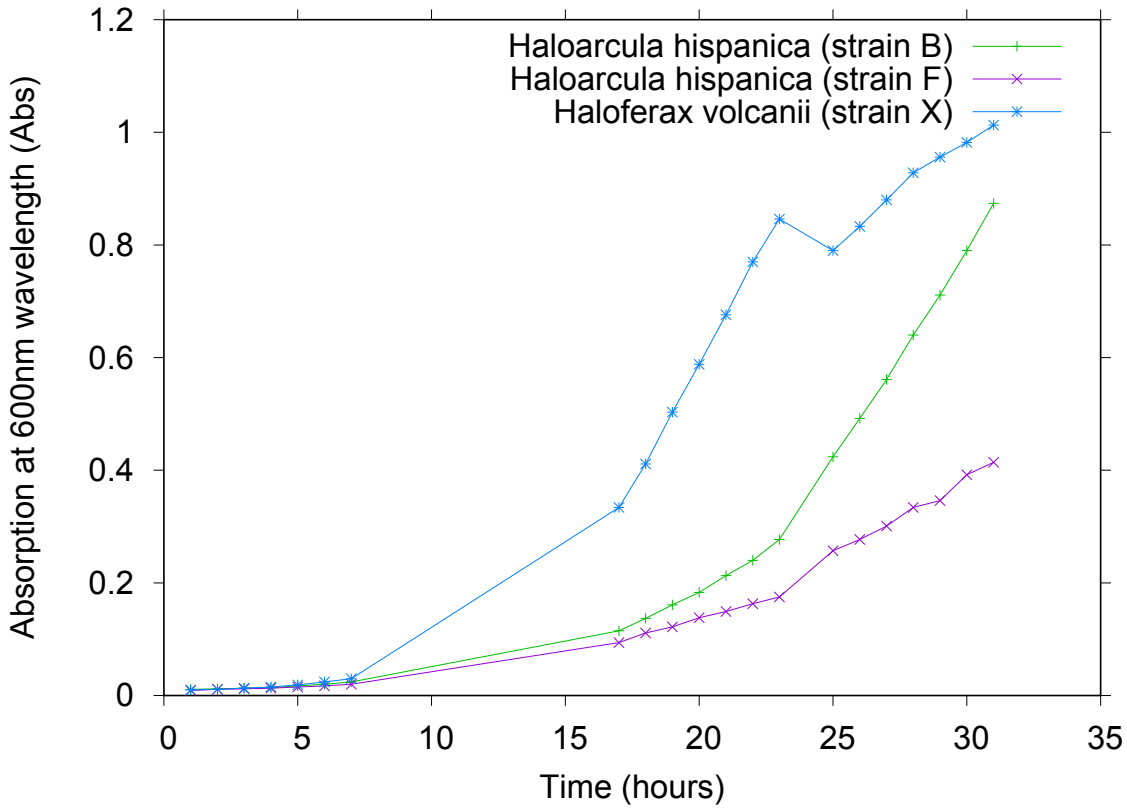

FIGURE 5.5. Growth curve for each strain of archaea. Cells were cultured in 25 % modified growth medium (MGM) from saturated refrigerated stock.

Figure 5.5 shows the cells enter early exponential phase after approximately 17-20 hours incubation. *Hx. volcanii* showed increased growth rates compared to both strains B and F of *H. hispanica*. The cultures are expected to reach saturation stage at approximately 1.6 Abs, as was the case in figures 5.3 and 5.4. Consequently, it can be estimated that at 17-30 hours incubation, these haloarchaeal cells would be undergoing exponential growth.

5.2.2 Dark Field Spectroscopy

Dark field videos were taken alongside the growth-rate curves, for each of the three strains (B, F, X). Videos were recorded using the optical set-up described in section 3.6.1, at a rate of 50 Hz. The power spectral density was plotted as a function of frequency as in [104]. A peak fitting algorithm (in-built LabVIEW was applied to the data, to isolate the centre of peaks corresponding to body-rotation rate (see section 3.3). Figure 5.6 shows an example power spectral density plot

with a clear, well-fitted peak at 2.7344 Hz. This value falls in-line with observed body rotation rates from other species of haloarchaea [83].

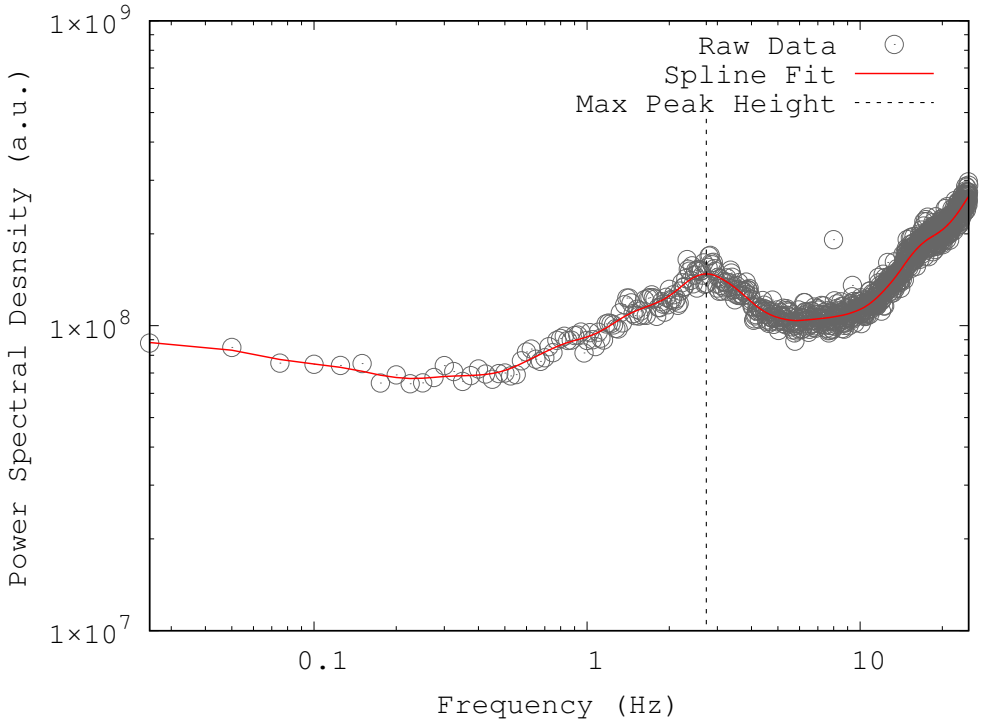

FIGURE 5.6. Dark field spectroscopy example of power spectral density, showing an archaeal body rotation rate peak at 2.7344 Hz. A sharp noise spike can be observed at a frequency of approximately 8 Hz, which is generated by the the power supply in the microscope. This spike is much higher than the region of interest, so for the purposes of this thesis was ignored. Other noise generated by the camera was typically random, and therefore frequency independent (see figure 3.9).

However, due to the large non-motile percentage of cells within these samples, the isolation of clear peak, representative of the cell body rotation rate can be challenging. At low concentrations body rotation signals can be dampened by other noise within the sample. Figure 5.7 is an example of a power spectral density plot where the body rotation peak was difficult to reliably extract, even with the application of peak-fitting software.

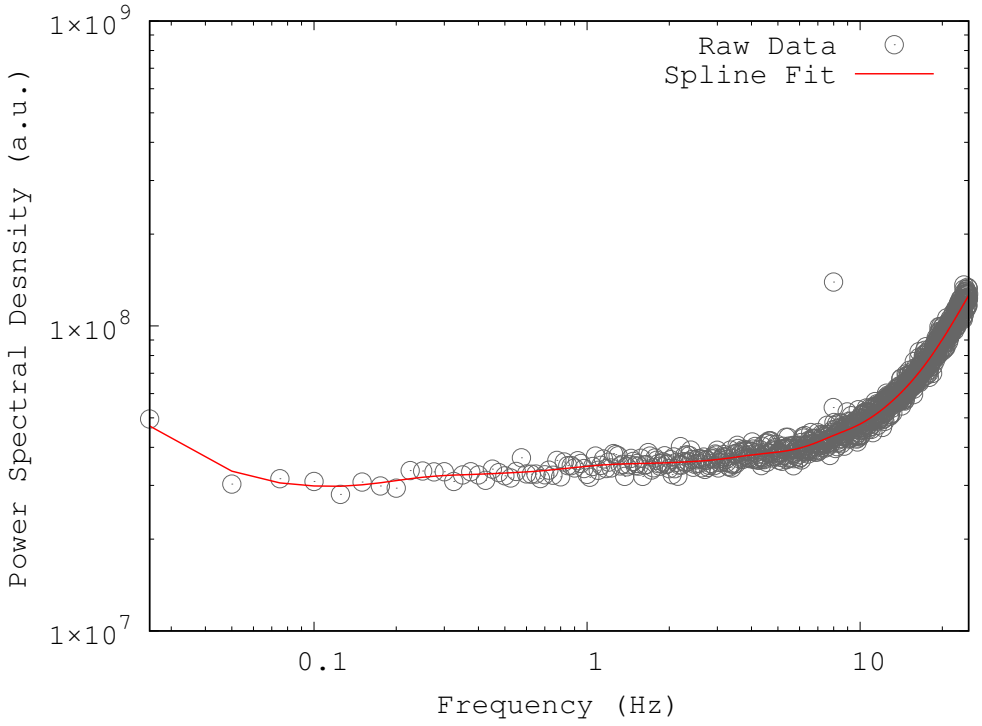

FIGURE 5.7. Dark field spectroscopy example power spectral density, with a low signal to noise ratio, therefore lacking an easily discernible peak. A sharp noise spike can be observed at a frequency of approximately 8 Hz, which is generated by the the power supply in the microscope. This spike is much higher than the region of interest, so for the purposes of this thesis was ignored. Other noise generated by the camera was typically random, and therefore frequency independent (see figure 3.9).

5.3 Results

At each time point, for each sample, the power spectral density extracted from the dark field videos was plotted as a function of frequency. Whilst videos recorded early within the growth cycle were relatively easy to locate the centre of the fitted peak, those videos recorded later within the growth stage were inconclusive. Figure 5.8 shows the centre of the peak detected at each time point, for each of the three strains. Shaded regions denote ambiguity in the exact position of the centre. Data files where a peak could not be reliably fitted were omitted from the results. None of the videos taken after the 24 hour period could reliably yield a value for the body rotation rate.

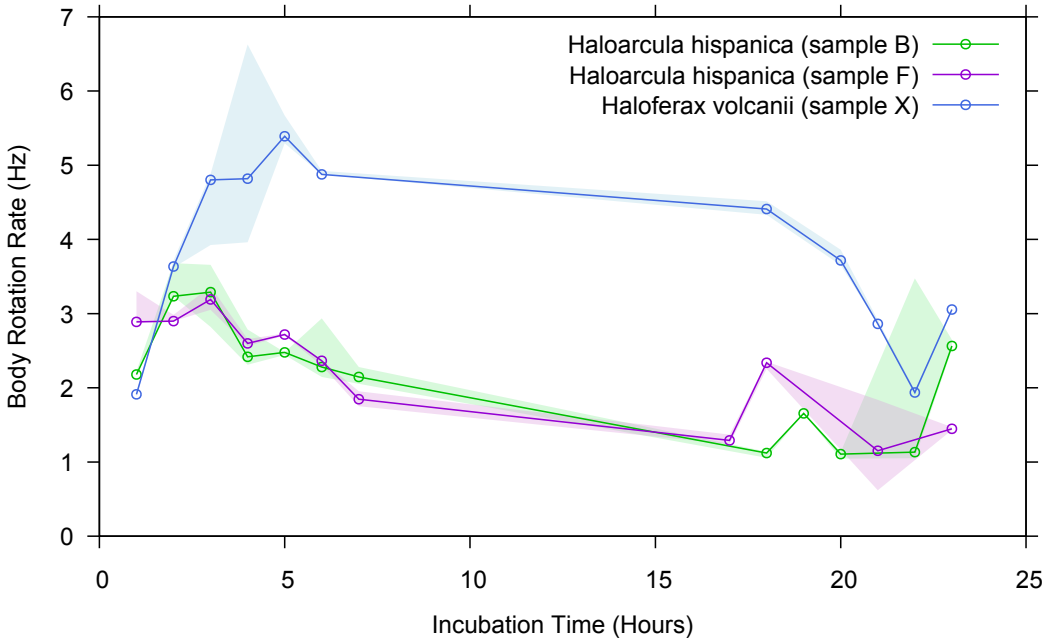

FIGURE 5.8. Dark field spectroscopy body rotation rate over time. Points denote the centre of the fitted body rotation peak, shaded regions denote areas of ambiguity in the exact positioning of the peak centre

5.4 Discussion

The dark field videos showed that cells had faster body rotation rates within the first 5 hours of incubation. After this period rotation rates began to decline, indicating a probable decline in motility. After 24 hours the body rotation rates were no-longer discernible from the dark field spectroscopy data. Given these results it would be preferable to image at very low cell concentrations. However, figure 5.5 indicated that the cells did not reach early exponential growth until approximately 17-20 hours after incubation. Therefore, it would be impractical to image before this time, as cell concentrations would be too low to reliably capture holographic data. Consequently, an incubation time of 18 hours was selected, as this enabled early exponential growth, and relatively high body rotation rates. An incubation period of 18 hours should provide sufficient cell concentrations for imaging, whilst also maintaining good levels of motility.

Furthermore, growth levels were significantly lower in the reduced salt concentrations and in chemically defined medium than in the 25% MGM. Consequently, 25% modified growth medium was selected as the most appropriate media type for all future experiments.

Chapter 6

3D Tracking

6.1 Introduction

Synthesising motility appendages and powering the rotary motor to enable the ability to swim is an energetically expensive pursuit for many microorganisms. The main benefit of swimming is the capability to detect chemical gradients and move towards, or remain in, nutrient rich environments [4]. To achieve this, individuals must modify their swimming behaviours in response to external stimuli, reorientating towards favourable conditions. This is forms the basis of chemotaxis.

This chapter focuses on the swimming behaviours displayed by motile prokaryotic cells. Whilst tracking a chemical gradient is beyond the scope of this thesis, the behaviours observed within experimentation are likely to form the basis of a chemotactic response, being modified in frequency or duration in the presence of a stimulus. Here, digital holographic microscopy is utilised to collect the three-dimensional swimming trajectories of the three samples under investigation (*H. hispanica* B & F, and *Hx. volcanii* X).

6.1.1 Micro-swimming Patterns

In order to change direction, cells must either stop or reverse the rotation of the motor driving the filament. The most iconic of these reorientation behaviours is the 'run and tumble' (formerly twiddle), first observed in *Escherichia coli* in 1972 [111]. The run-and-tumble behaviour is generally observed in cells with multiple flagella, and a 'tumble' reorientation occurs when one or more of the flagella motors reverse their direction, throwing the cell off axis in a random direction (figure 6.1). In polar, mono-flagellated cells, reversals typically occur

in place of the tumble behaviour. If a cell is being 'pushed' by a single filament, when it switches rotation direction the cell will be 'pulled' along in the direction it appeared from (figure 6.1). However, because of the reorientational effects of Brownian motion, the cell is diverted slightly off course and never revisits exactly the same path twice.

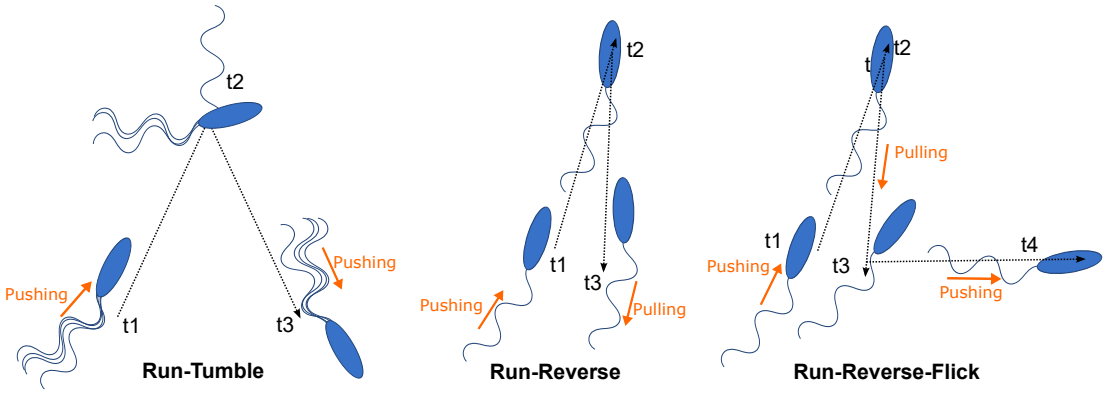

FIGURE 6.1. Schematic of the three main reorientation types exhibited by freely swimming bacteria. Black arrows denote cell swimming direction, orange arrows and text highlight whether the flagellum is 'pushing' or 'pulling' the cell body.

For polar flagellated bacterial (and possibly archaeal) cells containing a flexible hook, the reversal of the motor direction can lead to a 'flicking' reorientation behaviour. These flick motility behaviours occur between the typical run-reverse motion, through the buckling of the hook region when 'pushing' after a period of 'pulling' (figure 6.2), which 'flicks' the cell in a random direction.

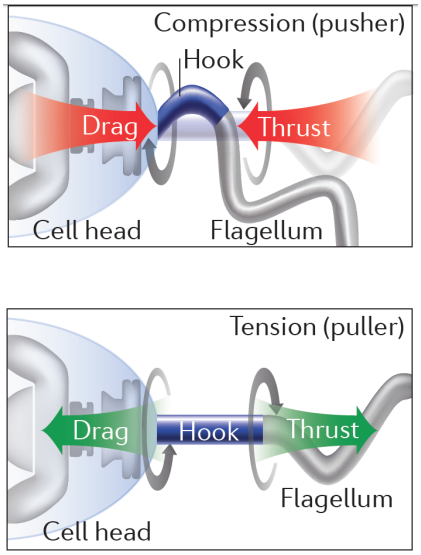

FIGURE 6.2. Example of a bacterial Flagella Hook [117]

6.2 Methods

The following conditions were maintained throughout all tracking experiments used within this thesis. The optical set-up was as previously discussed in chapter 3. A 642 nm laser fibre was placed directly above the sample holder at a distance of 2-5 cm from the stage. Once positioned, the laser was switched on and allowed to warm-up for at least 30 minutes prior to imaging, to ensure thermal equilibrium had been reached, in an attempt to limit the variations in stability and drift associated with temperature fluctuations [145].

6.2.1 Preparing Samples

For holography experiments, cells were cultured in MGM 25 % via the addition of 50 μl of saturated culture to 10 ml of media, (measured using micro-pipette and serological pipette respectively). Flasks were incubated and shaken for 18 hours at 45 °C and 150 rpm (as in previous experiments). After the incubation period cells were removed from the incubator and placed in custom-built chamber slides for imaging.

When studying motile cells, standard flat microscope slides can restrict swimming behaviours to almost two-dimensions due to the narrow depth of fluid between the two glass surfaces. Furthermore, cells swimming close to a solid boundary often display abnormal behaviours known as 'wall effects' resulting from the non-slip layer of fluid directly adjacent to the boundary [146]. These

behaviours usually involve a significant increase in observed circular swimming patterns, reduction in reorientation events, and an increased risk of cells becoming stuck or trapped directly on the surface [147, 148]. The closer to the boundary, the greater the observed behavioural changes. At a distance of approximately 20 μm [148] there appears to be little or no effect on the swimming behaviours of microorganisms. In an effort to reduce any boundary effects on the samples, chamber slides were created to increase the depth of the sample. These bespoke chamber slides were created (figure 6.3) using two standard glass cover slips glued (Norland Optical Adhesive) to a flat microscope slide to create a channel. This was then covered with a long cover slip, creating a chamber approximately (10×26×2.5 mm) in size.

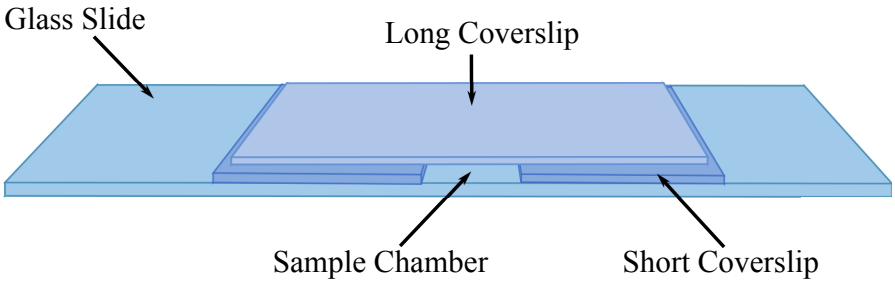

FIGURE 6.3. Schematic of the bespoke chamber slides used in holographic experiments. All components were fixed using optical glue and sample chamber edges sealed using petroleum jelly.

Chambers were filled using a micro-pipette with sterile disposable tip under sterile conditions. Chambers were then sealed with petroleum jelly, appropriately labelled and inverted (to ensure imaging through cover-glass rather than thicker slide side). If cell concentrations appeared too high on initial observations, then a portion of the remaining culture was diluted using MGM 25 % and a new slide prepared.

6.2.2 Video Capture

Holographic videos were captured at 50 Hz using a × 20 magnification objective (as described in section 3.6.2). Samples were positioned such that the videos were captured from the centre of the sample chamber, to minimise wall effects. The microscope focal plane was positioned approximately 50 μm below the bottom surface of the chamber slide to enable the video capture of the entire chamber from below. All imaging was undertaken at room temperature (22 °C). These conditions were replicated over several days of experimentation.

The captured region was 512×512 pixels at the centre of the camera sensor. Exposure times and gain levels varied slightly between individual samples, as they were manually adjusted to maximises contrast between the holograms and the background. 3000 frames of video footage were captured for each video at a rate of 50 Hz, and saved in an uncompressed format. 20-25 videos were included in the analysis for each sample.

6.3 Holography Results

This results section compares the motility features of all of the trajectories for each of the three strains. After the computational analysis steps have been completed, individual trajectories can be selected and analysed in more depth.

Figure 6.3 shows a representative, 1 minute long trajectory from each sample, plotted in 3D. The coloured lines represent the raw unsmoothed data, and therefore display extensive fluctuations from the smoothed path. At this small scale, Brownian motion can account for a significant proportion of these fluctuations. However, it is likely an additional 'wobble' generated through off-axis positioning of the archaellum filament (as observed by Kinesota *et al.* [83]) is also present. Furthermore, previous work has indicated that changes in cell body shape can significantly impact observed swimming behaviours [149]. Due to the pleiomorphic nature of archaeal cells, any small variations in body shape could also contribute to minor deviations from the straight-line swimming. In both the smoothed and raw data, the reorientation events are clearly distinguishable between long periods of straight swimming.

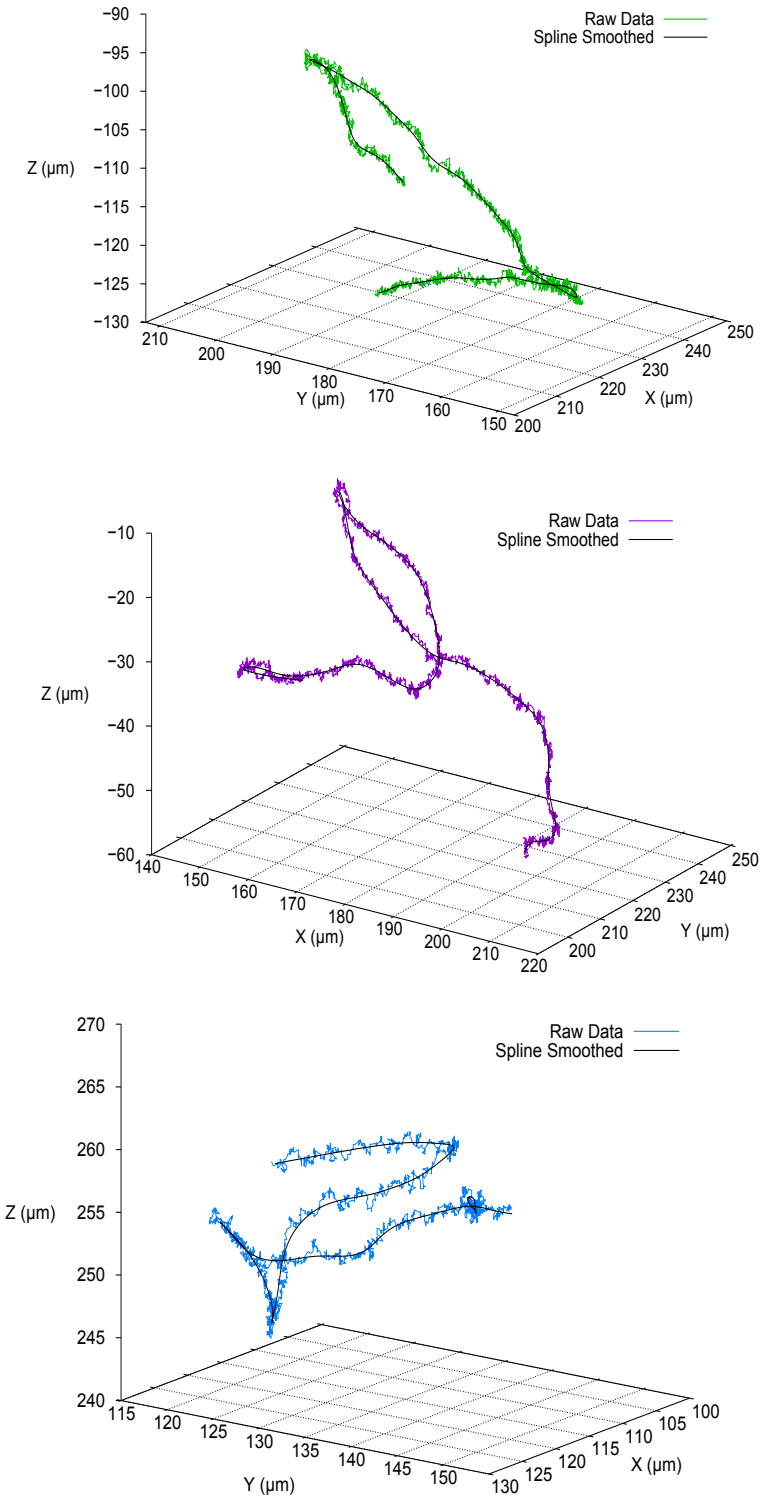

FIGURE 6.4. Example 3D trajectories from each of the study species. *Top*: *H. hispanica* sample B, *Middle*: *H. hispanica* sample F, *Bottom*: *Hx. volcanii* sample X. Coloured lines represent the raw data, black lines indicate the spline-smoothed. All three trajectories are 60 seconds in duration, imaged at 50 fps. x, y and z are all measured in μm from the position 0,0,0. Negative z values occur when imaging from the top of the sample chamber down vs the bottom of the sample chamber up.

6.3.1 Motile Percentage

All of the trajectories from each video were grouped together for each of the three archaeal strains (*H. hispanica* B, *H. hispanica* F and *Hx. volcanii* X, respectively). Trajectories were sorted into swimmers and diffusers based on the mean squared displacement of the trajectory as a whole (figure 6.5). The percentage of motile cells recorded was very low $< 20\%$ for each of the three samples. This data is likely to include diffusing particles (not cells) and may capture the same diffusing object on multiple occasions, providing a slightly skewed dataset. However, given the significantly lower swimming portion of tracks, it can be inferred that many of the individuals within the sample are non-motile. This supports the earlier dark-field findings in section 5.3.

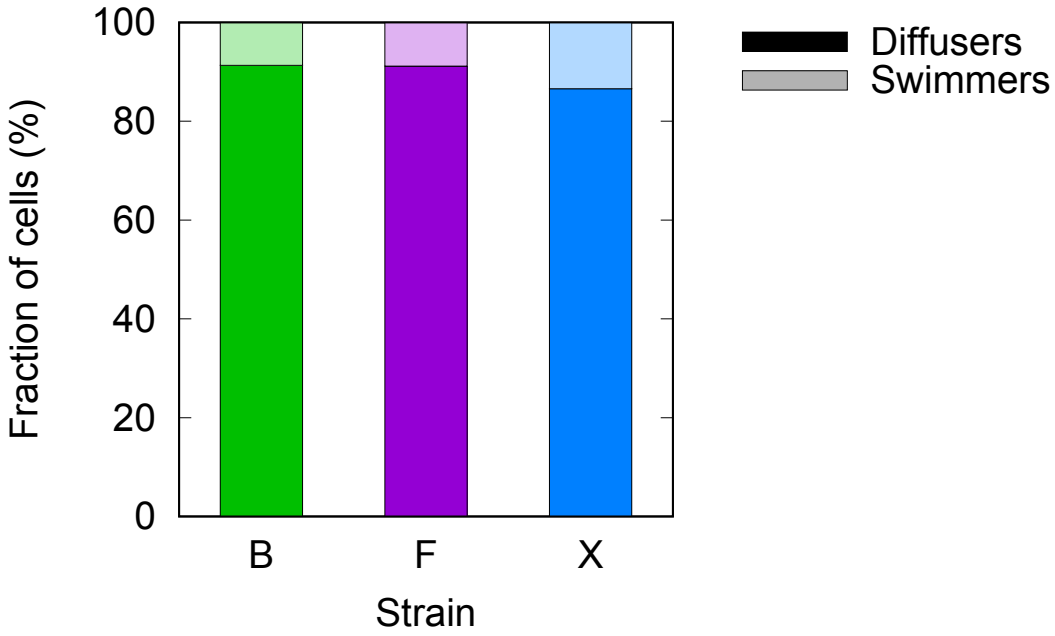

FIGURE 6.5. Percentage of swimmers vs diffusers, solid colour denotes diffusing trajectories, translucent colour denotes the swimming portion. The total number of recorded trajectories are; B = 29,098, F = 28, 231 and X = 17,003.

For the remaining analyses, only the swimming trajectories will be considered.

6.3.2 Swimming Speed

As an initial measure of motility, the instantaneous velocity was calculated for each of the three strains imaged. Videos were recorded at 50 Hz, therefore each cell's position was recorded every 20 ms. Instantaneous velocity (v_i) was calculated as:

$$v_i = \frac{\sqrt{(x_{i+1} - x_i)^2 + (y_{i+1} - y_i)^2 + (z_{i+1} - z_i)^2}}{(t_{i+1} - t_i)} \tag{6.1}$$

Where x_i, y_i, z_i represent the 3D co-ordinates of an individual cell's position, at a particular time point (t_i). The distribution of instantaneous velocity across the whole population was examined by creating histograms for each of the three samples (figure 6.6). A Gaussian peak was fitted to each of the histograms in turn. The centre of the fitted peak provided an average swimming speed of approximately 2 μms^{-1} for each of the three strains. Slight variations were observed between the three samples; *Haloarcula hispanica* strain F had the highest average instantaneous velocity 2.27 +/- 0.84 μms^{-1} (centre of peak +/- standard deviation of fit for 3,992,312 data points). *Haloarcula hispanica* strain B had an instantaneous velocity of 2.09 +/- 0.73 μms^{-1} (centre of peak +/- standard deviation of fit for 2,529,938 data points) and *Haloferax volcanii* had an average velocity of 1.98 +/- 0.72 μms^{-1} (centre of peak +/- standard deviation of fit for 2,343,831 data points).

The data for all three strains produced remarkably symmetrical Gaussian bell curves, suggesting the population swimming speeds are normally distributed around the mean with few extreme values or outliers. There is slight skewness to the right, indicating a slight tendency to swim slightly faster than the mean.

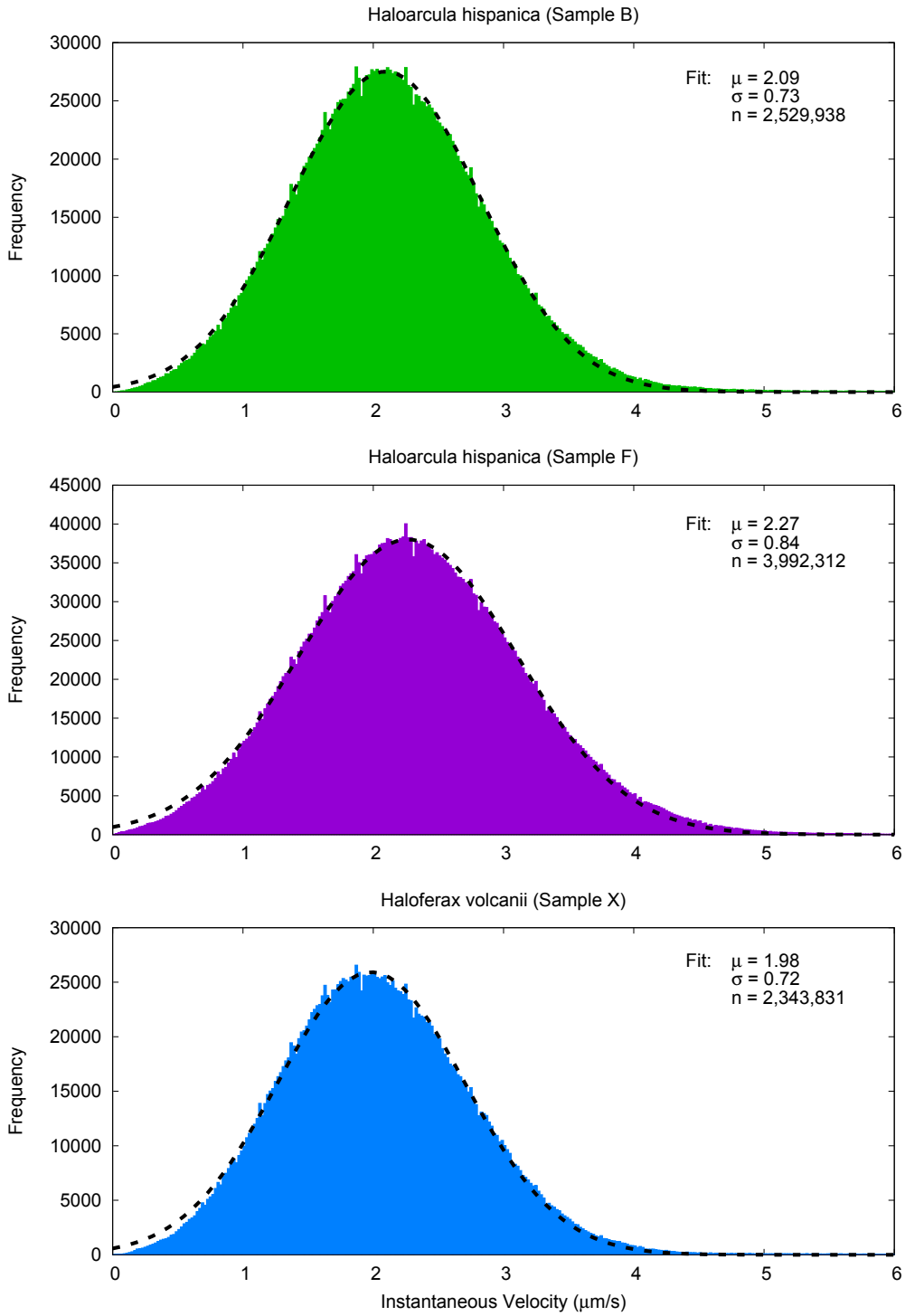

FIGURE 6.6. Instantaneous velocity histograms. Top to bottom: *Haloarcula hispanica* population 1 (sample B), *Haloarcula hispanica* population 2 (sample F) and *Haloferax volcanii* (sample X). Dashed black line represents best Gaussian fit, based on μ (mean) and σ (standard deviation) values for n data points extracted from >2000 tracks for each strain. (Whilst most tracks will represent unique individuals, some cells may be imaged on multiple occasions at different points within the sample, if they move in and out of the frame of reference.)

Figure 6.7 shows a series of histograms where the mean speed for each individual track was plotted. When looking at the average velocity across tracks as a whole, only slight variations occurred compared with the raw data. *Haloarcula hispanica* strain B had an instantaneous velocity of 2.04 +/- 0.47 μms^{-1} (centre of peak +/- standard deviation of peak for 2519 tracks). The reduction in standard deviation suggests that there are bigger variations in speed occurring within individual tracks than between different tracks. Furthermore, the slight reduction in average speed could either be an indication of faster tracks being longer than slower ones. *Haloarcula hispanica* strain F still had the highest instantaneous velocity 2.16 +/- 0.59 μms^{-1} (centre of peak +/- standard deviation of peak for 2721 tracks), similar to strain B, the mean track average and standard deviation values were slightly lower than the population whole. *Haloferax volcanii* had an average velocity of 2.00 +/- 0.52 μms^{-1} for the track values (centre of peak +/- standard deviation of fit for 2390 data points). Similar to the GSL strains, this showed a slight reduction in standard deviation from the population, suggesting greater speed variations within individual tracks rather than between. However, there was a slight reduction in the average swimming speed observed, suggesting that the slower tracks were perhaps longer than faster counterparts.

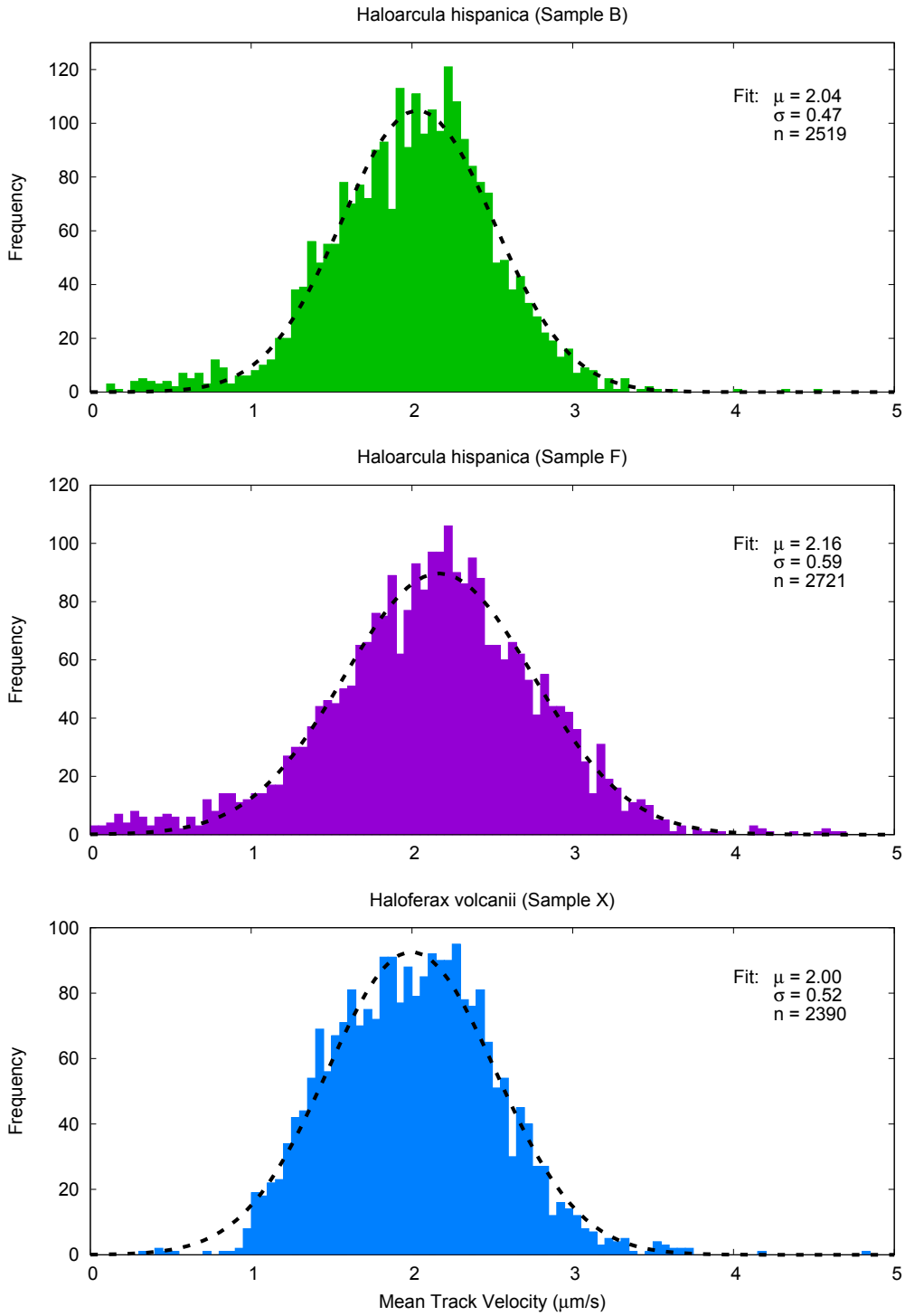

FIGURE 6.7. Mean track speed histograms. Top to bottom: *Haloarcula hispanica* population 1 (sample B), *Haloarcula hispanica* population 2 (sample F) and *Haloferax volcanii* (sample X). Dashed black line represents best Gaussian fit, based on μ (mean) and σ (standard deviation) values for n number of tracks for each strain. (Whilst most tracks will represent unique individuals, some cells may be imaged on multiple occasions at different points within the sample, if they move in and out of the frame of reference.)

The mean squared displacement (MSD) was calculated for each time interval τ, within each track, and averaged across all the tracks collected for each sample. MSD was calculated as;

$$MSD = < \Delta r^2(\tau) > = \frac{1}{n} \sum_{i=1}^{n} r_i^2(\tau) \tag{6.2}$$

$$< \Delta r^2(\tau) > = < \Delta x^2(\tau) > + < \Delta y^2(\tau) > + < \Delta z^2(\tau) > \tag{6.3}$$

Whereby τ is the time interval and Δx is the change in x position. The resulting values were plotted (figure 6.8).

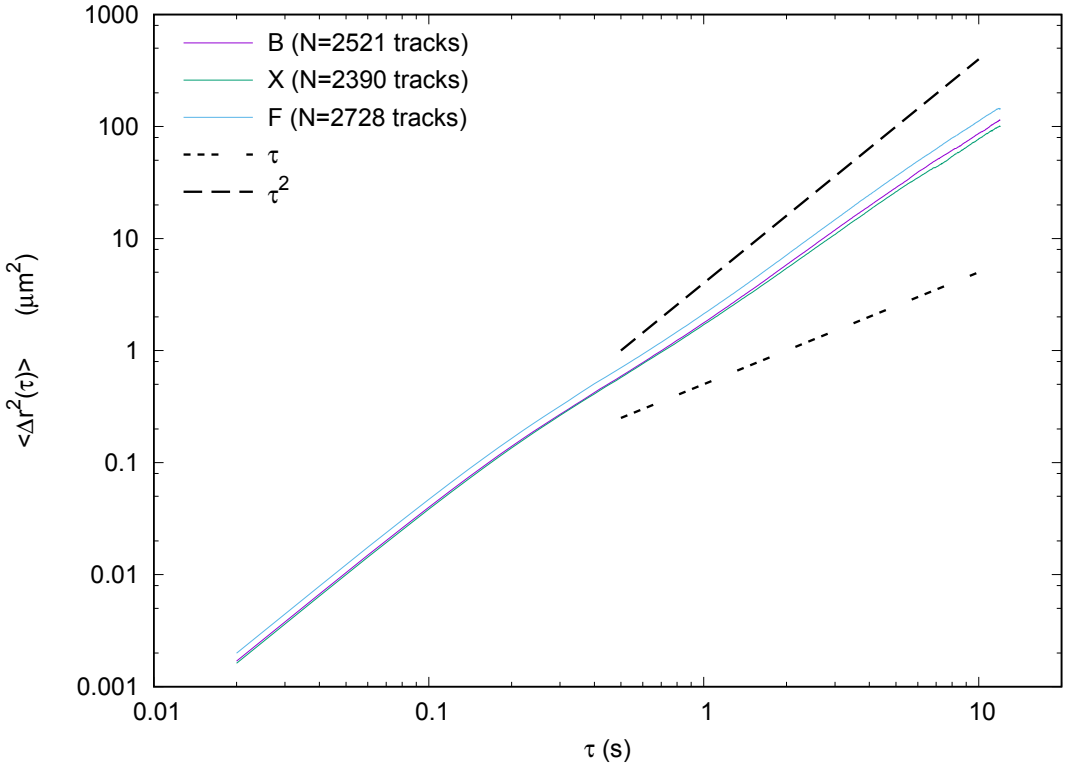

FIGURE 6.8. Mean Squared Displacement. Top to bottom: *Haloarcula hispanica* (sample B), *Haloarcula hispanica* (sample F) and *Haloferax volcanii* (sample X). Figure legend shows the number of tracks included for each strain, dashed lines denote expected values for τ and τ^2.

Only slight variations in the MSD were observed between the samples. All three samples showed a slight tendency away from diffusive motion at longer time-scales. Sample F was marginally less diffusive than B or X.

6.3.3 Runs

A 'run' refers to a period of straight-line swimming, without any active reorientation mechanisms. Runs typically encapsulate the fastest swimming speeds undertaken by a micro-organism, but are never truly straight at this scale, as they are still subjected to the rotational (and translational) effects of Brownian motion.

Figure 6.9 shows a series of histograms where the run durations for each sample were plotted. These values were plotted on a semi-log graph, to look for exponential trends in the run lengths. Modulating the run-length is a well characterised chemotactic response in *E. coli*, with exponential run duration distributions frequently being observed [111]. The run durations observed within the haloarchaeal samples revealed a vaguely exponential trend, which would perhaps be more pronounced with greater sampling numbers.

Haloarcula hispanica strain B had a mean run duration of 13.55 +/- 11.23 seconds (mean +/- standard deviation for 527 runs). *Haloarcula hispanica* strain F had a slightly shorter mean run length of 12.52 +/- 10.86 seconds (mean +/- standard deviation for 982 runs). *Haloferax volcanii* had an average run time of 13.63 +/- 12.12 seconds (mean +/- standard deviation 405 data points). These values are much higher than ≈ 1 second run durations typically observed within many bacterial species [111].

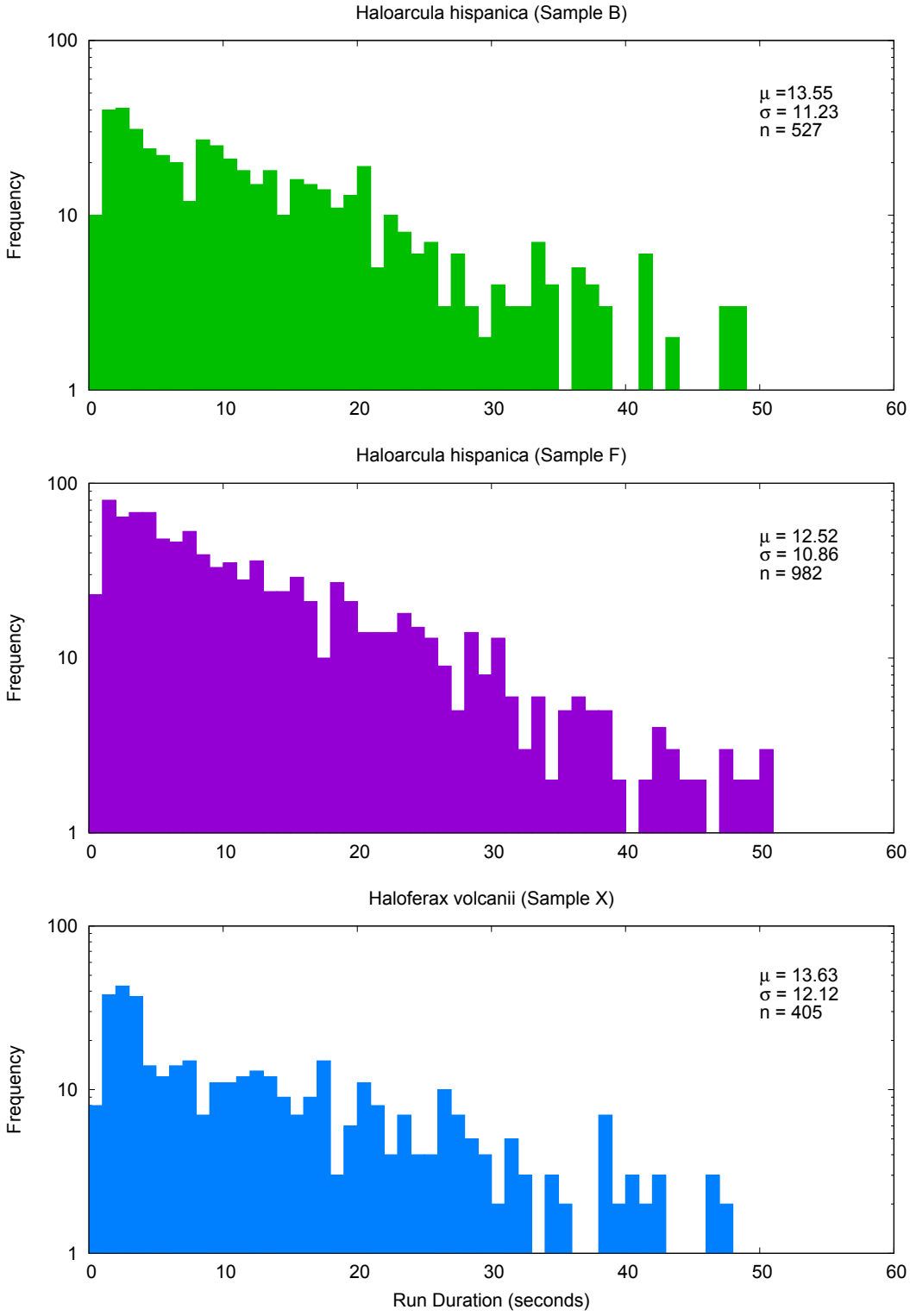

FIGURE 6.9. Run duration histograms. Top to bottom: *Haloarcula hispanica* population 1 (sample B), *Haloarcula hispanica* population 2 (sample F) and *Haloferax volcanii* (sample X). Figure legend shows μ (mean) and σ (standard deviation) values for n number of complete runs (between two reorientation events) for each strain.

Figure 6.10 shows a series of histograms where the distance travelled during a run for each sample were plotted. These values were plotted on a semi-log graph, for ease of comparison with the run durations in figure 6.9. The observed run distances show a similar trend to the run durations, therefore it is likely that short run times equate to a short travel distance. This suggests that cell speed is not affected by run duration. Consequently, as in many bacterial species, individual cells may be unable to modulate speed, but simply increase or decrease the number of reorientation events (and by consequence the duration of each run) in response to chemotactic stimuli [7, 111].

Haloarcula hispanica strain B had a mean run distance of 10.22 +/- 14.39 micrometers (mean +/- standard deviation). *Haloarcula hispanica* strain F had a slightly shorter mean run length of 10.43 +/- 17.14 seconds (mean +/- standard deviation). *Haloferax volcanii* had an average run time of 10.3 +/- 14.76 micrometers (mean +/- standard deviation). The observed run distances follow an exponential trend, with shorter run distances occurring most frequently. Overall, the mean values were slightly lower than expected distances (when considering the mean run time and mean speed of cells) can most likely be attributed to the tortuousness of the swimming path. As previously discussed, although 'runs' can be considered straight swimming, due to additional displacements created by Brownian motion, they are never truly straight.

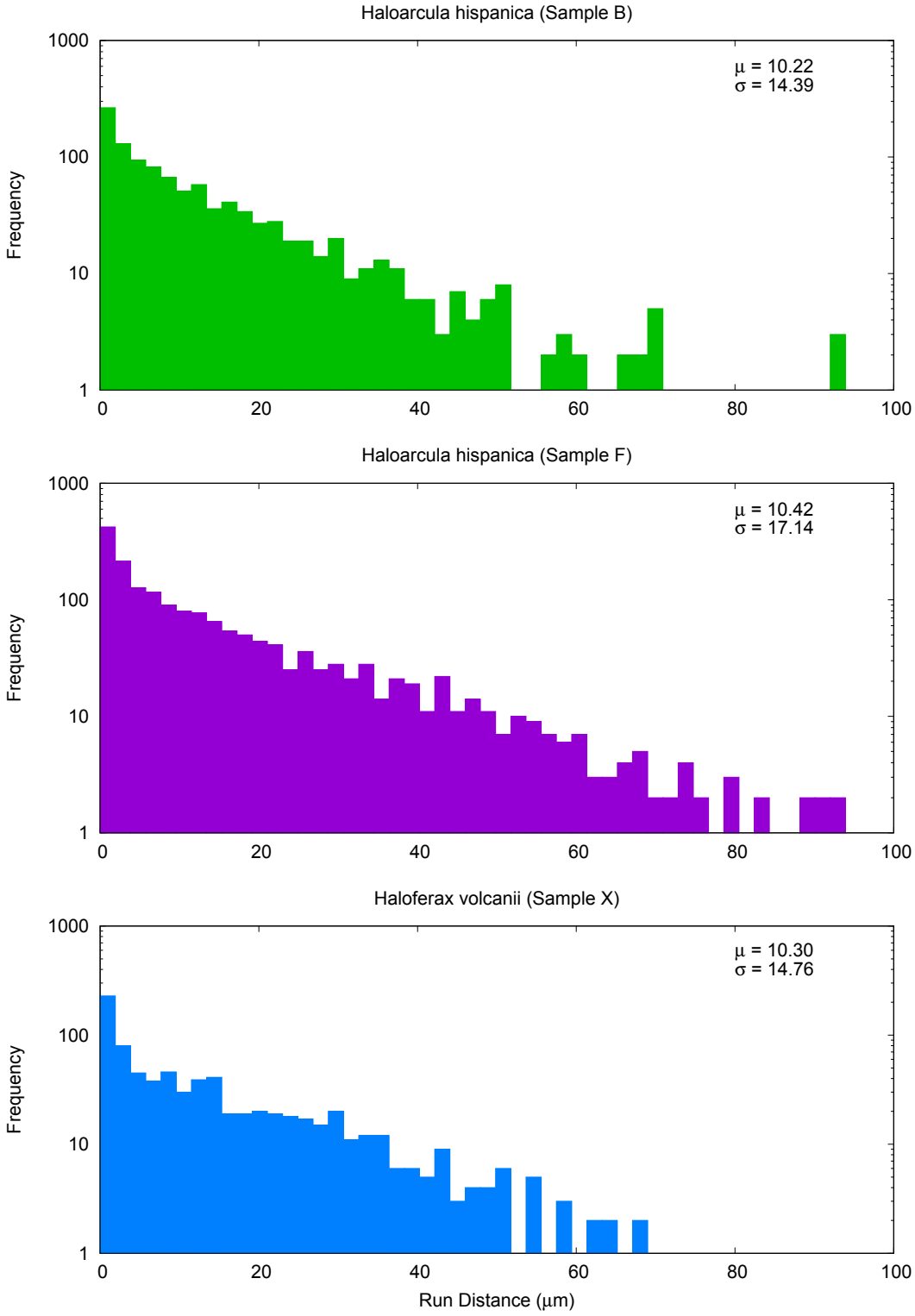

FIGURE 6.10. Run distance histograms. Top to bottom: *Haloarcula hispanica* population 1 (sample B), *Haloarcula hispanica* population 2 (sample F) and *Haloferax volcanii* (sample X). Figure legend shows μ (mean) and σ (standard deviation) values for the distances travelled during all complete runs (between two reorientation events) for each strain.

6.3.4 Reorientations

The reorientation angle was calculated between two vectors before and after a reorientation event. The angle was calculated as; reorientation angle (θ_r):

$$\theta_r = ((\theta_{i+1} - \theta_i) - (\theta_i - \theta_{i-1})) \tag{6.4}$$

Any reorientation events flanked between two runs were included in figure 6.11. *Haloarcula hispanica* strain B had a mean angle of 119.72 +/- 36.78 degrees μms^{-1} (mean +/- standard deviation for 1249 reorientation events). *Haloarcula hispanica* strain F had the highest mean reorientation angle, at 123.43 +/- 36.62 degrees μms^{-1} (mean +/- standard deviation for 2223 reorientation events), *Haloferax volcanii* had an average angle of 120.42 +/- 37.41 μms^{-1} degrees (mean +/- standard deviation for 1020 reorientation events). The large reorientation angles observed here are indicative of the run-reverse reorientation behaviour.

For a cell exhibiting pure run-reverse motion, without any external forces, a reorientation angle of 180 degrees would be produced. The addition of Brownian motion (especially at this scale), and the off axis flagella 'wobble' observed within archaea could be responsible for the range of reorientation angles observed within experimentation. Smaller angles recorded could be accounted for in this way. However, it is possible that the peak fitting parameters captured events which were not true reorientations, but just extremes of the previously discussed random motions. Further analysis of the 'wobble' phenomenon would need to be implemented to improve peak-fitting parameters.

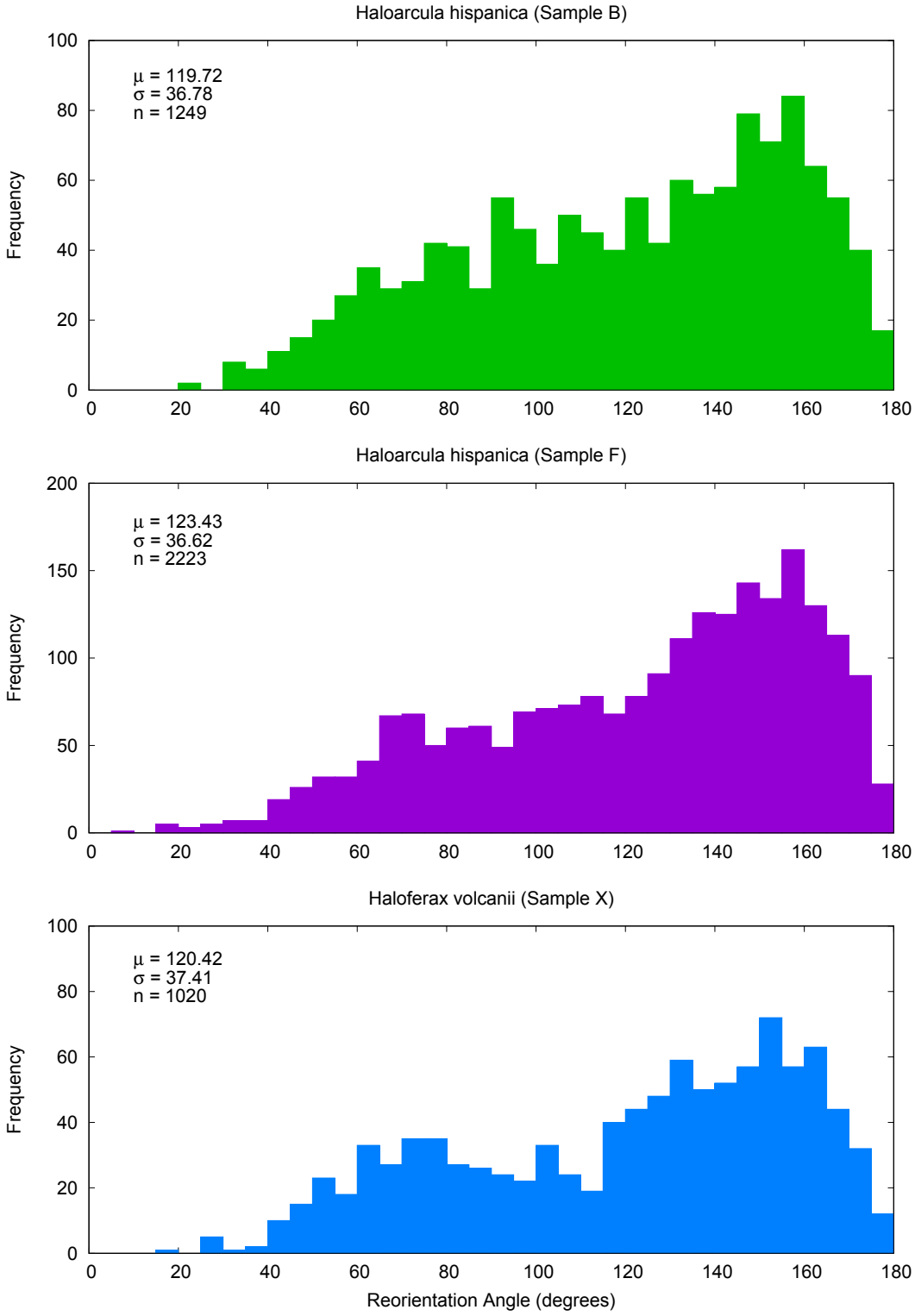

FIGURE 6.11. Reorientation angle histograms. Top to bottom: *Haloarcula hispanica* population 1 (sample B), *Haloarcula hispanica* population 2 (sample F) and *Haloferax volcanii* (sample x). Figure legend shows μ (mean) and σ (standard deviation) values for n number of reorientation events recorded for each strain.

6.4 Discussion

The haloarchaeal cells were observed to swim much more slowly than typical bacterial cells (roughly an order of magnitude more slowly). Furthermore, the reorientation events occurred less frequently than has previously been observed in other microorganisms [8, 111]. This could be a result of the increased effect of Brownian motion due to the smaller size of the cells, and their slower motility rates. Increased Brownian motion would lead to more diffusive trajectories than observed within bacterial species, thus could lead to a reduction in the need to actively reorientate. Moreover, this could be an energy-saving tactic employed by these extremophiles, as motor switching would require more energy than continued propulsion in a single direction.

The key finding of this section, is that the cells display reorientation angles indicative of run and reverse reorientation behaviours. The lack of the required genes for the synthesis of a flexible hook, is supported here, by the lack of any observed 'flick' behaviours. There was also very little variation in the swimming behaviours of each of the tested samples. Whilst all samples displayed slightly different results, these were marginally small, and could be the result of individual cell diversity, rather than species, or structural differences.

One area for further investigation is the noisy 'wobble' observed within the raw data tracks. This 'wobble' appeared on all trajectories and the magnitude was approximately constant throughout. Personal observations suggest that this may be the same phenomenon observed in [83], generated from the cell body rotation, as the positioning of the flagella is off axis to the centre of the cell body. In these experiments the spline smoothing parameter could be increased to improve the signal to noise ratio, however, this behaviour provides an interesting platform for further exploration. Any off axis movements would contribute to the overall change in directionality within the 'straight run' sections of the trajectory.

Chapter 7

General Discussion

7.1 Conclusions

Within this final chapter I will discuss the overarching findings of the project, and highlight some interesting areas for future study both closely linked to the project, and more remote fields of interest.

In chapter 2, it was revealed that all of the samples extracted from the Great Salt Lake had multiple copies of the 16S rRNA within their genome, this suggests that the organisms within the lake may have high levels of genetic heterogeneity, often swapping sections of DNA with members of the same (or in the case of sample B's flagellin genes, different) species. This level of lateral gene transfer was not evident in the single strain from Boulby Potash Mine, however, further samples would need to be collected (particularly from the mine) for a more accurate comparison. Whilst high levels of lateral gene transfer within extremophiles is relatively well characterised [71], this thesis is the first work to focus the adoption of genetic material within the archaellum structure. Unfortunately, only slight motility differences were observed between samples B and F from the Great Salt Lake. This could indicate that the alternative Fla genes were not expressed, or simply that both flagellins Fla A and Fla B produce very similar swimming patterns. If the latter is the case, further investigation into the evolution of both flagellins could aid indicate possible advantages to either structure, and provide insight into why such differences occur in an otherwise highly conserved molecular machine.

The dark-field spectroscopy experiments revealed that haloarchaea swim faster in the lag and early exponential phases than late exponential. This is particularly interesting as the biology standard for imaging bacterial swimming

has been established for decades as the late exponential phase (e.g [98, 111]). It is possible that older imaging techniques, such as Brightfield, which require a high density of cells, have led to the assumption that cells swim optimally at this stage. However, archaeal cells could simply have a different growth/motility pattern compared with bacterial counterparts. Either way, it would be interesting to further explore the swimming behaviours of early growth bacterial cells, of key laboratory strains. Such experiments could lead to fundamental changes in the way laboratories conduct motility experiments.

The key findings from the holography experiments, are the that *haloarcula hispanica* and *haloferax volcanii* both swim very slowly, when compared to other microorganisms and exhibit the run-reverse reorientation behaviour. Run-reverse swimming is typically indicative of polar flagellation, which is often displayed in marine bacteria, as it is less energetically expensive in low nutrient conditions. The 'flick' behaviour often observed with this swimming pattern is absent, due to the lack of a flexible flagella hook necessary for the 'flick' reorientation type. All samples imaged displayed high levels of Brownian rotation and an interesting, almost helical, 'wobble' movement. This 'wobble' can most likely be attributed to the off axis positioning of the archaellum, but would require further investigation to fully characterise. All three archaeal strains showed very similar swimming behaviours in all of the analysed parameters. When compared with the laboratory standard *E. coli*, cells displayed similar run duration distributions, but significantly longer actual times, and fewer reorientation events. Whilst the run duration distributions are indicative of general chemotaxis behaviour [7] the low levels of reorientations have never previously been described. It is likely that generating fewer reorientations is advantageous in the low nutrient environments experienced by haloarchaea, but further investigation would be needed to fully understand this unusual behaviour.

Overall, this thesis provides a comprehensive examination of environmental samples from two very distinct extreme saline sites. The work covers every step in the process, from collection, culture and sequencing, to an in-depth examination of the swimming behaviours. This is the first example of the 3D swimming behaviours of any haloarchaeal species and illustrates a unique method of 'slow-swimming' with few re-orientations, not previously observed in microbial species.

7.2 Future Work

This thesis provides the first investigation into the three-dimensional swimming behaviours of halophillic archaea. Consequently, there are many possible avenues for future exploration. Whilst the study of microbial motility has produced a wealth of research into the swimming behaviours of key laboratory species such as; *Escherichia coli*, *Bacillus subtillus* and *Chlamydomonas reinhardtii* [117], other organisms remain woefully under-represented within the literature. This is particularly true for archaeal species, which can be more challenging to collect and culture within the laboratory environment.

For all known microorganisms, the ability to move towards nutrient rich environments is the primary purpose for developing the ability to swim [4]. Whilst the various carbon sources suitable for the successful growth of *Haloarcula hispanica* and *Haloferax volcanii* have been defined through a variety of growth experiments ([43, 80]), the swimming behaviours associated with following a chemical gradient remain a mystery. It would be useful to explore whether a particular sugar or amino acid is preferential over others within the environment. This could aid in improving laboratory culturing, not only by optimizing the growth of the species explored within this thesis, but perhaps, also enabling the growth of some of the currently unculturable haloarchaea. Furthermore, given the slow swimming speeds and low reorientation rates (when compared with many bacterial species) observed within these experiments, it would be interesting to explore whether the presence of different sugars increase either the frequency of reorientations, or the overall swimming velocity.

Recent work by Kinosita *et al.* [83] used quantum dot fluorescence to successfully image the archaellum of an actively swimming haloarchaeon. This technique would be useful to employ alongside the existing data from this thesis, to generate a greater insight into the physical mechanisms for the observed swimming behaviours. For example, it would be beneficial to observe the number and position of the archaella. This could lead to greater understanding of the observed 'body wobble' phenomenon. Furthermore, comparisons could be made between the different types of flagellin found through the genetic analysis, to see if there are any obvious structural differences in the archaellum (length, thickness, pitch etc.).

Another avenue of interest for future research would be the photo-tactic responses of these. Many halophiles contain large quantities of a red-pigment known as rhodopsin. Rhodopsin acts either as a photoreceptor (sensory rhodopsin), track-

ing changes in light intensity, or as light-driven ion transporters (transporter rhodopsin). Multiple types of pigment can be expressed within a single cell, depending on the growth conditions and the individual species. In some haloarchaea there is evidence to suggest that individuals containing the sensory pigment will migrate towards longer wavelengths (red) of light, and be repelled by shorter wavelengths (blue) [150]. This increases the likelihood of exposure to useful light, to enable the activation of light-driven proton and chloride pumps via the transporter rhodopsin [151]. Whilst *H. hispanica* was extracted from a surface environment, where the diurnal cycles of the sun play an important role, *Hx. volcanii* was extracted form a site in total darkness. Whilst phenotypically *Hx. volcanii* appears to have less pigment (personal observation) than *H. hispanica*, some red colouring visibly remains. Consequently, comparing the light mediated behaviours in various wavelengths and intensities of light of these two species could yield interesting results.

7.3 Wider Context

Halophillic archaea are arguably one of the most resilient microorganisms on this planet, their ability to withstand dessication, large fluctuations in temperature, low nutrient availability and UV radiation, have made them a model organism for understanding how life on other planets may exist, and exactly where it is we should look [38]. It is highly possible that individuals could also be utilised for bioremediation of oil spills, bio-fuels, or other industrial purposes. Investing further research into these poorly understood microorganisms could provide a wide range of opportunities for future scientific and/or industrial developments.

Appendix (A) - Modified Growth Media Protocol

Modified Growth Media (MGM) is the recommended nutrient rich medium for culturing a wide variety of haloarchaeal species [45]. The media can be prepared in two stages the 'salt water' and 'nutrient' parts, which can be sterilised and stored for at least 6 months. MGM can be diluted to produce a range salt concentrations dependent upon the natural levels of osmotic pressure experienced by the study species. Furthermore, MGM is suitable for both solid and liquid growth mediums.

Salt Water

For a one litre stock solution, the following salts were dissolved in ≈ 900ml deionised water:

- 240 g Sodium Chloride (NaCl)
- 30 g Magnesium Chloride Hexahydrate ($MgCl_2 \cdot 6H_2O$)
- 35 g Magnesium Sulphate Heptahydrate ($MgSO_4 \cdot 7H_2O$)
- 7 g Potassium Chloride (KCl)
- 5 ml 1 Molar Tris(hydroxymethyl)aminomethane (Tris base)

When the salts were completely dissolved, 5 ml Calcium Chloride Dihydrate ($CaCl_2 \cdot 2H_2O$) from a one molar sterile stock solution was slowly added to the salt water solution. The pH was then adjusted to pH 7.5 through the addition of small quantities of Tris base. The solution was then autoclaved at 101 kPa for 15 minutes on a liquid cycle, and stored at room temperature in airtight containers.

Nutrient Component

For a one litre stock solution containing 25 % salt, the following ingredients were combined:

- 833 ml Salt Water stock solution
- 134 ml Deionised water
- 5 g Peptone (Oxoid)
- 1 g Yeast Extract

The pH was adjusted to 7.5 through the addition of small quantities of 1 M Tris base. Further DI water was added to reach the required 1 litre volume, before the solution was autoclaved at 101 kPa for 30 mins on a liquid cycle. Oxoid peptone was selected for this media, over the more commonly used Difco Bacto-Peptone, as the bile salts found in Difco Bacto-Peptone have previously been shown to cause cell lysis in some haloarchaeal species [58].

For solid medium, 1.5 % agar plates were produced through the addition of 15 g of Agar, and heating to 100 °C for 10-20 minutes to ensure fully dissolved before sterilisation. Solid media was autoclaved (101 kPa for 30 mins) and poured whilst relatively hot (≈ 60 °) into petri dishes to form 1 cm deep plates. Plates were cooled at room temperature overnight and stored at 4 °C.

Appendix (B) - Freezing Cells

Haloarchaeal cells can be frozen at - 80 °C for long-term storage. A glycerol and salt water solution [45] is combined with saturated culture to stabilize the cells and reduce the risk of membrane damage through ice crystal formation. The stock solution is prepared by combining:

- 80 ml of 100 % sterile Glycerol
- 20 ml of sterile SW stock solution (see Appendix A.0.1)
- 200 μl of sterile 0.5 molar Calcium Chloride ($CaCl_2$)

This stock solution can be combined with saturated or late exponential culture, at a ratio of 3:1 (Culture: Glycerol SW solution). Once thoroughly mixed, the resulting solution can be dispensed into cryo-tubes and stored at - 80 °C indefinitely (20 + years). The benefit of this type of storage, is not only the long-term preservation of cells, but also the separation of an uncontaminated cell-line which has been unaffected by generational adaptations to the laboratory environment, and thus remains as close to the original environmental individuals as is possible within a laboratory setting.

Appendix (C) - STE Buffer

For a 1 litre stock solution:

- 5.84 g Sodium Chloride (NaCl)
- 1.21 g Tris(hydroxymethyl)aminomethane (Tris base)
- 0.29 g Ethylenediaminetetraacetic acid (EDTA)

All chemicals were accurately weighed and dissolved in ≈ 900 ml deionised (DI) water, through warming and stirring. The pH of the resulting solution was adjusted to pH 8.0 using 1 Molar Hydrochloric Acid (HCL), and topped up to 1 litre with further DI water. Buffer was stored in sterile, air-tight containers at room temperature until required.

All chemicals used for experimentation were laboratory reagent grade (or higher), purchased from Sigma Aldrich or similar. Deionised water refers solely to Milli Q 'Type 1' ultra-pure filtered water [152].

Appendix (D) - Chemically Defined Media Protocol

Chemically defined media (CDM) is a relatively simple haloarchaeal minimal medium [144]. The standard protocol recommends an 18 % salt water solution, this was adapted to produce a higher salt medium (23 %).

For a 500 ml stock solution of 23 % salt water solution, the following salts were dissolved 400 ml of distilled water:

- 79.86 g Sodium Chloride (NaCl)
- 31.94 g Magnesium Chloride Hexahydrate ($MgCl_2 \cdot 6H_2O$)
- 3.19 g Potassium Sulphate ($K_2 \cdot SO_4$)
- 0.17 g Calcium Chloride Dihydrate ($CaCl2 \cdot 2H_2O$)

The solution was topped-up to 500 ml with DI water, and autoclaved on a liquid cycle (101 kPa above atmospheric pressure for 30 minutes). Prior to autoclaving 7 g of agar can be added, if solid medium is required.

After sterilization, the following chemicals can be added to the 500 ml salt water stock solution:

- 2.5 ml of 1 M Ammonium Chloride (NH_4Cl)
- 2 ml of (0.5 Molar) Potassium Phosphate Dibasic (K_2HPO_4)
- 0.5 ml Trace Elements
- 0.4 ml of 1 mg/ml Thiamine
- 0.05 ml of 1 mg/ml Biotin

Each of the additional solutions must be filter-sterilised prior to introduction to the media.

The trace elements were comprised of (per 100 ml solution):

- 36 mg Magnesium Chloride Tetrahydrate ($MnCl_2 \cdot 4H_2O$)
- 44 mg Zinc Sulphate Heptahydrate ($ZnSO_4 \cdot 7H_2O$)
- 230 mg Iron Sulphate Heptahydrate ($FeSO_4 \cdot 7H_2O$)
- 5 mg Copper Sulphate Pentahydrate ($CuSO4 \cdot 5H_2O$)

The pH was adjusted to 7.5 using HCl, and filter-sterilized to avoid precipitation through autoclaving.

A wide variety of carbon sources can be added to this medium, depending on the species of interest and/or field of research. A combination of glycerol and lactate were selected in this thesis, as recommended by [144].

- 150 μl glycerol (0.03 % of final solution)
- 150 μl lactate (0.03 % of final solution)

The final medial solution was adjusted to pH 7.5, through the drop-wise addition of Tris-base. It can then either be stored at room temperature in airtight containers, or poured into plates if solid medium.

Bibliography

[1] H. N. Schulz and B. Barker-Jorgensen. Big bacteria. *Annual Reviews in Microbiology*, 55:105–137, 2001.

[2] O. Reynolds. An experimental investigation of the circumstances which determine whether the motion of water shall be direct or sinuous, and of the law of resistance in parallel channels. *Proceedings of the Royal Society of London*, 35:935–982, 1883.

[3] S. Vogel. *Life in moving fluids: the physical biology of flow*. Princeton University Press, Princeton, New Jersey, 2nd edition, 1994.

[4] E. Purcell. Life at low reynolds number. *American Journal of Physics*, 45:3–11, 1977.

[5] D. B. Dusenbery. *Living at micro scale: The unexpected physics of being small*. Harvard University Press, Cambridge, Massachusetts, 1st edition, 2011.

[6] H. C. Berg. *Random walks in Biology*. Princeton University Press, Princeton, New Jersey, USA, expanded edition, 1993.

[7] H. C. Berg. *E. coli in motion*. Springer, New York, USA, 1st edition, 2003.

[8] R. Stocker. Marine microbes see a sea of gradients. *Science*, 338:628–633, 2012.

[9] M. T. Madigan, J. M. Martingo and J. Parker. *Brock Biology of Microorganisms*. Prentice Hall, Upper Saddle River, New Jersey, 10th edition, 2003.

[10] P. J. Keeling, R. L. Charlebois and W. F. Doolittle. Archaebacterial genomes: Eubacterial form and Eukaryotic content. *Current Opinion in Genetics and Development*, 4(6):816–822, 1994.

[11] J. L. Howland. *The Surprising Archaea: Discovering another domain of life*. Oxford University Press, New York, New York, 1st edition, 2000.

[12] C. R. Woese, G. E. Fox, L. Zablen, T. Uchida, L. Bonen, K. Pechman, B. J. Lewis and D. Stahl. Conservation of primary structure in 16s ribosomal RNA. *Nature*, 254:83–86, 1975.

[13] C. R. Woese and G. E. Fox. Phylogenetic structure of the prokaryotic domain: The primary kingdoms. *Proceedings of the National Academy of Sciences*, 71(11):5088–5090, 1977.

[14] E. F. DeLong. Archaea in coastal marine environments. *Proceedings of the Natural Academy of Sciences*, 89:5685–5689, 1992.

[15] C. Schleper, W. Holben and H. P. Klenk. Recovery of Crenarchaeotal ribosomal DNA sequences from freshwater-lake sediments. *Applied and Environmental Microbiology*, 63(1):321–323, 1997.

[16] S. B. Bintrim, T. J. Donohue, J. Handelsman, G. P. Roberts and R. M. Goodman. Molecular phylogeny of Archaea from soil. *Proceedings of the Natural Academy of Sciences*, 94:277–282, 1997.

[17] B. Dridi, D. Raoult and M. Drancourt. Archaea as emerging organisms in complex human microbiomes. *Anaerobe*, 17:56–73, 2011.

[18] H. Huber, S. Burggraf, T. Mayer, I. Wyschkony, R. Rachel and K. O. Stetter. *Ignicoccus* gen. nov., a novel genus of hyperthermophilic, chemolithoautotrophic Archaea, represented by two new species, *Ignicoccus islandicus* sp. nov. and *Ignicoccus pacificus* sp. nov. *International Journal of Systematic and Evolutionary Microbiology*, 50:2093–2100, 2000.

[19] E. F. DeLong, K. Y. Wu, B. B. Prézelin and R. V. Jovine. High abundance of Archaea in Antarctic marine picoplankton. *Nature*, 371:695–697, 1994.

[20] K. O. Stetter. Ultrathin mycelia-forming organisms from submarine volcanic areas having an optimum growth temperature of 105°C. *Nature*, 300:258–260, 1982.

[21] M. R. Mormile, M. A. Biesen, M. C. Gutierrez, A. Ventosa, J. B. Pavlovich, T. C. Onstott and J. K. Fredrickson. Isolation of *Halobacterium salinarum* retrieved directly from halite brine inclusions. *Environmental Microbiology*, 5(11):1094–1102, 2003.

[22] D. M. Barker. A class of their own - Archaea. *Crabtree Publishing Company*, page 17, 2010.

[23] R. Cavicchioli. Cold-adapted Archaea. *Nature Reviews Microbiology*, 4:331–343, 2006.

[24] B. Chaban, S. Y. M. Ng and K. Jarrell. Archaeal habitats - from the extreme to the ordinary. *The Canadian Journal of Microbiology*, 52:73–116, 2006.

[25] A. Oren. The ecology of the extremely halophilic Archaea. *FEMS Microbiology Reviews*, 13:415–440, 1994.

[26] G. Belovsky, D. Stephens, C. Perschon, P. Birdsey, D. Paul, D. Naftz, R. Baskin, C. Larson, C. Mellison, J. Luft, R. Mosley, H. Mahon, J. Van Leeuwen and D. V. Allen. The Great Salt Lake ecosystem (Utah, USA): long term data and a structural equation approach. *Ecosphere*, 2(33):1–40, 2011.

[27] S. DasSarma and P. Arora. Halophiles. *Encyclopedia of Life Sciences*, pages 1–9, 2001.

[28] A. Oren. Microbial life at high salt concentrations: phylogenetic and metabolic diversity. *Saline Systems*, 4(2), 2008.

[29] O. Henriet, J. Fourmentin, B. Delincé and J. Mahillon. Exploring the diversity of extremely halophilic archaea in food-grade salts. *International Journal of Food Microbiology*, 191:36–44, 2014.

[30] H. Abriouel, N. Benomar, R. Lucas and A. Gàlvez. Culture-independent study of the diversity of microbial populations in brines during fermentation of naturally-fermented Aloreña green table olives. *International Journal of Food Microbiology*, 144(3):487–496, 2011.

[31] W. Tapingkaea, S. Tanasupawatb, K. L. Parkinc, S. Benjakula and W. Visessanguan. Degradation of histamine by extremely halophilic Archaea isolated from high salt-fermented fishery products. *Enzyme and Microbial Technology*, 46(2):92–99, 2010.

[32] A. P. A. Oxley, M. P. Lanfranconi, D. Würdemann, S. Ott, S. Schreiber, T. J. McGenity, K. N. Timmis and B. Nogales. Halophillic Archaea in the human intestinal mucosa. *Environmental Microbiology*, 12(9):2398–2410, 2010.

[33] W. D. Williams, A. J. Boulton and R. G. Taaffe. Salinity as a determinant of salt lake fauna: a question of scale. *Hydrobilogia*, 197:257–266, 1990.

[34] A. Baricz, C. Coman, A. Ş. Andrei, V. Muntean, Z. G. Keresztes, M. Paŭşan, M. Alexe and H. L. Banciu. Spatial and temporal distribution of Archaeal diversity in meromictic, hypersaline Ocnei lake (Transylvanian Basin, Romania). *Extremophiles*, 18:399–413, 2014.

[35] Y. Ma, E. A. Galinski, W. D. Grant, A. Oren and A. Ventosa. Meeting review: Halophiles 2010: Life in saline environments. *Applied and Environmental Microbiology*, 76(21):6971–6981, 2010.

[36] R. E. Bardavid, P. Khristo and A. Oren. Interrelationships between dunaliella and halophilic prokaryotes in saltern crystallizer ponds. *Extremophiles*, 12:5–14, 2008.

[37] C. F. Norton and W. D. Grant. Survival of halobacteria within fluid inclusions in salt crystals. *Journal of General Microbiology*, 134:1365–1373, 1988.

[38] B. K. Baxter, B. Eddington, M. R. Riddle, T. N. Webster and B. J. Avery. Great Salt Lake halophilic microorganisms as models for astrobiology: Evidence for desiccation tolerance and ultraviolet irradiation resistance. *Proceedings of SPIE*, 2007.

[39] R. L. Mancinelli and L. I. Hochstein. The occurrence of denitrification in extremely halophilic Bacteria. *Foundation of European Microbiological Society*, 35:55–58, 1986.

[40] R. Hartmann, H. Sickinger and D. Oesterhelt. Anaerobic growth of halobacteria. *Proceedings of the National Academy of Science*, 77(6):3821–3825, 1980.

[41] D.M. Al-Mailem, N.A. Sorkhoh, H. Al-Awadhi, M. Eliyas and S.S. Radwan. Biodegradation of crude oil and pure hydrocarbons by extreme halophilic archaea from hypersaline coasts of the Arabian Gulf. *Extremophiles*, 14(3):321–328, 2010.

[42] S. Cohen, M. Shilo and M. Kessel. Nature of the salt dependence of the envelope of a Dead Sea archaebacterium, *Haloferax volcanii*. *Archives of Microbiology*, 156:198–203, 1991.

[43] A. Oren, A. Ventosa, M. C. Gutierrez and M. Kamekura. *Haloarcula quadrata* sp. nov., a square, motile archaeon isolated from a brine pool in Sinai (Egypt). *International Journal of Systematic Bacteriology*, 49:1149–1155, 1999.

[44] A. Oren. Life at high salt concentrations. *The Prokaryotes*, pages 263–282, 2006.

[45] M. Dyall-Smith. The halohandbook: Protocols for haloarchaeal genetics [version 7.2]. *http://www.haloarchaea.com/resources/halohandbook*, Online, 2009. [Accessed Dec 10, 2014].

[46] J. H. Brown and G. B. West. *Scaling in Biology*. Oxford University Press, New York, USA, 1st edition, 2000.

[47] C. F. Norton, T. J. Mcgenity and W. D. Grant. Archaeal halophiles (halobacteria) from two British salt mines. *Journal of General Microbiology*, 139:1077–1081, 1993.

[48] J. E. Meuser, B. K. Baxter, J. R. Spear, J. W. Peters, M. C. Posewitz and E. S. Boyd. Contrasting patterns of community assembly in the stratified water column of great salt lake, utah. *Environmental Microbiology*, 66:268–280, 2013.

[49] A. Oren. Halophilic microbial communities and their environments. *Current Opinion in Biotechnology*, 33:119–124, 2015.

[50] F. J. Post. The microbial ecology of the Great Salt Lake. *Microbial Ecology*, 3:143–165, 1977.

[51] Google Earth. Great Salt Lake Utah, 2d map of USA and satellite image of lake. *http://www.google.com/earth/index.html*, Online, 2017. [Accessed September 16, 2017].

[52] J. S. White, S. E. Null and D. G. Tarboton. How do changes to the railroad causeway in Utah's Great Salt Lake affect water and salt flow? *PLOS one*, 12(10):e0144111, 2015.

[53] B. K. Baxter, C. D. Litchfield, K. Sowers, J. D. Griffith, P. A. Dassarma and S. Dassarma. *Adaptation to Life at High Salt Concentrations in Archaea, Bacteria, and Eukarya - Chapter 3: microbial diversity of The Great Salt Lake*. Springer, Netherlands, 1st edition, 2005.

[54] L. L. Daniels. On the flora of the Great Salt Lake. *American Society of Naturalists*, 51(608):499–506, 1917.

[55] A. Murphy and S. Paling. The Boulby Mine Underground Science Facility: The search for dark matter, and beyond. *Nuclear Physics News*, 22(1):19–24, 2012.

[56] Polysulphate: organic fertilizer. Boulby mine stratigraphy. *http://www.polysulphate.com/introducing-polysulphate/*, Online, 2018. [Accessed Oct 31, 2018].

[57] T. J. McGenity, R. T. Gemmell, W. D. Grant and H. Stan-Lotter. Origins of halophilic microorganisms in ancient salt deposits. *Environmental Microbiology*, 2(3):243–250, 2000.

[58] M. Kamekura, D. Oesterhelt, R. Wallace, P. Anderson and D. J. Kushner. Lysis of halobacteria in bacto-peptone by bile acids. *Applied and Environmental Microbiology*, 54(4):990–995, 1988.

[59] A. Willis. Extrapolating abundance curves has no predictive power for estimating microbial biodiversity. *Proceedings of the National Academy of Sciences*, 113(5):E5096, 2016.

[60] K. J. Locey and J. T. Lennon. Reply to willis: Powerful predictions of biodiversity from ecological models and scaling laws. *Proceedings of the National Academy of Sciences*, 113(35):E5097, 2016.

[61] K. J. Locey and J. T. Lennon. Scaling laws predict global microbial diversity. *Proceedings of the National Academy of Sciences*, 10:1073, 2016.

[62] J. Shendure and H. Ji. Next-generation dna sequencing. *Nature Biotechnology*, 26:1135–1145, 2008.

[63] Enzoklop on Wiki-Commons. Schematic drawing of the PCR cycle. *https://en.wikipedia.org/wiki/Polymerase_chain_reaction*, Online, 2014. [Accessed October 09, 2018].

[64] Macherey-Nagel. PCR clean-up gel extraction user manual: Nucleospin gel and PCR clean-up. *http://www.mn-net.com/Portals/8/attachments/Redakteure_Bio /Protocols/DNA%20Cleanup/ UM_PCRcleanup_Gelex_NSGelPCR.pdf*, Online, 2017. [Accessed August 07, 2018].

[65] P. Desjardins and D. Conklin. NanoDrop microvolume quantitation of nucleic acids. *Journal of Visualized Experiments*, 45:e2565, 2010.

[66] DeNovix inc. Ds-11 spectrophotometer purity ratios: Technical note 130. *https://www.denovix.com/pdf/130-Purity-Ratios.pdf*, Online, 2014. Version 7.2.

[67] Labtech. Faq nanodrop. *https://www.labtech.com/sites/default/files/FAQ%20NanoDrop* Online, 2019. [Accessed March 07, 2019].

[68] S. F. Altschul, W. Gish, W. Miller, E. W. Myers and D. J. Lipman. Basic local alignment search tool. *Journal of Molecular Biology*, 14(215):403–410, 1990.

[69] Y. Van-De-Peer. *The Phylogenetic Handbook: a Practical Approach to Phylogenetic Analysis and Hypothesis Testing*. Cambridge University Press, Cambridge, UK, 2009.

[70] R. T. Papke, O. Zhaxybayeva, E. J. Feil, K. Sommerfeld, D. Muise and W. F. Doolittle. Searching for species in Haloarchaea. *Proceedings of the National Academy of Sciences*, 104(35):14092–14097, 2007.

[71] A. Wagner, R. J. Whitaker, D. J. Krause, J. Heilers, M. Wolferen, C. Does and S. Albers. Mechanisms of gene flow in Archaea. *Nature Reviews Microbiology*, 15:492–501, 2017.

[72] D. L. Sun, X. Jiang, Q. L. Wu and N. Y. Zhou. Intragenomic heterogeneity of 16s rRNA genes causes overestimation of prokaryotic diversity. *Applied and Environmental Microbiology*, 79(19):5962–5969, 2013.

[73] H. L. Cui, P. J. Zhou, A. Oren and S. J. Liu. Intraspecific polymorphism of 16s rRNA genes in two halophilic archaeal genera, *Haloarcula* and *Halomicrobium*. *Extremophiles*, 13:31–37, 2009.

[74] L. D. Crosby and C. S. Criddle. Understanding bias in microbial community analysis techniques due to rrn operon copy number heterogeneity. *BioTechniques*, 34(4):2–9, 2003.

[75] A.López-López, S. Benlloch, M. Bonfá, F. Rodríguez-Valera and A. Mira. Intragenomic 16s rDNA divergence in *Haloarcula marismortui* is an adaptation to different temperatures. *Foundation of European Microbiological Society*, 35:55–58, 2007.

[76] E. A. Lynch, M. G. I. Langille, A. Darling, E. G. Wilbanks, C. Haltiner, K. S. Y. Shao, M. O. Starr, C. Teiling, T. T. Harkins, R. A. Edwards, J. A. Eisen and M. T. Facciotti. Sequencing of seven haloarchaeal genomes reveals patterns of genomic flux. *PLOS One*, 7(7):e41389, 2012.

[77] G. Juez, F. Rodriguez-Valera, A. Ventosa and D. J. Kushner. *Haloarcula hispanica* spec. nov. and *Haloferax gibbonsii* spec, nov., two new species

of extremely halophilic archaebacteria. *Systems of Applied Microbiology*, 8:75–79, 1986.

[78] B. E. Volcani. Bacteria in the bottom sediments of the dead sea. *Nature*, 142(3853):274–275, 1943.

[79] A. Zaigler, S. C. Schuster and J. Soppa. Construction and usage of a onefold-coverage shotgun DNA microarray to characterize the metabolism of the archaeon *Haloferax volcanii*. *Molecular Microbiology*, 48(4):1089–1105, 2003.

[80] J. A. Leigh, S. Albers, H. Atomi and T. Allers. Model organisms for genetics in the domain archaea: methanogens, halophiles, thermococcales and sulfolobales. *Foundation of European Microbiological Society - Microbiology Reviews*, 35(4):577–608, 2011.

[81] S. Albers and K. F. Jarrell. The archaellum: How archaea swim. *Frontiers in Microbiology*, 6(23):1–12, 2015.

[82] K. F. Jarrell, and S. V. Albers. The archaellum: an old motility structure with a new name. *Trends in Microbiology*, 20(7):307–312, 2012.

[83] Y. Kinosita, N. Uchida, D. Nakane and T. Nishizaka. Direct observation of rotation and steps of the archaellum in the swimming halophilic archaeon *Halobacterium salinarum*. *Nature Microbiology*, 1038:16148, 2016.

[84] S. Y. M. Ng, B. Zolghadr, A. J. M. Driessen, S. V. Albers and K. F. Jarrell. Cell surface structures of archaea. *Journal of Bacteriology*, 190(8):6039–6047, 2018.

[85] S. Albers and K. F. Jarrell. The archaellum: An update on the unique archaeal motility structure. *Trends in Microbiology*, 26(4):351–362, 2018.

[86] M. G. Pyatibratov, S. N. Beznosov, R. Rachel, E. I. Tiktopulo, A. K. Surin, A. S. Syutkin and O. V. Fedorov. Alternative flagellar filament types in the haloarchaeon *Haloarcula marismortui*. *Canadian Journal of Microbiology*, 54:834–844, 2008.

[87] J. V. Zuylen. The microscopes of Antoni van Leeuwenhoek. *Journal of Microscopy*, 121:309–328, 1981.

[88] B. Cohen. On Leeuwenhoek's method of seeing Bacteria. *Journal of Bacteriology*, 34(3):343–346, 1937.

[89] Porter. Antony van Leeuwenhoek: Tercentenary of his discovery of Bacteria. *American Society for Microbiology*, 40(2):260–269, 1976.

[90] Zeiss. Basic microscopy resources. *https://www.zeiss.com/microscopy/us/solutions/reference/basic-microscopy/koehler-illumination.html*, Online, 2018. [Accessed February 07, 2018].

[91] Nikon. Microscopy U. *https://www.microscopyu.com*, Online, 2018. [Accessed February 07, 2018].

[92] M. Davidson and M. Abramowitz. Optical microscopy. *Encyclopedia of Imaging Science and Technology*, 2:1106–1141, 2002.

[93] P. Evennett. Köler illumination: A simple interpretation. *Proceedings of the Royal Microscopical Society*, 28(4):189–192, 1983.

[94] F. Zernike. How I discovered phase contrast. *Science*, 121:354–349, 1955.

[95] E. Hecht. *Optics*. Addison Wesley, San Francisco, California, 4th edition, 2002.

[96] Molecular Expressions. Optical microscopy primer: Specialized techniques. *https://micro.magnet.fsu.edu/primer/techniques/phasecontrast/phase.html*, Online, 2018. [Accessed April 12, 2018].

[97] Encyclopaedia Britannica. Constructive and destructive wave interference. *https://kids.britannica.com/students/assembly/view/53869l*, Online, 2018. [Accessed April 12, 2018].

[98] R. M. Macnab and D. E. Koshland. Bacterial motility and chemotaxis: Light-induced tumbling response and visualization of individual flagella. *Journal of Molecular Biology*, 84:399–406, 1974.

[99] R. M. Macnab. Examination of bacterial flagellation by dark-field microscopy. *Journal of Clinical Microbiology*, 4(3):258–265, 1976.

[100] Y. Magariyama, S. Sugiyama, K. Muramoto, I. Kawagishi, Y. Imae and S. Kudot. Simultaneous measurement of bacterial flagellar rotation rate and swimming speed. *Biophysical Journal*, 69:2154–2162, 1995.

[101] T. Horio and H. Hotani. Visualization of the dynamic instability of individual micro-tubules by dark-field microscopy. *Letters to Nature*, 321:605–607, 1986.

[102] A. Runemark, M. Wellenreuther, H. H. E. Jayaweera, S. Svanberg and M. Brydegaard. Rare events in remote dark-field spectroscopy: An ecological case study of insects. *IEEE Journal of Selected Topics in Quantum Electronics*, 18(5):1573–1582, 2012.

[103] M. Li. Experimental study of swimming flagellated bacteria and their collective behaviour in concentrated suspensions. PhD Thesis. *The University of Edinburgh*, 2010.

[104] L. G. Wilson, R. Zhang, V. A. Martinez, M. Li, J. Schwarz-Linek, A. N. Morozov, J. Arlt and W. C. K. Poon. High speed, high-throughput screening of molecular motor speed in a free-swimming bacterial population. *In Preparation*.

[105] Y. Han, A. M. Alsayed, M. Nobili, J. Zhang, T. C. Lubensky and A. G. Yodh. Brownian motion of an ellipsoid. *Science*, 314:626–630, 2006.

[106] H. Khouri, J. G. Mitchell, L. Pearson, A. Bonazinga, S. Dillon and R. Paxinos. Long lag times and high velocities in the motility of natural assemblages of marine bacteria. *Applied and Environmental Microbiology*, 61(3):877–882, 1995.

[107] J. E. Johansen, J. Pinhassi, N. Blackburn, U. L. Zweifel and Å. Hagström. Variability in motility characteristics among marine bacteria. *Aquatic Microbial Ecology*, 28:229–237, 2002.

[108] K. Son, J. S. Guasto and R. Stocker. Bacteria can exploit a flagellar buckling instability to change direction. *Nature Physics*, 9:494–498, 2013.

[109] M. Theves, J. Taktikos, V. Zaburdaev, H. Stark and C. Beta. A bacterial swimmer with two alternating speeds of propagation. *Biophysical Journal*, 105:1915–1924, 2013.

[110] I. Duchesne, S. Rainville and T. Galstian. Bacterial motility reveals unknown molecular organization. *Biophysical Journal*, 109:2137–2147, 2015.

[111] H. C. Berg and D. A. Brown. Chemotaxis in *E. coli* analysed by three-dimensional tracking. *Nature*, 239:500–504, 1972.

[112] M. Wu, J. W. Roberts, S. Kim, D. L. Koch, and M. P. DeLisa. Collective bacterial dynamics revealed using a three-dimensional population-scale defocused particle tracking technique. *Applied and Environmental Microbiology*, 72(7):4987–4994, 2006.

[113] M. Wu, J. W. Roberts and M. Buckley. Three-dimensional fluorescent particle tracking at micron-scale using a single camera. *Experiments in Fluids*, 38:461–465, 2005.

[114] G. Li and J. X. Tang. Accumulation of microswimmers near a surface mediated by collision and rotational brownian motion. *Physical Review Letters*, 103:078101, 2009.

[115] K. M. Taute, S. Gude, S. J. Tans and T. S. Shimizu. High-throughput 3D tracking of bacteria on a standard phase contrast microscope. *Nature Communications*, 6:8776, 2015.

[116] M. J. Orchard, S. Humphries, R. Schuech and S. Menden-Deuer. The influence of viscosity on the motility and sensory ability of the dinoflagellate *Heterocapsa triquetra*. *Journal of Plankton Research*, 38(4):1062–1076, 2016.

[117] K. Son, D. R. Brumley, and R. Stocker. Live from under the lens: exploring microbial motility with dynamic imaging and microfluidics. *Nature Reviews Microbiology*, 13:761–775, 2015.

[118] M. K. Kim. Principles and techniques of digital holographic microscopy. *SPIE Reviews*, 1:018005, 2010.

[119] N. E. Farthing, R. C. Findlay, J. F. Jikeli, P. B. Walrad, M. A. Bees and L. G. Wilson. Simultaneous two-color imaging in digital holographic microscopy. *Optics Express*, 25(23):28489, 2017.

[120] D. Gabor. A new microscopic principle. *Nature*, 161(4098):777–778, 1948.

[121] U. Schnars and W. Juptner. Direct recording of holograms by a CCD target and numerical reconstruction. *Applied Optics*, 33:179–181, 1994.

[122] M. H. Jericho and H. J. Kreuzer. *Coherent light microscopy - chapter 1: Point Source Digital In-Line Holographic Microscopy*. Springer Series in Surface sciences, Berlin, Germany, 1st edition, 2011.

[123] C. B. Giuliano, R. Zhang, and L. G. Wilson. Digital inline holographic microscopy (dihm) of weakly-scattering subjects. *Journal of Visualized Experiments*, 84:e50488, 2014.

[124] S. K. Jericho, P. Klages, J. Nadeau, E. M .Dumas, M. H. Jericho and H. J. Kreuzera. In-line digital holographic microscopy for terrestrial and exobiological research. *Planetary and Space Science*, 58(4):701–705, 2010.

[125] S. Lee, Y. Roichman, G. R. Yi, S. H. Kim, S. M. Yang, A. van Blaaderen, P. van Oostrum and D. G. Grier. Characterizing and tracking single colloidal particles with video holographic microscopy. *Optics Express*, 15:18275–18282, 2007.

[126] A. Wang, R. F. Garmann and V. N. Manoharan. Tracking *E. coli* runs and tumbles with scattering solutions and digital holographic microscopy. *Optics Express*, 24(21):23719–23725, 2016.

[127] F. C. Cheong, B. J. Krishnatreya and D. G. Grier. Strategies for three-dimensional particle tracking with holographic video microscopy. *Optics Express*, 18(13):13563–13573, 2010.

[128] S. Lee and D. G. Grier. Holographic microscopy of holographically trapped three-dimensional structures. *Optics Express*, 15(4):1505–1512, 2007.

[129] C. J. Mann, L. Yu, C. Lo and M. K. Kim. High-resolution quantitative phase-contrast microscopy by digital holography. *Optics Express*, 13(22):8693–8698, 2005.

[130] E. Zetsche, A. E. Mallahi, F. Dubois, C. Yourassowsky, J. C. Kromkamp and F. J. R. Meysman. Imaging-in-flow: Digital holographic microscopy as a novel tool to detect and classify nanoplanktonic organisms. *Limnology and Oceanography: Methods*, 12:757–775, 2014.

[131] E. Zetsche, A. Mallahi and F. J. R. Meysman. Digital holographic microscopy: A novel tool to study the morphology, physiology and ecology of diatoms. *Diatom Research*, 31(1):1–16, 2016.

[132] Z. Frentz, S. Kuehn, D. Hekstra and S. Leibler. Microbial population dynamics by digital-in-line holographic microscopy. *Review of Scientific Instruments*, 81:084301, 2010.

[133] T. Su, L. Xuea and A. Ozcana. High-throughput lensfree 3D tracking of human sperms reveals rare statistics of helical trajectories. *Proceedings of the National Academy of Science*, 109(40):16018–16022, 2012.

[134] J. F. Jikeli, L. Alvarez, B. M. Friedrich, L. G. Wilson, R. Pascal, R. Colin, M. Pichlo, A. Rennhack, C. Brenker and U. B. Kaupp. Sperm navigation along helical paths in 3d chemoattractant landscapes. *Nature Communications*, 6(7985):8985, 2015.

[135] L. G. Wilson, L. M. Carter and S. E. Reece. High-speed holographic microscopy of malaria parasites reveals ambidextrous flagellar waveforms. *Proceedings of the National Academy of Science*, 10(47):18769–18774, 2013.

[136] M. Bartels, M. Krenkel, J. Haber, R. N. Wilke and T. Salditt. X-ray holographic imaging of hydrated biological cells in solution. *Physical Review Letters*, 114:048103, 2015.

[137] S. M. Vater, S. Weiße, S. Maleschlijski, C. Lotz, F. Koschitzki, T. Schwartz, U. Obst and A. Rosenhahn. Swimming behavior of *Pseudomonas aeruginosa* studied by holographic 3d tracking. *PLOS one*, 9(1):e87765, 2014.

[138] J. Sheng, E. Malkiel, J. Katz, J. Adolf, R. Belas and A. R. Place. Digital holographic microscopy reveals prey-induced changes in swimming behavior of predatory dinoflagellates. *Proceedings of the National Academy of Science*, 104(44):17512–17517, 2007.

[139] L. G. Wilson. Portable holographic microscope. *Personal Communication*.

[140] K. Thornton, R. Finlay, P. Walrad and L. Wilson. *Investigating the Swimming of Microbial Pathogens using Digital Holography - in: Biophysics of Infection*. Springer, New York, USA, 2016.

[141] L. G. Wilson and R. Zhang. 3d localization of weak scatterers in digital holographic microscopy using rayleigh-sommerfeld back-propagation. *Optics Express*, 20(15):16736, 2012.

[142] J. C. Crocker and D. G. Grier. Methods of digital video microscopy for colloidal studies. *Journal of Colloid and Interface Science*, 179(217):298–310, 1996.

[143] N. A. Campbell and J. B. Reece. *Biology*. Pearson, London, UK, 8th edition, 2008.

[144] T. Kauri, R. Wallace and D.J. Kushner. The nutrition of the halophilic Archaeabacterium, *Haloferax volcanii*. *Systematic and Applied Microbiology*, 13:14–18, 1990.

[145] K. Grayson, C. M. de Silva, N. Hutchins and I. Marusic. Beam stability and warm-up effects of Nd:YAG lasers used in particle image velocimetry. *Measurement Science and Technology*, 28:065301, 2017.

[146] H. Winet. Wall drag on free-moving ciliated micro-organisms. *Journal of Experimental Biology*, 59:753–766, 1973.

[147] E. Lauga, W. R. DiLuzio, G. M. Whitesides and H. A. Stone. Swimming in circles: Motion of bacteria near solid boundaries. *Biophysical Journal*, 90(2):400–412, 2006.

[148] M. Molaei, M. Barry, R. Stocker and J. Sheng. Failed escape: Solid surfaces prevent tumbling of *Escherichia coli*. *Physical Review Letters*, 6(113):068103, 2014.

[149] Oscar Guadayol, K. L. Thornton and S. Humphries. Cell morphology governs directional control in swimming bacteria. *Scientific Reports*, 7:2061, 2017.

[150] S. I. Bibikov and V. P. Skulachev. Mechanisms of phototaxis and aerotaxis in *Halobacterium halobium*. *Federation of European Biochemical Societies*, 243(2):303–306, 1989.

[151] K. H. Jung. The distinct signaling mechanisms of microbial sensory rhodopsins in Archaea, Eubacteria and Eukarya. *Photochemistry and Photobiology*, 83:63–69, 2006.

[152] Milli-Q. Milli-q direct water purification system - overview. *http://www.merckmillipore.com*, Online, 2018. [Accessed May 15, 2018].